8-2020

Benchmarking of a Mobile Phone Particle Image Velocimetry System

David Armijo
Utah State University

BENCHMARKING OF A MOBILE PHONE PARTICLE IMAGE VELOCIMETRY SYSTEM

by

David Armijo

A thesis submitted in partial fulfillment
of the requirements for the degree

of

MASTER OF SCIENCE

in

Mechanical Engineering

Approved:

Tadd T. Truscott, Ph.D. Major Professor	Angela Minichiello, Ph.D., P.E. Committee Member
Barton Smith, Ph.D. Committee Member	Richard S. Inouye, Ph.D. Vice Provost for Graduate Studies

UTAH STATE UNIVERSITY
Logan, Utah

2020

ABSTRACT

Benchmarking of a Mobile Phone Particle Image Velocimetry System

by

David Armijo, Master of Science

Utah State University, 2020

Major Professor: Tadd T. Truscott, Ph.D.
Department: Mechanical and Aerospace Engineering

As part of a two-decade-long effort to create simplified particle image velocimetry (PIV) systems and make them more widely available, many new and useful PIV innovations have come forth. Two such innovations are the production of open-source PIV software [1, 2, 3, 4, 5] and the idea of image acquisition using smartphones [6, 7]. We seek to combine both of these together into one mobile device application, called *mobile Instructional PIV* (mI-PIV). This application will use the mobile device's internal camera for image acquisition and then perform cross-correlation and other PIV functions using open-source algorithms, without any need for a computer. Such a design will greatly reduce complexity and cost from basically any system that has been brought forth so far and has the potential to open up a much larger PIV user-base, including high school students. This thesis describes the examination of different parameters of the mI-PIV system and their effects on the accuracy of the system. Such a study will serve to guide in the iterative design process of mI-PIV as we strive to balance safety, simplicity, cost, and accuracy of the system. Using this process, we plan to create a real solution for making PIV a useful tool in high school classrooms, undergraduate laboratories, and potentially in industries where inexpensive, low-speed fluid velocity measurements are needed.

(121 pages)

PUBLIC ABSTRACT

Benchmarking of a Mobile Phone Particle Image Velocimetry System

David Armijo

One of the most important tools in a fluid dynamics laboratory is a particle image velocimetry (PIV) system. This system can measure the speed of a fluid flow simply by taking high-speed images of the motion of the fluid, then applying PIV cross-correlation software to calculate speed from the resulting images. The mI-PIV project is in the process of designing a new method of performing PIV by putting the cross-correlation software on a mobile phone application, called *mobile Instructional PIV* (mI-PIV). This system is an innovative stepping stone in making PIV systems more widely available. It is designed to be convenient and safe even for high school classrooms, which until now have had virtually no exposure to PIV due to its expensive, complex, and dangerous nature.

This thesis will describe the examination of different aspects of the mI-PIV system, such as algorithms and illumination for imaging of the flow, and their separate effects on the accuracy of the system. Such a study serves to guide in the design process of mI-PIV as we strive to balance safety, simplicity, cost, and accuracy of the system. Using this process, we plan to create a real solution for making PIV a useful tool in high school classrooms, undergraduate laboratories, and potentially in industries where inexpensive, low-speed fluid velocity measurements are needed.

ACKNOWLEDGMENTS

Of course, I want to start by thanking Dr. Tadd Truscott, my thesis advisor. Thank you so much, Tadd, not only for guiding me through every aspect of the master's program, but also for being an inspiration to me and everyone in the Splashlab. We all feed off your energy and the love that you have for your work. You're the only thesis advisor I've had, but in my mind and from my observations, you are the definition of a great advisor. I feel like all of us in the Splashlab get the one-on-one attention we need, and all of us, as well as our work and our ideas, are treated with respect. You have been there for me every step of the way and have shared invaluable wisdom and training not only in PIV and scientific research in general, but also in scientific writing and presentation of data as well. I'm proud of all the things I've learned from you and I have been blessed to be part of your lab.

Dr. Angela Minichiello, it has been an absolute pleasure to work with you on the mI-PIV project. What a privilege to be part of such an innovative and fascinating creative process, and I have you to thank for taking me in and getting me funded for the past two years. I had a great time and honestly, I thought our team meetings were really fun and that you ran them well. Also, thank you for your support with my thesis and all the edits you've done for it, as well as for the presentation and poster that I did.

Dr. Barton Smith, you have been a very important part of the work I've done and I really appreciate your guidance in doing PIV the right way, troubleshooting, and helping me interpret the data I've shown you along the way. Your wisdom has been very helpful. Also, thank you for letting me use your lab and for being gracious in lending me your equipment.

I was part of the coolest team. Dr. Vladimir Kulyukin, Sarbajit Mukherjee, Lori Caldwell, Aditya Bhouraskar, Jack Elliot, Oliver Hulme, and Andrea Peterson, you were seriously so fun to work with, all of you. You've helped make my master's experience an awesome one.

My lab mates have helped me in my thesis process as well. Dr. Akihito Kiyama, Rafsan Rabbi, Matthew Jones, Jeffrey Fonnesbeck, Emma Fraley, Rafid Rahman, Cody

Hatch, Sarah Dayley, and Chase Mortensen, thanks for any help you've given me and your edits on the stuff I've done. And we've had great times together too. Also, special thanks to Emma for providing some very helpful code that has helped the CS guys and me learn how to write PIV code.

Thanks to Bart's lab — Nazmus Sakhib, Andrew Smith, Austin Parker, and John Garret — for welcoming me into their lab downstairs and helping me when I needed it. Especially Nazmus, thanks for getting me started with the water tunnel and for doing PIV on DaVis for me here and there. Thank you, Dr. Kurt Becker, Candida Desjardins, Dr. Jean Hertzberg, Dr. John Charonko, and Dr. Doug Neal, for your participation in the mI-PIV project. Your advice and your resources have been much appreciated and very useful to my work.

To my lovely wife, Andrea: I can't believe how supportive you've been throughout this process, from the times I've come home late and dinner is waiting for me, to the many times you've sat and listened to me going on and on about all the sciency stuff I'm doing and have been genuinely interested. You have been the rock in my life, and even when things have been difficult and I've gotten frustrated or down, you've been there to lift me up every time. You and Ellie are my world. I love you.

CONTENTS

LIST OF TABLES

Table Page

LIST OF FIGURES

CHAPTER 1

Introduction

1.1 PIV - A Brief Overview

Offering unobtrusive, accurate, whole-field velocity data for a large variety of fluid flows, particle image velocimetry (PIV) is a powerful fluid velocity measurement technique. Visual by nature, it can turn a complex fluid flow into a vector field that is easy to understand and quantifiable, making it a staple in research laboratories all over the world for a multitude of fluid dynamics applications [10, 13, 14].

For PIV in its most basic form (macroscopic planar PIV), a laser sheet illuminates particles in a flow and a high-speed camera is used to capture images of a field of view (FOV) in the flow, as shown in fig. 1.1.

The acquired images are grouped into "image pairs" and then particle displacement is found for those image pairs. The two images in each image pair are both split into a grid of square windows or interrogation areas (IA). Each interrogation area in the second image IA_2 is shifted by r pixels row-wise and s pixels column-wise from the location of the interrogation area in the first image IA_1, as shown in fig. 1.2(a). These shifts represent possible particle displacements $\Delta\vec{x}(r,s)$. The correlation R of the particle intensities in the two interrogation areas at each of these $\Delta\vec{x}(r,s)$ is then calculated by eq. (1.1) [9], where D_I is the size of the sides of the IA in pixels. The correlation coefficients at all possible displacement locations can be shown as peaks, like in fig. 1.2(b). The algorithm selects the largest peak as the approximate displacement, shown as the green vector in figs. 1.2(a) and 1.2(b). This type of cross-correlation is called "direct cross-correlation" (DCC).

$$R(r,s) = \sum_{i=0}^{D_I/2} \sum_{i=0}^{D_I/2} IA_1(i,j) IA_2(i+r, j+s) \tag{1.1}$$

A more common correlation method is the fast-Fourier transform (FFT) correlation

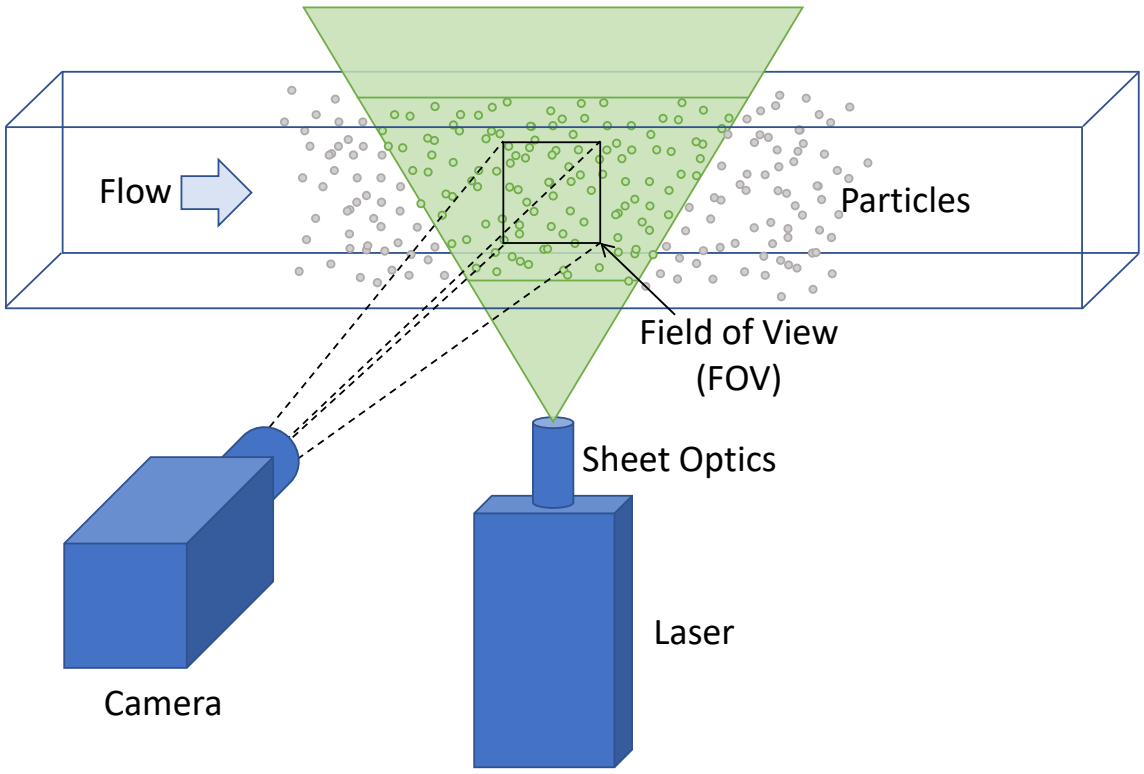

Fig. 1.1: Schematic of basic PIV setup. A flow is moving from left to right and particles in the flow (dots) are illuminated by a laser that is passed through a sheet optic to make a laser sheet. A camera images the illuminated portion of the flow field as illustrated by the box outline.

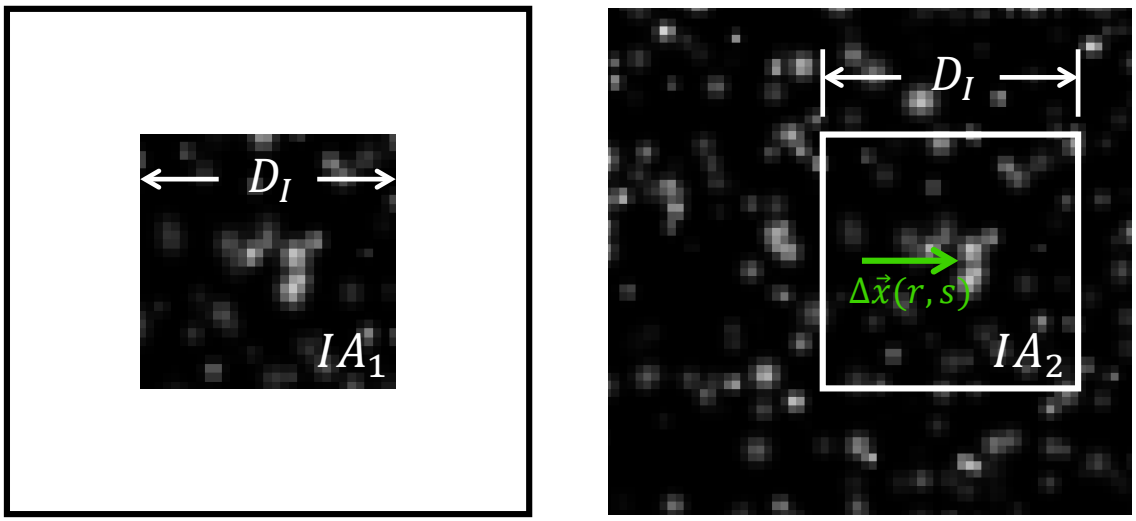

(a)

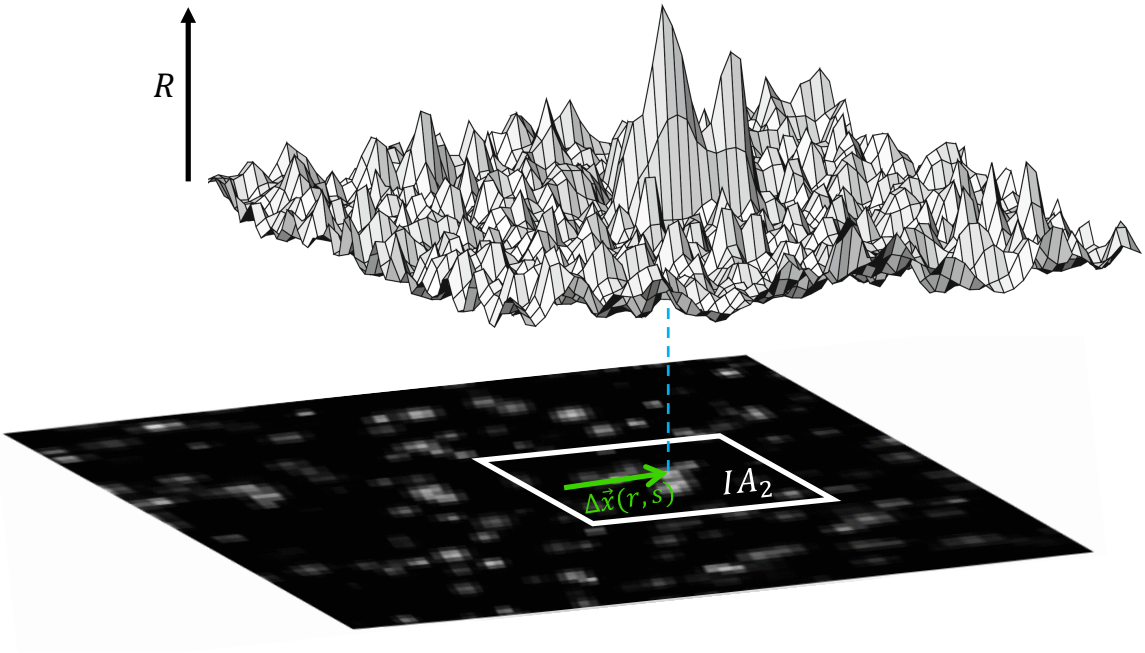

(b)

Fig. 1.2: (a) Illustration of the cross-correlation of IA_1 and IA_2, according to eq. (1.1) [9], where D_I is the size of the side of the interrogation regions and $\Delta\vec{x}(r,s)$ is a possible displacement given by a window shift of (r,s). (b) An example of peaks representing the correlation R obtained by cross-correlation of IA_1 and IA_2. The image of correlation peaks was obtained from [10].

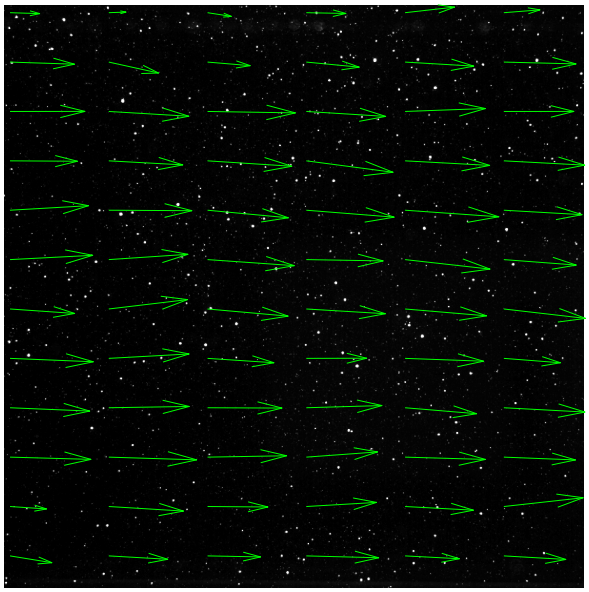

Fig. 1.3: Velocity measurements in the FOV from a basic PIV setup overlaid on top of a raw image from the camera, where particles have been illuminated by a laser sheet.

technique, more widely used because of its superior speed, but not detailed here due to its complexity. After cross-correlation, subpixel accuracy can be achieved by fitting a Gaussian curve to the largest cross-correlation peak and its two largest neighbors then finding the peak of that Gaussian curve. For more detailed descriptions of PIV algorithms, see [9, 10, 14, 15, 16, 17].

Displacements at every interrogation area IA in the image pair are found, and these can be shown as vectors, like in fig. 1.3, or used to find different characteristics of the flow, such as shear, flow rate, vorticity, boundary layers, or pressure measurements. With this technique, fluid dynamicists can take measurements of an entire FOV of a fluid flow at once, with minimal disturbance of the actual flow [10]. There are other forms and variations of PIV, such as steroscopic PIV, micro-PIV, and tomographic PIV, to name a few, but this work will be primarily concerned with planar PIV.

A typical lab-grade PIV system includes either a pulsed Nd:YAG (532 nm) or a pulsed Nd:YLF (527 nm) laser, both of which have desirable optical properties and pulsing capabilities for PIV measurement systems. These two components are usually paired with a syncing device in order to time the pulses of the laser with the frame rate of the cam-

era exposures. Pulsing of the laser allows for particles to be illuminated only very briefly (usually in the range of μs or ns) to prevent "particle streaking" in the images caused by particle motion during the exposure. If the flow is slow enough that pulsing is not needed, a diode-pumped solid-state (DPSS) continuous-wave (CW) laser may be used [9].

Since PIV relies on illumination of particles *inside* a fluid, it is only possible in clear fluids such as water or air. For water, usually an experiment is "seeded" with polyamide particles or hollow glass spheres. Air may be seeded by olive oil droplets, fog droplets, or bubbles. These particles must be neutrally buoyant (or as close as possible to neutrally buoyant). In other words, they must have a specific gravity as close to that of the fluid as possible, so that they follow the flow faithfully. For liquids, particles can have specific gravity very close to that of the fluid, but for air this is impossible. It is usually desirable to have small particles, around around 10 μm - 100 μm in diameter for water and 1 μm - 3 μm for air [9], to minimize the effects of differences in specific gravity and help particles follow the flow as closely as possible.

1.2 The mI-PIV Project – Introduction

A traditional PIV setup is expensive (usually more than $100,000), complex, and potentially dangerous due to the use of high-powered lasers, so it is only really practical for serious fluid dynamics laboratories. The *mobile Instructional PIV* (mI-PIV) project seeks to broaden the availability of PIV to more students in lower education by drastically reducing cost, complexity, and safety hazards by downsizing to lower-grade – but still effective – PIV components. Such a goal is not new to the scientific community, and many studies have brought forth innovative simplified PIV systems, such as described in [6, 18, 19, 20, 21, 22, 23, 24, 25], which will be expounded upon in Section 1.4. The mI-PIV system builds upon different aspects of many of these other simplified systems, but it also introduces a relatively novel idea: putting image correlation software on a mobile device application and using that mobile device's internal camera for image acquisition. This removes the need for a computer as a part of the mI-PIV system components. The mI-PIV system also utilizes a low-powered laser pointer, such as can be purchased on online stores

like Amazon, DigiKey, laserpoints.com, laserpointerpro.com, etc. in order to be usable in a setting where highly involved safety procedures and equipment are not possible and/or practical. These features will enable a much larger user base of PIV for those who are more concerned about cost and safety than achieving lab-grade accuracy, making it a versatile tool in all levels of education. The mI-PIV system will be a viable option for more undergraduate laboratories and it will even be practical for use in high school classrooms, which is unprecedented, even for other simplified PIV systems previously cited. Since high school students generally benefit from visual lessons and seem to have interest in lasers and mobile phones, mI-PIV can be a very effective tool to increase their interest in fluid dynamics. In fact, in one study, mobile devices were used as learning aids for a variety of subject matters, which proved to increase achievements scores in all areas vs. traditional teaching methods [26]. To make mI-PIV as powerful as possible in an educational context, it will also include an in-depth instructional feature that will guide students through the process of taking PIV measurements and provide access to resources for learning about PIV and fluid dynamics.

1.3 Laser Safety

1.3.1 Laser Classification

Since mI-PIV seeks to broaden the availability of PIV to as many people as possible, laser safety is of great importance to this project. OSHA and the FDA give very specific regulations for the classification of lasers and the rules associated with each of these classifications [8, 11]. The classification methods and rules that are most pertinent to the present research are summarized in this section.

The FDA classifies lasers according to an "Emission Limit" on five different quantities: radiant energy [J], radiant power (or radiant flux) [W], radiant exposure [$\mathrm{Jcm^{-2}}$], radiance [$\mathrm{Wcm^{-2}sr^{-1}}$], and integrated radiance [$\mathrm{Jcm^{-2}sr^{-1}}$]. Another important factor in the classification system is "Emission Duration" t_e [s]. Emission duration means how long the laser is on and the shutter is open at a time. For example, in PIV, emission duration should be at least the time a laser must be turned on (and the shutter to be open) to finish one

PIV measurement. If the laser is pulsed at a given pulsewidth τ_p for a given total length of time t_{tot} at a constant frequency f or period T, emission duration can be calculated as $t_e = \tau_p \frac{t_{tot}}{T} = \tau_p \times t_{tot} \times f$. The classification system used by the FDA for lasers with wavelengths of 400-700 nm is shown in Table 1.1. For a laser to belong to a certain class, it must not exceed the emission limit for the given emission duration t_e of the laser. A laser belongs in the lowest class that it qualifies for.

Lasers are often measured in radiant power Φ [W], which can be converted to radiant energy Q [J], radiant exposure H [Jcm^{-2}], radiance L [Wcm^{-2}sr^{-1}], and integrated radiance L_{int} [Jcm^{-2}sr^{-1}] using eqs. (1.2) to (1.5) [8]. In these equations, t_e is emission duration [s], A is area of exposure [cm^2] and ω is solid angle in steradians [sr]. These equations are useful in applying Table 1.1 to a laser with known values for these quantities.

$$Q = \Phi t_e \tag{1.2}$$

$$H = \frac{\Phi t_e}{A} \tag{1.3}$$

$$L = \frac{\Phi}{A\omega} \tag{1.4}$$

$$L_{int} = \frac{\Phi t_e}{A\omega} \tag{1.5}$$

Table 1.1 is somewhat complex and non-intuitive because some classes have multiple emission limit criteria and some of the emission limit criteria are a function of emission duration t_e. To further complicate matters, in order for a laser to be considered class I, it must not exceed BOTH the radiant power/energy criterion (shown in the top half of the class I row) AND the radiance/integrated radiance criterion (shown in the bottom half of the class I row). In other words, if it qualifies for either of these criteria by being under that criterion's emission limit, it IS considered a class I laser. Because of these complexities, an example is given for how to classify a laser using Table 1.1 in Section 1.3.2.

Table 1.1: Laser classification for lasers with wavelengths from 400 to 700 nm [8]. Reference [8] includes more wavelengths in its specifications, but only 400 to 700 nm is selected for this table, since green lasers (532 nm) are most common for PIV. Classifications are based on "Emission Limits," measured in in radiant power Φ [W], radiant energy Q [J], radiant exposure H [$\mathrm{Jcm^{-2}}$], radiance L [$\mathrm{Wcm^{-2}sr^{-1}}$], and/or integrated radiance L_{int} [$\mathrm{Jcm^{-2}sr^{-1}}$], depending on the classification. "Emission Duration, t_e [s]" is how long the laser emission is accessible to human contact. Usually this means how long the laser is on at a time. If the laser is pulsed at a given pulsewidth τ_p for a given total length of time t_{tot} at a constant frequency f or period T, emission duration can be calculated as $t_e = \tau_p \frac{t_{tot}}{T} = \tau_p \times t_{tot} \times f$. For a laser to belong to a given class, it must not exceed the emission limit for the given emission duration of the laser. Some emission limits are a flat value, such as with class II and III lasers. Other emission limits are dependent on emission duration t_e. Class I has seven different expressions for its emission limit, split into two separate rows. The limits according to t_e in *both* rows must be *exceeded* for the laser to *not* be considered class I. In other words, if the emission according to t_e is *under* the limit of *either* of these rows, it *is* considered class I. Class IIIb has two different expressions for power emission limit, depending on t_e. For more clarification, refer to the example given in this section.

Class	t_e **[s]**	**Emission Limit**	**Quantity**	**Unit**
I	$< 2 \times 10^{-5}$	2×10^{-7}	Q	J
	2×10^{-5} to 1×10^{1}	$7 \times 10^{-4} t_e^{3/4}$	Q	J
	1×10^{1} to 1×10^{4}	3.9×10^{-3}	Q	J
	$> 1 \times 10^{4}$	3.9×10^{-7}	Φ	W
	AND			
	$< 1 \times 10^{1}$	$10 t_e^{1/3}$	L_{int}	$\mathrm{Jcm^{-2}sr^{-1}}$
	1×10^{1} to 1×10^{4}	20	L_{int}	$\mathrm{Jcm^{-2}sr^{-1}}$
	$> 1 \times 10^{4}$	2×10^{-3}	L	$\mathrm{Wcm^{-2}sr^{-1}}$
IIa	$> 1 \times 10^{3}$	3.9×10^{-6}	Φ	W
II	$> 2.5 \times 10^{-1}$	1×10^{-3}	Φ	W
IIIa	$> 3.8 \times 10^{-4}$	5×10^{-3}	Φ	W
IIIb	$< 2.5 \times 10^{-1}$	$\min(10 t_e^{1/3}, 10)$	H	$\mathrm{Jcm^{-2}}$
	$> 2.5 \times 10^{-1}$	5×10^{-1}	Φ	W
IV	–	∞	–	–

1.3.2 Example - Laser Classification Using Table 1.1

A given laser has the following quantities:

$t_e = 2 \times 10^{-2}$ [s],

$\Phi = 1 \times 10^{-2}$ [W],

$D = 0.15$ [cm],

$\theta = 1.5 \times 10^{-3}$ [rad],

where D is diameter of the beam and θ is divergence of the beam. From these quantities, we can calculate the following important quantities:

$$A = 1/4\pi D^2 = 1/4\pi(0.15\ [\text{cm}])^2 = 1.77 \times 10^{-2}\ [\text{cm}^2]$$
$$\omega = \pi\theta^2 = \pi(1.5 \times 10^{-3}\ [\text{rad}])^2 = 7.07 \times 10^{-6}\ [\text{sr}]$$
$$Q = \Phi t_e = (1 \times 10^{-2}\ [\text{W}])(2 \times 10^{-2}\ [\text{s}]) = 2 \times 10^{-4}\ [\text{J}]$$
$$H = \frac{\Phi t_e}{A} = \frac{(1\times10^{-2}\ [\text{W}])(2\times10^{-2}\ [\text{s}])}{1.77\times10^{-2}\ [\text{cm}^2]} = 0.0113\ [\text{Jcm}^{-2}]$$
$$L = \frac{\Phi}{A\omega} = \frac{1\times10^{-2}\ [\text{W}]}{(1.77\times10^{-2}\ [\text{cm}^2])(7.07\times10^{-6}[\text{sr}])} = 8 \times 10^4\ [\text{Wcm}^{-2}\text{sr}^{-1}]$$
$$L_{int} = \frac{\Phi t_e}{A\omega} = \frac{(1\times10^{-2}\ [\text{W}])(2\times10^{-2}\ [\text{s}])}{(1.77\times10^{-2}\ [\text{cm}^2])(7.07\times10^{-6}[\text{sr}])} = 1.6 \times 10^3\ [\text{Jcm}^{-2}\text{sr}^{-1}]$$

We begin by finding whether or not this is a class I laser. The emission duration $t_e = 2 \times 10^{-2}$ [s] is between 2×10^{-5} and 1×10^{1} [s], so it will be classified according to the emission limit expressions in the second and sixth lines (The line that says "AND" is the fifth line) in the class I row. The emission limit for the radiant energy Q_{limit} criterion is calculated from the "Emission Limit" expression in the second line to be

$$Q_{limit} = 7 \times 10^{-4} t_e^{3/4} = 7 \times 10^{-4} \times (2 \times 10^{-2})^{3/4} = 3.7 \times 10^{-5}\ [\text{J}],$$

and the emission limit for integrated radiance $L_{int,limit}$ is calculated from the "Emission Limit" expression in the fifth line to be

$$L_{int,limit} = 10 t_e^{1/3} = 10 \times (2 \times 10^{-2})^{1/3} = 2.7\ [\text{Jcm}^{-2}\text{sr}^{-1}].$$

Since both the radiant energy Q and the integrated radiance L_{int} of this laser are above their respective class I emission limits, this is not a class I laser. It is also above the radiant power emission limits of class IIa, class II, and class IIIa lasers, so it is not class IIa, II or

IIIa. Since the emission duration is $< 2.5 \times 10^{-1}$ [s], the class IIIb emission limit for radiant exposure H_{limit} is calculated using the "Emission Limit" expression in the first line of the IIIb row, giving

$$H_{limit} = 10 t_e^{1/3} = 10 \times (2 \times 10^{-2})^{1/3} = 2.7 \text{ [Jcm}^{-2}\text{]}.$$

Since the radiant exposure H is below the class IIIb emission limit for radiant exposure H_{limit}, this is a class IIIb laser. If radiant exposure of the laser were anywhere above 2.7 [Jcm^{-2}] it would be a class IV laser.

1.3.3 Simplification of Laser Classification - Conversion of Quantities to Radiant Power Φ

In order to simplify the classification system given in Table 1.1, all emission limit quantities are converted to emission limit in radiant power Φ_{limit} by isolating Φ in eqs. (1.2) to (1.5) and then are plotted for a range of emission durations from 1×10^{-6} to 1×10^{6} in fig. 1.4. Since most cheap laser pointers sold online have beam diameter $D > 0.15$ [cm] and beam divergence $\theta > 1.5 \times 10^{-3}$ [rad] (at least those tested during the present research), these are conservative values and thus are used for calculating Φ_{limit}. For example, the class I emission limit for integrated radiance $L_{int,limit}$ at $t_e = 2 \times 10^{-2}$ [s] is converted to radiant power according to eq. (1.5) and the fifth line of the class I row in Table 1.1 and found to be

$$\Phi_{limit} = \frac{L_{int,limit} A \omega}{t_e} = \frac{10 t_e^{1/3} A \omega}{t_e} =$$

$$\frac{\left(\left(10(1.77 \times 10^{-2})\right) \text{[Jcm}^{-2}\text{sr}^{-1}\text{]}\right) \left(1.77 \times 10^{-2} \text{ [cm}^2\text{]}\right) \left(7.1 \times 10^{-6} \text{ [sr]}\right)}{2 \times 10^{-2} \text{ [s]}} = 1.70 \times 10^{-5} \text{ [W]}.$$

This happens to be less than the class I emission limit for radiant energy Q_{limit} at the same emission duration $t_e = 2 \times 10^{-2}$ [s], which, when converted to radiant power using eq. (1.2) and the second line of the class I row, is calculated as

$$\Phi_{limit} = \frac{Q_{limit}}{t_e} = \frac{7 \times 10^{-4} t_e^{3/4}}{t_e} = \frac{\left(7 \times 10^{-4}\right)(2 \times 10^{-2})^{1/4}\right) \text{ [J]}}{2 \times 10^{-2} \text{ [s]}} = 1.9 \times 10^{-3} \text{ [W]}.$$

Since only one of these emission limit criteria must be met to qualify a laser class I, the larger of the two emission limits in radiant power is chosen, and the emission limit for power Φ_{limit} at $t_e = 2 \times 10^{-2}$ [s] is plotted as 1.9×10^{-3} [W].

With the plot in fig. 1.4, it is much easier to classify a 400-700 nm laser with the specified $D = 0.15$ [cm] and $\theta = 1.5$ [rad] that this project is concerned with. For example, if a laser with these specifications has output power Φ of 2×10^{-3} [W] and emission duration $t_e = 1$ [s], it falls in the Class IIIa range, shown as the green area with the power emission limit ranging from 1×10^{-3} [W] to 5×10^{-3} [W] (see right axis).

1.3.4 Laser Regulations that Affect This Project

According to [8], a class I laser is considered non-hazardous, a class IIa laser is considered to be a chronic viewing hazard for time greater than 1000 [s], a class II laser is considered to be a chronic viewing hazard, a class IIIa laser is considered to be either an acute intrabeam viewing hazard or a chronic viewing hazard depending upon the irradiance, a class IIIb laser is considered to be an acute hazard to the skin and eyes from direct radiation, and a class IV laser is considered to be an acute hazard to the skin and eyes from direct and scattered radiation [8]. Protective eyewear is encouraged for class IIIb lasers and required for class IV lasers [11], as denoted by the images of eyewear in the plot in fig. 1.4. Class IV lasers can be extremely dangerous and thus have many restrictions [8, 11], as denoted by the "Danger" sign in the class IV regime in fig. 1.4. Other regulations associated with this classification system deal with protective housing, interlocks, laser controlled area, labels, and alignment procedures, to name a few. However, since protective eyewear seems to be a fairly intuitive standard for measuring how "safe" a particular laser is, special emphasis is put on this aspect of laser classification and regulation in the present study. For instance, because requiring safety eyewear for mI-PIV use would greatly magnify the burden (especially monetary) of high school teachers trying to introduce PIV to their students, it is desirable for mI-PIV to use laser output powers at or under 5 mW, if this is possible while still maintaining reasonably accurate PIV measurements.

Class II lasers and lower are not suitable for PIV, at least not with a smartphone

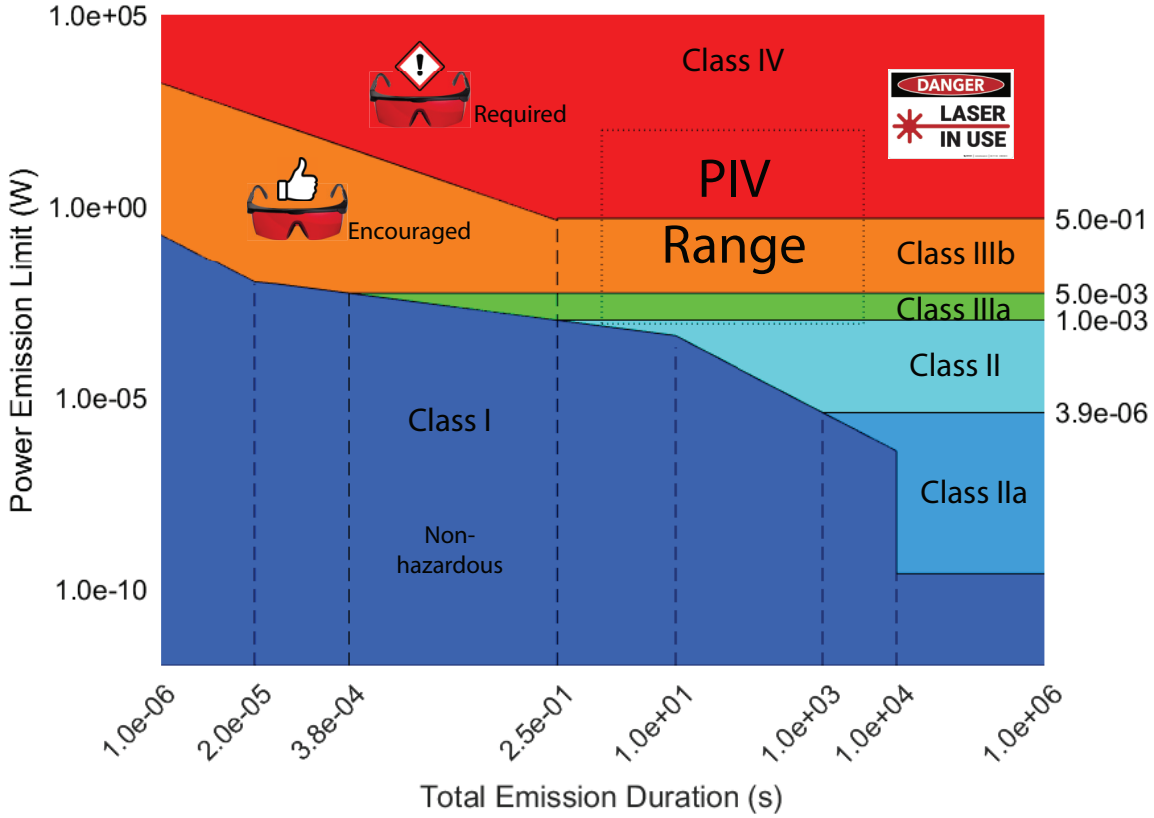

Fig. 1.4: Laser classification regime plot for wavelengths of 400 to 700 nm. This plot is derived from Table 1.1 [8]. A beam diameter of 0.15 [cm] is assumed, giving an area of exposure of $A = \pi r^2 = \pi(0.15\ [\text{cm}])^2 = 0.0177\ \text{cm}^2$. Also, a beam divergence of $\theta = 1.5 \times 10^{-3}$ [rad] is assumed, which, when made to be the apex angle of a cone (the assumed shape of a laser beam), is equivalent to a solid angle of about $\omega = \pi\theta^2 = \pi(1.5 \times 10^{-3}\ [\text{rad}])^2 = 7 \times 10^{-6}$ [sr]. Protective eyewear is encouraged for class IIIb lasers and required for class IV lasers, as denoted by the images of eyewear in the plot. Class IV lasers can be extremely dangerous and have many restrictions, as denoted by the "Danger" sign in the class IV regime. The (approximate) bounds for laser output power for PIV are from 1 [mW] to 100 [W]. Also, PIV experiments are generally done within a time of 1 [s] to 3600 [s].

camera, because they cannot illuminate the particles enough for the smartphone camera's sensor to detect light (this finding is described in Section 3.4.3). Because of this, the approximate lower bound for laser output power in PIV is around 1 [mW]. Usually, high-powered lasers give an output power of < 100 [W], so this acts as the approximate upper bound for PIV laser output power. Also, PIV experiments are generally done within a time of 1 [s] to 3600 [s]. All four of these approximated bounds are shown in the plot in fig. 1.4 by the dotted bounding box labeled "PIV Range."

These guidelines and regulations play a prominent role in the mI-PIV project. Because class IIIb lasers are considered to be hazardous to the skin and safety eyewear is recommended for their use, the mI-PIV project aims to keep laser power of the system at or under 5 [mW] in order to stay in the class IIIa range. However, since class II and lower lasers are not suitable for PIV, the laser output power must remain above 1 [mW]. This results in a fairly narrow range of laser power that is appropriate for this project: 1 mW to 5 mW. Another issue that is discussed in Section 3.4.1 is that laser output power is expected to be directly correlated to accuracy of the system, since extremely low powers give weak particle illumination, which leads to weak contrast of particle images with the background and a weak correlation signal. Therefore, an output power must be chosen that balances safety and accuracy to optimize the system. In Section 2.3, one idea that is brought forth to combat this issue is a system that utilizes two 5 [mW] lasers to increase overall particle illumination while remaining under (or at) the IIIa classification limit.

1.4 Simplified PIV Systems

In recent years there has been an interest in designing PIV systems that are more practical than traditional PIV systems, sacrificing lab-grade accuracy for lower cost. One of the main reasons for this is to make PIV more accessible to lower education. Here, a range of such simplified systems is described, as well as their application to the mI-PIV project.

1.4.1 History of Simplified PIV Systems

In 2001, Chetelat *et al.* [20] produced a Miniature PIV (MPIV) system that used a low-powered laser pointer with a digital CMOS camera for image acquisition, introducing the idea of a PIV system that gives modest performance compared to traditional systems but is much less expensive. This opened the door for many similar designs, all of which called for use of less expensive lasers, cameras, particles, and/or synchronizers (or no synchronizer at all) in their proposed systems. These systems were shown to be capable of measuring uniform flows [20], vortex shedding behind multiple shaped cylinders [18, 27], jets of both water and air [6, 21, 25], swirl flows [22], T-junction flows [24], surface flows [19], disturbances of water from a leaping frog [23], and vortices in the air from flicking snake tongues [25], and were able to give accurate – though perhaps not lab-grade accurate – measurements at a fraction of the price of a traditional lab-grade PIV system. By "lab-grade," what is meant is a system that uses reasonably state-of-the art equipment to attempt to maximize accuracy and precision as much as possible.

1.4.2 Smartphones in PIV

The work of [19] was the first PIV system to use a mobile device for image acquisition. This publication describes a mobile phone application built for measuring the velocity of surface flows for industrial use. The tool is made to take advantage of debris, bubbles, or other particular/granular items on the surface of a flow and perform PIV on those "particles," using an innovative orthorectification algorithm to adjust for the angle of image acquisition with respect to the surface of the flow. Although this system was tested on synthetic images from a PIV Challenge (it is unclear whether they used images from the 1st [28], 2nd [29], 3rd [30], or 4th [13] PIV Challenge), it was not quantitatively tested on an actual surface flow, therefore it cannot be determined whether it is a viable PIV measurement tool for use in a setting where accuracy is important. However, this work brought to light the possibility of both image capture and PIV image correlation on a mobile phone.

In [6], a mobile device was also used for image acquisition but a computer was used for the PIV algorithms, and a 1-Watt CW laser (class IV) was used for particle illumination.

Images of a jet were taken with a mobile phone and with a scientific high-speed camera simultaneously and PIV was performed on both sets of images. Error of the mobile phone PIV was then found by subtracting velocity measurements from the velocity measurements taken with the scientific high-speed camera. Since a high-power laser is used for [6], this study does not show what results can be obtained when using a low-power (1 mW - 50 mW) laser, and therefore the findings therein are not directly transferable to the mI-PIV system. However, it brought to light some important guiding principles to aid in developing the general use of mobile phones in PIV, some of which are:

1. Reasonable PIV accuracy can be achieved using the video function of a mobile phone camera and parsing the frames for PIV image acquisition.

2. Since a mobile phone video camera uses a "rolling shutter," in which only sections of an image are scanned at a time, a pulsing laser cannot be used. Thus, the mI-PIV system must use a CW laser. Since pulsed lasers are necessary when measuring rapid flows in order to eliminate particle streaking, it can then be inferred that there must be some limit to the flow velocity that can be measured with reasonable accuracy by the mI-PIV system.

3. For a higher-velocity flow, a higher frame rate is recommended to reduce error due to loss of pairs from in-plane motion. Since most mobile phones are only capable of 240 fps or lower, this is another limitation that bars measuring fast flows with the mI-PIV system.

Another work that utilized mobile phones for PIV is described in the work of [7], in which different-colored LEDs are used with a set of four mobile phone cameras to perform tomographic PIV on a vortex ring. This setup was compared against a commercial stereoscopic PIV setup to measure accuracy. The system in [7] is different in nature than the mI-PIV system. For example, it takes volumetric PIV measurements as opposed to planar, and it uses shadows of opaque particles instead of light scattered from reflective

particles. However, this system reinforces the findings of [6, 19] that mobile phone cameras have potential as effective tools for PIV image acquisition.

1.4.3 Laser Power - Cost Comparison of Existing Systems and mI-PIV

The cost and laser output power of all the aforementioned systems are plotted on a logarithmic scale in fig. 1.5. The mI-PIV system is also plotted for comparison. It is shown that mI-PIV uses a laser output power that is significantly lower than almost any other system besides that of Chetelat *et al.* [20] and "ePIV" and is significantly less expensive than all systems. This lower cost of the system is mainly due to the use of a mobile phone for image acquisition, and also due to the use of a very low-power and inexpensive laser pointer. The mobile phone is not included in the cost of mI-PIV, since it is assumed that the user will have a mobile phone of their own, and the app will be designed for compatibility with any Android device. This means the cost for mI-PIV is only based on the laser/optic system. The same applies to the system designed by Cierpka *et al.*, since a mobile phone was utilized for their image acquisition as well, but the laser used for their study was much more expensive. Although mI-PIV laser output power is low, the mI-PIV system still gives reasonable accuracy for slow flows, as discussed in further detail in Section 3.4.3. The vertical dotted line at 0.005 W (5 mW) shows the cutoff laser output power from class IIIa to IIIb, as outlined in Section 1.3.3. Starting at class IIIb, OSHA and the FDA begin to suggest the use of eye protection [8, 11], and for use of class IV lasers, they require the use of eye protection. The mI-PIV system seeks to have the highest possible laser output power – which is assumed to correspond to the highest possible accuracy (this assumption is proven to be correct in Section 3.4.3) – while remaining in the class IIIa range, where eye protection is not required or even encouraged. This puts the desired laser output for the mI-PIV system at 0.005 W (5 mW).

The plot in fig. 1.5 does not include more complicated variables such as the quality/accuracy of the PIV system, ease of setup, the velocity ranges and types of flows that can be measured, etc. Variables such as these are non-homogeneous among the different systems and are therefore impossible to compare. For example, Cierpka *et al.* [6] uses mean bias

error as a metric (with a lab-grade system for ground truth), Ryerson and Schwenk [25] use percent error of volume flow rate, and Chetelat *et al.*'s [20] experimental results are completely observational/qualitative. Also, most of the PIV systems were tested on entirely different flows, as mentioned in Section 1.4.1, making a flow-type comparison impossible. Because of such limitations, more complicated variables such as these are not compared in this plot, and therefore it does not give a perfect or exhaustive description of the relationship between each system, nor does it show that any particular system is "better" or "worse" overall than any other. However, a cost v. laser output power plot such as in fig. 1.5 is useful in showing the practicality of the mI-PIV system with respect to other systems currently in use, and for demonstrating its potential as a solution for introducing PIV to a broader range of students.

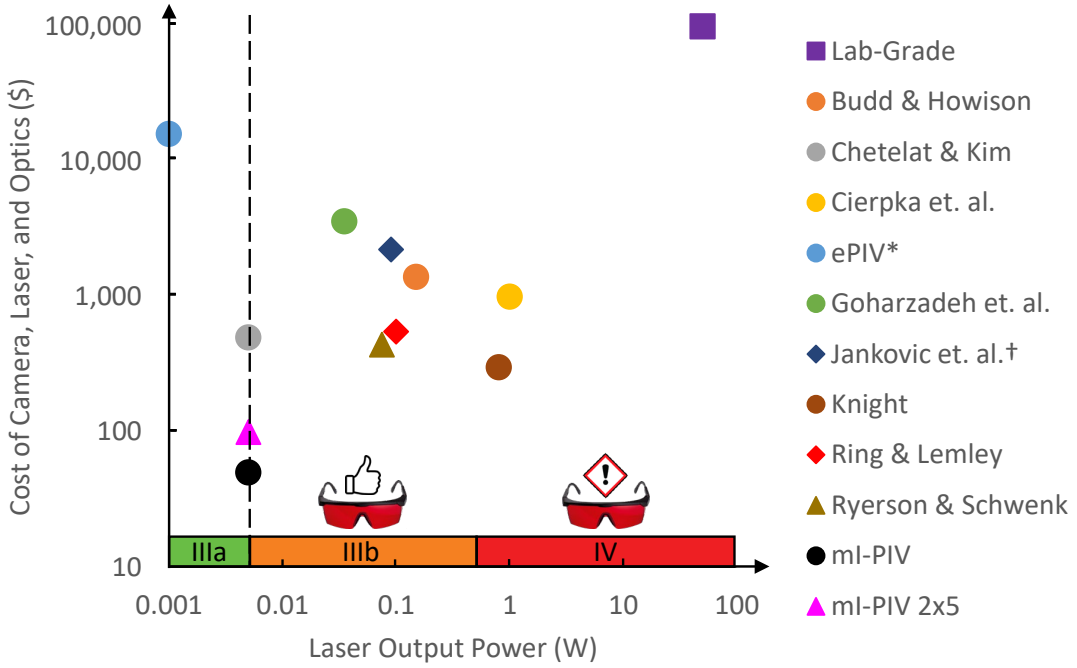

Fig. 1.5: Cost vs. laser output power comparison of different proposed simplified PIV systems, as described in their respective publications. For laser power, a horizontal bar is used to represent the vertical power range in the "PIV Range" bounding box in fig. 1.4, which includes class IIIa, class IIIb, and class IV laser output powers. This bar is shown to describe the classification of lasers according to their output power, as given by [8, 11]. To the right of the vertical dashed line at 0.005 W (5 mW) is the IIIb classification, for which users are encouraged by OSHA and the FDA to wear laser eye protection, as shown by the "thumbs-up" symbol and the eyewear image above the class IIIb range. For class IV lasers, which are lasers over 0.5 W (500 mW), eye protection is required, shown by the "warning" sign and the eyewear image above the class IV range. The cost for the mI-PIV system does not include the cost of the mobile device, since it is assumed that the user will have a mobile device of their own. The app will be designed for compatibility with any Android device. The "mI-PIV 2x5" data point represents a double-laser system described in Section 2.3.

* ePIV comes as a packaged product and therefore all components are included in cost. Although a class IIIb laser is used, everything is enclosed in this system, even the laser, and is not accessible to students, therefore ePIV is given the lowest possible laser output power rating for the purpose of this comparison.

† Jankovic *et al.* only provided overall cost of the system, so that is what is shown here, as opposed to only the cost of the laser and camera like shown for the other systems

CHAPTER 2

Design of the mI-PIV System

2.1 Objectives of the mI-PIV Project

The mI-PIV project is funded by the Office of Naval Research with the intent of allowing greater student access to hands-on learning of fluid dynamics principles with PIV, an important modern fluid dynamics tool. The Navy, having many applications in fluid dynamics, has a special interest in equipping today's students and tomorrow's workforce with deep knowledge of fluids concepts, as well as skill in related technologies such as PIV. In this light, the mI-PIV project seeks to make PIV available to a much broader range of users than at present, particularly high school classrooms, by having a very inexpensive and completely safe design, as well as a built-in instructional aspect. Also, maintaining accuracy that is acceptable for undergraduate laboratories is important in ensuring high-quality learning opportunities for both high school and undergraduate students. Specifically, goals [31, 32] for the mI-PIV project include:

1. Design a graphical user interface (GUI) mobile application that:
   (a) performs planar PIV on simple fluid flows with measurement accuracy within an appropriate margin of error for educational use.
   (b) is free to download, open-source, and archived on open and accessible repositories such as GitHub.
   (c) is able to operate completely on an Android mobile device (no external computers are needed) by having all functions written into the mobile device application in JAVA.
   (d) includes an intuitive and instructional guided user interface that:

i. provides users, who may be PIV novices, a step-by-step process for setting up and troubleshooting PIV experiments

ii. engages users in learning about PIV techniques and laser safety

iii. guides users in interpreting experimental PIV results to connect visual, data representations with physical and mathematical concepts from fluid mechanics

iv. includes easy access, search-able user guide information

2. Design a simple, low-cost, class IIIa continuous wave laser/optics system that will be used for safe and economical particle illumination in a darkened room without eye protection, to be used for PIV in conjunction with the mI-PIV app.

3. Develop supporting curricular materials, such as flow experiments, for high school and undergraduate use of the mI-PIV system and disseminate those materials with the mI-PIV system throughout Navy STEM, engineering education, and fluids engineering communities.

2.2 Mobile Application

2.2.1 Code

The mI-PIV app is currently in the design process and therefore many factors are subject to change until August 2021, which is the proposed delivery date. The current prototype of the mI-PIV app relies on a server to perform PIV on the images acquired by the mobile device camera. The end goal is to have all computation be done on the mobile device itself, removing any need for a computer before, during, or after a mI-PIV experiment.

The server uses OpenPIV [1], an open-source PIV package, for PIV processing of the images. OpenPIV has several different PIV methods with different approaches to applying PIV algorithms. Some such methods include direct cross correlation, FFT correlation, single pass, and a window displacement iterative method (WiDIM) based on the approach

given in [33], which is similar to the discrete window offset described by [34] and the image deformation technique described by [35]. The current mI-PIV application uses the WiDIM method. This method splits the FOV into a gird of interrogation regions or windows, then correlates an image pair at each window (as most PIV algorithms do), then for the next iteration it shifts the window according to the displacement prediction of the previous iteration. This increases the particles that remain in the window, as opposed to a single-pass or fixed grid algorithm, and in turn gives a better correlation signal for each iteration than would be possible with one of these simpler algorithms.

In order to have the mI-PIV application operate completely on the mobile phone, it must be written in JAVA, which is the language for most Android devices. Therefore, all functions, including the GUI, video parsing, image processing, and PIV algorithms — including PIV preprocessing and PIV postprocessing — must be written in JAVA. This constraint does not allow for the use of OpenPIV for the PIV algorithms because OpenPIV is based on MATLAB, Python, and C++. Therefore, mI-PIV code must be designed mostly by hand in JAVA, although some functions could potentially be ported from OpenPIV or JPIV [5], another open source PIV program written in JAVA. Originally the intention was to simply write the JPIV code directly into the app, but it was found that this software is dependent on a package called "AWS" that is not supported on Android. For these reasons, the PIV code for the mI-PIV app must be written largely by hand. However, ideas will be pulled from OpenPIV, JPIV, and PIVlab [2, 3, 4], another widely-used open-source code.

The future JAVA code is projected to use a scheme similar to the WiDIM algorithm that OpenPIV implements. It is projected to include a multipass algorithm, which is a proven technique to improve accuracy and is included in most advanced modern PIV algorithms [10, 13, 15, 33, 34, 35]. It will likely also draw from window shifting code written in JPIV and PIVlab.

At this point in the project, no parameters of the PIV algorithm, such as window size, number of passes, etc., can be adjusted within the GUI. This is due to the necessity of testing on a simplest-case basis for the beginning of the project, and will likely change

in the future. It is important for the user to be able to adjust certain parameters in a PIV program. For example, most programs allow window size adjustment in order to vary spatial resolution and valid detection probability [14, 36] and to help the user accommodate the "1/4 Rule" [37], a generally-accepted guideline stating that optimal accuracy is given when in-plane displacements are kept under 1/4 of the window size.

2.2.2 Flow of GUI

The basic flow of the mI-PIV GUI is shown in fig. 2.1. The simplest form of image acquisition with mobile phones is taking video of the flow and parsing the video's frames. Therefore, this is the main method of image acquisition of the mI-PIV app, as shown in fig. 2.1(a), although it is possible to import images that have been acquired elsewhere. The app uses the mobile device's internal video camera for video capture — fig. 2.1(b) — and then parses the video into images. The user then chooses the images they want to make an image pair — fig. 2.1(c) — and can toggle between the two — fig. 2.1(d). If the user decides to process the image pair, that image pair is processed and a vectormap is shown to the user, which they can then save if they desire to do so — fig. 2.1(e).

2.3 Lighting Device

In order to accommodate the strict safety requirements described in Section 1.3.4, and to lower cost as much as possible, a laser optics system was designed that positioned a glass stir stick in-line with a simple inexpensive laser pointer to create a laser sheet, as shown in the rendering and the exploded view in fig. 2.2. The frame aligning the glass stir stick with the laser beam is intended to be 3D printed, and accounts for most of the projected cost of the system. A glass stir stick was found to produce a laser sheet in a similar fashion to other sheet optic lenses, and although it was previously unknown whether this optic lens would give comparable PIV accuracy to an actual optic lens, Section 3.7.2 details a comparison between the two lens types and Section 3.7.3 gives the findings of that test. In summary, the findings show that the design described here is an effective sheet optic design, at least for low-light, non-lab-grade PIV.

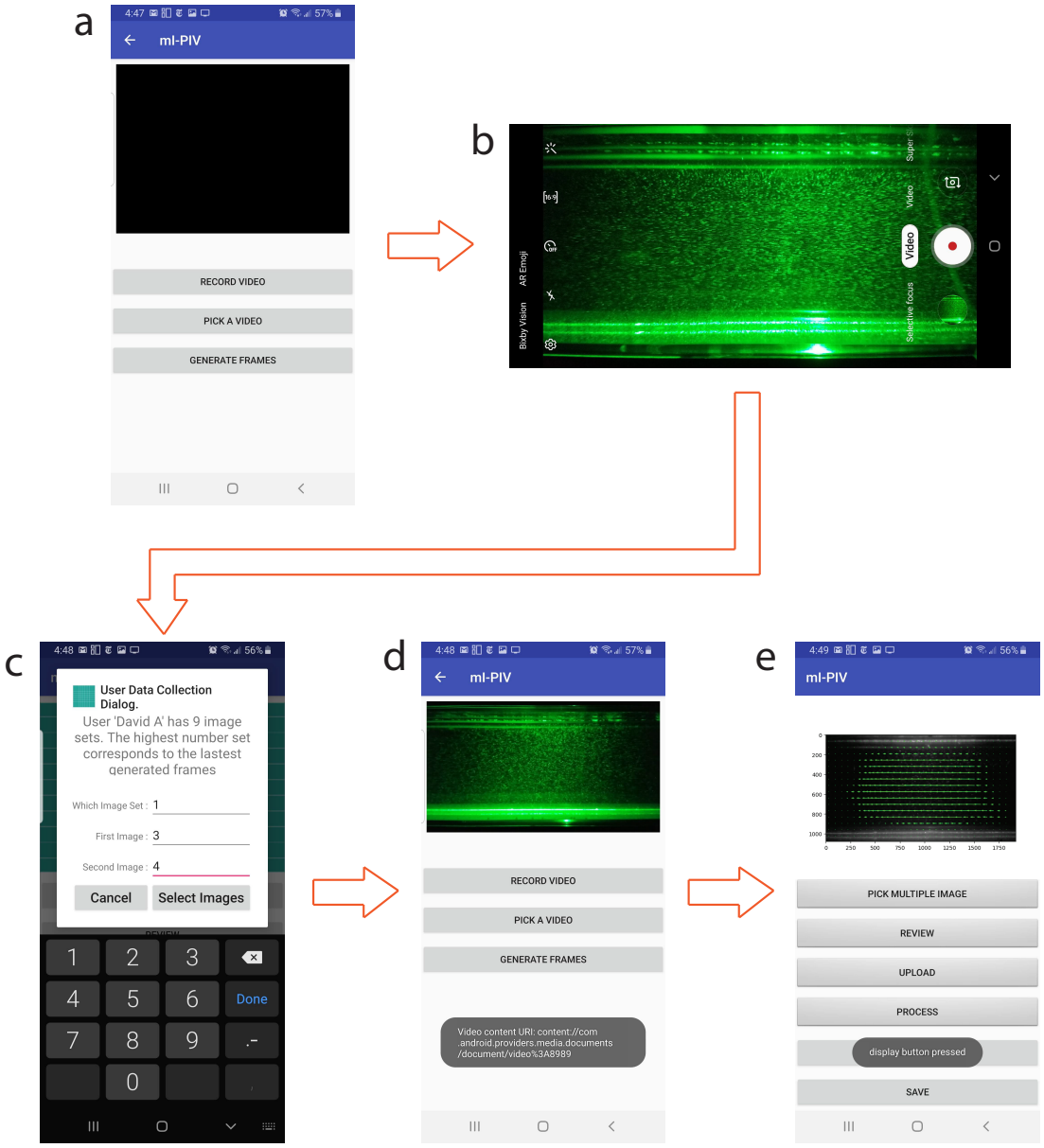

Fig. 2.1: Flow of the app, shown with screenshots of an actual experiment done using the mI-PIV app. These are only the main steps that are done in the actual app, which has a few more steps and may be further streamlined in the future. Step (a) shows the decision of recording a video or picking a video that is already saved onto the mobile device. Step (b) shows the mobile phone's camera app which is accessed by the mI-PIV app for image acquisition. Frames are parsed from the video and step (c) shows where two of those images are selected to make an image pair. Step (d) shows where the images are shown to the user, who then decides whether to process the images or to start over. Step (e) shows the vector field obtained.

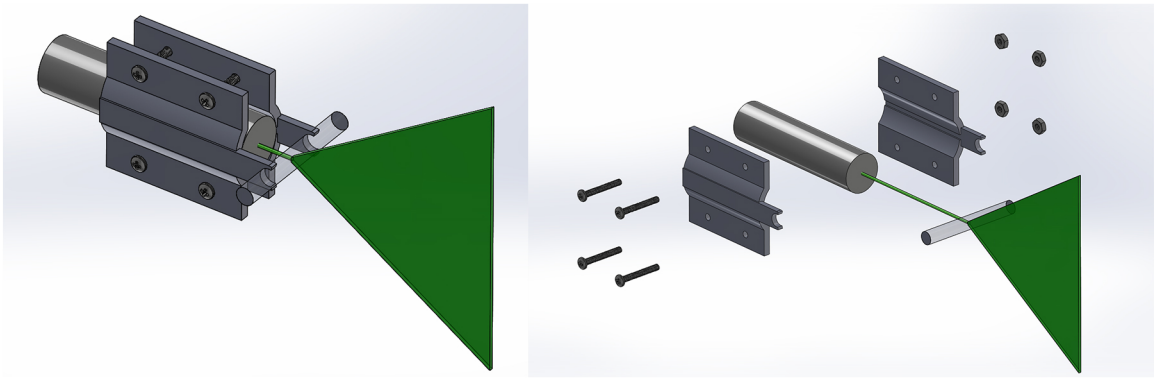

Fig. 2.2: Rendering of the laser-optics device

A design was made that could potentially serve to increase the illumination of particles while retaining the IIIa classification of the lasers for the mI-PIV system. This design consists of two 5 mW lasers, aligned to form one light sheet, as shown in the rendering in fig. 2.3. By increasing the total light in the light sheet, the particles images could potentially have better contrast with the background, and accuracy could thus be increased compared to a single 5 mW laser. It is hypothesized that the laser sheet produced by two aligned 5 mW laser should produce a light sheet equivalent to 10 mW and thus perform similarly to a single 10 mW laser. Evidence of the validity of this hypothesis is given in Section 3.6.3. The double-laser design is classified differently than a single 10 mW laser because when formed into a sheet, only a small fraction of the total laser radiation can enter the eye at a time, as opposed to a laser beam that can enter the pupil all at once.

2.4 Flow Experiments

Due to the slow frame rate of the mI-PIV camera (30 fps), the flow rate of mI-PIV experiments is limited to slow flows. The specific theoretical limitation of the flow velocity for a given experiment is discussed in Appendix A. To help accommodate for this limitation, several flow experiment ideas have been developed as part of this project. These experiments were not made to benchmark the mI-PIV system, but they do serve to demonstrate some particular experiments for which the mI-PIV system gives reasonable particle displacement measurements. A more thorough and quantitative benchmarking of the mI-PIV system

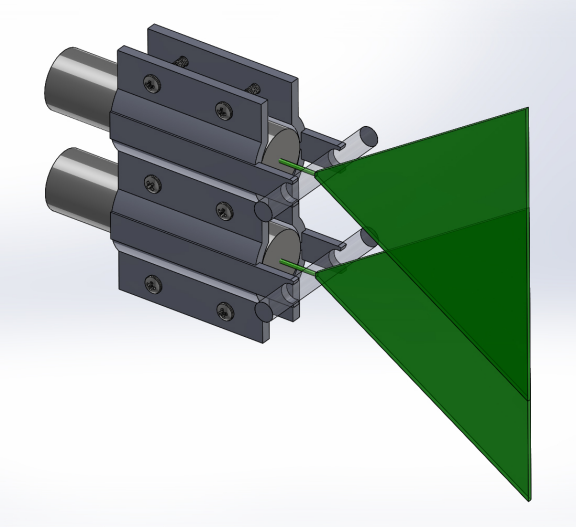

Fig. 2.3: Rendering of the double-laser device

with a steady-state, uniform flow is included in Chapter 3 of this work.

2.4.1 Laminar Entrance Length in a Square Pipe

An experiment was made to visualize the entrance length of a laminar pipe flow, similar to the experiment done with lab-grade PIV equipment in [38]. A square acrylic pipe was purchased from ePlastics and a pump was attached to cycle water at a steady rate through the pipe, with flow meters attached to measure flow rate, as shown in fig. 2.4, where (a) is a view of the entire setup and (b) is a zoomed crop that shows the mI-PIV components — the laser optic device and the mobile phone camera. The water was seeded with PIV particles (polyamid seeding particles) and the mI-PIV mobile phone application was used to analyze the flow. Figure 2.4 (c) shows a zoomed crop that shows an example of the mI-PIV components acquiring images. Specifications of equipment used are given in Appendix B.

For a given flow entering a pipe, the distance before fully developed flow, or "entrance length", is given by [39] to be eq. (2.1), where Re is Reynold's Number and D_h is hydraulic diameter. Although this equation assumes uniform inflow, which this setup did not achieve, it is still used for approximation of entrance length to *approximate* the capability of the mI-PIV system. For a square pipe, D_h is equal to the width or height of the pipe [39]. Re is

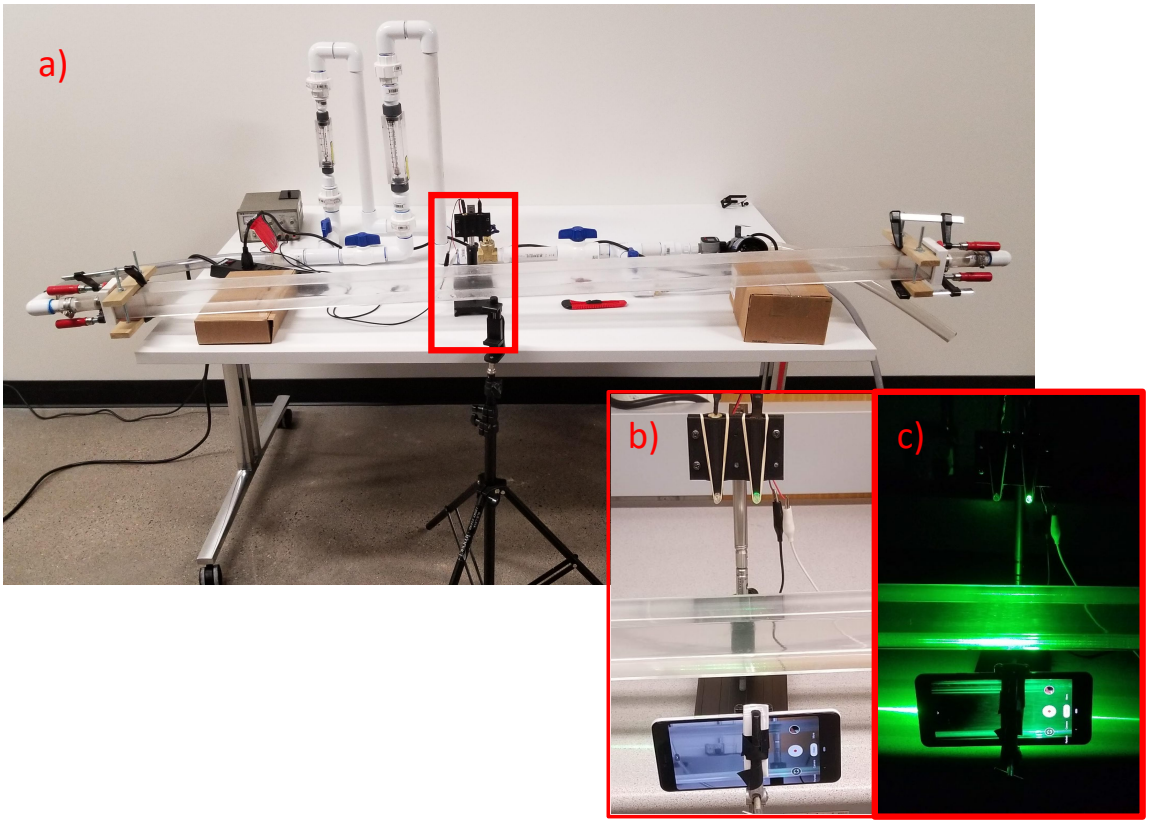

Fig. 2.4: (a) Photo of setup for square pipe experiment. (b) Zoomed crop that shows the mI-PIV components (the laser optic device and the mobile phone camera). (c) Zoomed crop that shows the mI-PIV components acquiring images.

given by eq. (2.2), where v is average velocity, D_h is hydraulic diameter, and ν is kinematic viscosity. Combining eqs. (2.1) and (2.2) and rearranging to isolate v, eq. (2.3) is obtained. Equation (2.3) gives the average velocity that corresponds to a particular entrance length, which is useful given a fixed length of pipe, such as was the case for this experiment.

$$L_{E,laminar} = 0.06 \times D_h \times Re \tag{2.1}$$

$$Re = \frac{vD_h}{\nu} \tag{2.2}$$

$$v = \frac{\nu L_{E,laminar}}{0.06 D_h^2} \tag{2.3}$$

In this setup, it is known that:

$D = 2$ [in] $= 0.051$ [m]
$\nu \approx 1 \times 10^{-6}$ [m^2/s]
$L_{E,laminar} = 3.75$ [ft] $= 45$ [in] $= 1.14$ [m]

where $L_{E,laminar}$ is chosen as less than the length of the pipe (about 5 [ft]), which will be the limiting factor in the allowed v. Substituting these values into eq. (2.3) gives

$v = 0.0074$ [m/s].

Flow rate can then be found using eq. (2.4), where A_C is cross-sectional area, v is velocity, and D_h is hydraulic diameter.

$$Q = vA_C = vD_h^2 \tag{2.4}$$

Substituting the known values of D_h and v into eq. (2.4), it is found that $Q = 1.90 \times 10^{-5}$ [m^3/s] $= 0.3$ [GPM]. With this flow rate known to correspond to an entrance length of 3.75

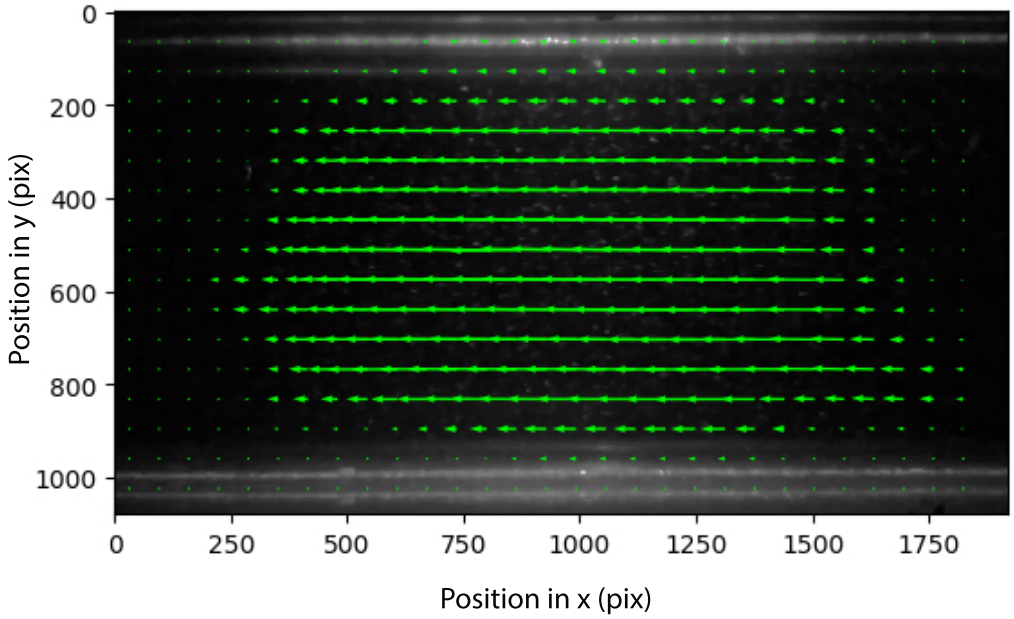

Fig. 2.5: Vector output from mI-PIV app for square pipe experiment

[ft], the pump was set to 0.3 [GPM] and the mI-PIV app was used to take measurements at 3.75 [ft] downstream of the entrance of the flow into the square pipe for this experiment. The resulting vectors are shown in fig. 2.5. The background in fig. 2.5 is an example image that was parsed from the video taken with the mobile phone camera. Since the mI-PIV app does not yet have the capability of selecting a region of interest (ROI), the PIV is performed on the entire image, which includes some area outside of the ROI. The ROI is bounded on the top and bottom where laser sheet crosses the inside of the square pipe, shown as the brightest horizontal lines at the top and bottom of the flow.

The analytical solution to the flow profile in a rectangular duct with the cross-sectional area shown in fig. 2.6 [12] is given to be eq. (2.5)[12], where a is 1/2 the width of the pipe, b is 1/2 the height of the pipe, x is position in the a-direction (with zero in the middle of the pipe), y is position in the b-direction (with zero in the middle of the pipe), μ is dynamic viscosity, and $-\frac{dp}{dz}$ is the pressure gradient. Pressure gradient $-\frac{dp}{dz}$ is given by eq. (2.6), where Q is flow rate. Equation (2.6) is not the exact equation given in [12], but has been algebraically manipulated to isolate the pressure gradient term $-\frac{dp}{dz}$.

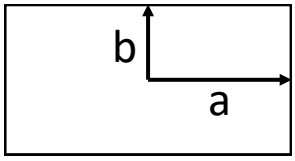

Fig. 2.6: Cross section of a rectangular pipe as given by [12]

$$u_z(x,y) = \frac{16a^2}{\mu\pi^3}\left(-\frac{dp}{dz}\right)\sum_{i=1,3,5...}^{\infty}(-1)^{\frac{i-1}{2}}\left[1-\frac{\cosh(i\pi y/2a)}{\cosh(i\pi b/2a)}\right]\left(\frac{\cos(i\pi x/2a)}{i^3}\right) \tag{2.5}$$

$$-\frac{dp}{dz} = \frac{3\mu Q}{4ba^3}\left[1-\frac{192a}{\pi^5 b}\sum_{i=1,3,5...}^{\infty}\frac{\tanh(i\pi b/2a)}{i^5}\right]^{-1} \tag{2.6}$$

A flow profile was made from the average values of the vectors and is shown in fig. 2.7 in comparison with the theoretical flow profile calculated using eqs. (2.5) and (2.6). In this plot, both displacement profiles are normalized from 0 to 1. The y-axis represents the ratio of the y-position y to the height of the image H, and the x-axis represents the normalized displacement in the x-direction.

It is reiterated that PIV was performed on the entire image, so the regions from 0.43 to 0.5 (bottom) and from -0.41 to -0.5 (top) on the y-axis were on regions outside of the pipe, and the theoretical velocity was set to zero there. This also explains the erroneous mI-PIV readings in those regions. However, in the majority of the area (from -0.41 to 0.43) of the y-axis, the mI-PIV readings closely follow the theoretical velocity profile, even near the inner edges of the pipe. This proof-of-concept analysis shows not only that the mI-PIV mobile phone application gave measurements that were expected, but that the flow experiment in question gave a flow that closely resembles a fully developed flow at the entrance length calculated. Therefore, this flow experiment is recommended for use with the mI-PIV application to give an effective visual demonstration of entrance length and fully developed flow.

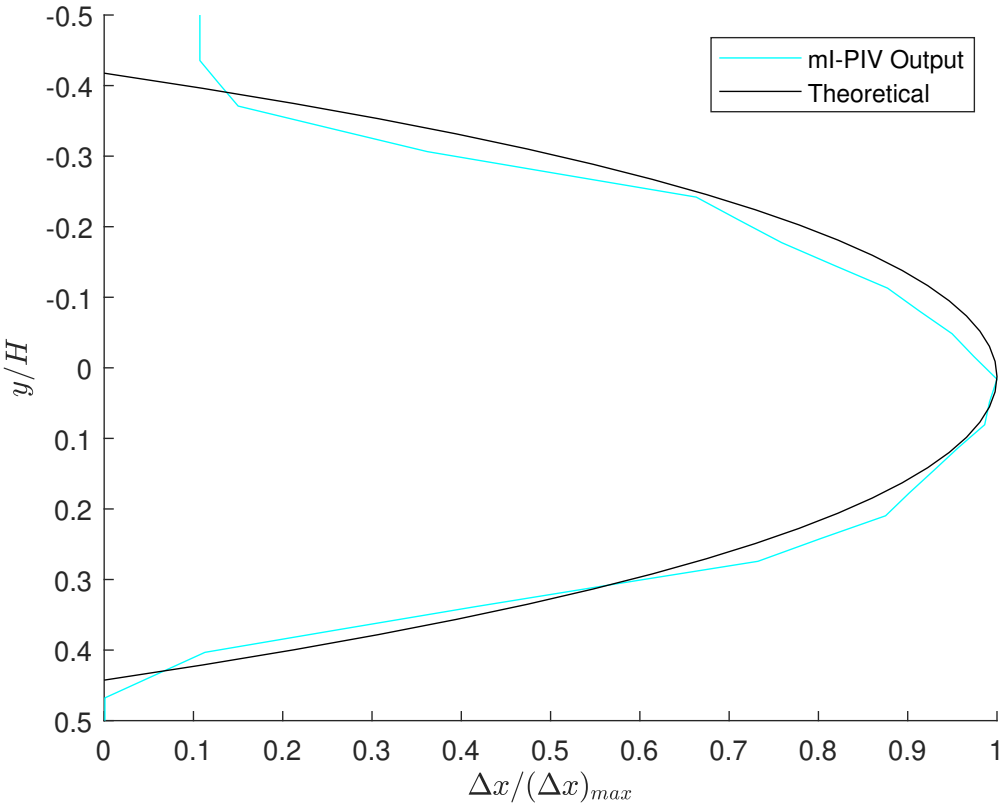

Fig. 2.7: Comparison of flow profile given by mI-PIV and theoretical flow profile as given by [12]

2.4.2 Downward Jet

Using a small fish tank pump, a jet was made with PVC pipe that ejected water downward into a fish tank. This jet was analyzed with a mobile phone camera and the mI-PIV laser-optic device, as shown in fig. 2.8(a), and then with a lab-grade setup, as shown in fig. 2.8(b). For technical details about the mI-PIV system and the lab-grade system, refer to the benchmarking setup described in Section 3.3. Also, specifications of equipment used are given in Appendix B. PIV was taken on an ROI directly below the mouth of the jet with the mI-PIV setup, as shown by the mI-PIV image in fig. 2.9, resulting in the output vectors in fig. 2.10(a). Then PIV was taken on the same ROI with the lab-grade setup, resulting in the output vectors in fig. 2.10(b). Both mI-PIV and lab-grade image sets were analyzed using PIVlab with a 2-pass multipass algorithm, with a 64x64 pixel window size for the first pass and a 32x32 pixel window size for the second pass. No preprocessing was done on the images. For postprocessing, vectors that were more than 5 standard deviations from their surrounding vectors were replaced with the average of their surrounding vectors. The measurements taken with the mI-PIV setup, although not exactly equal to the lab-grade measurements at all points of the ROI, shows a reasonable representation of the flow. This shows that this flow experiment is an effective way to demonstrate the mI-PIV app as a method for velocity measurement.

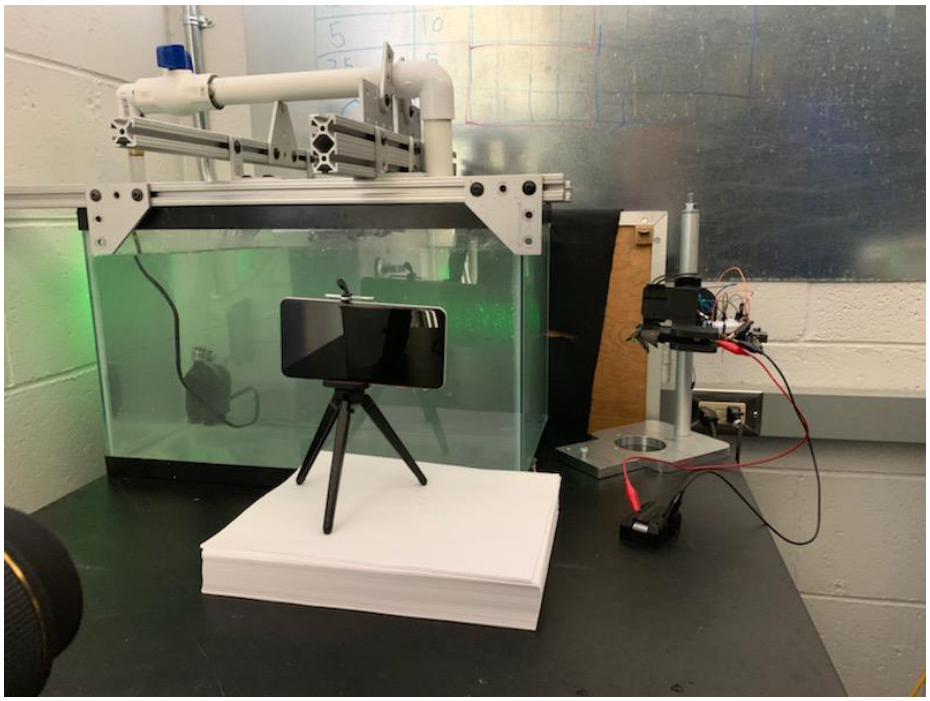

(a)

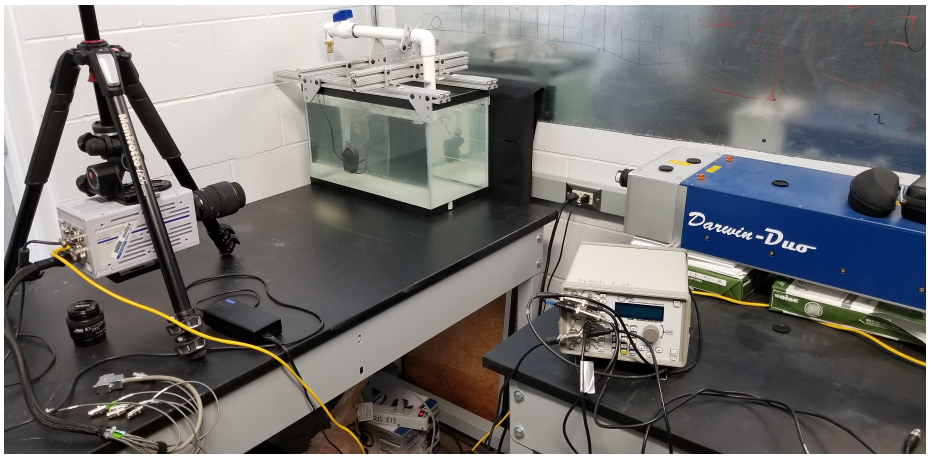

(b)

Fig. 2.8: (a) Lab-grade PIV output for downward jet (b) PIVlab output from mI-PIV laser and mobile phone camera for downward jet

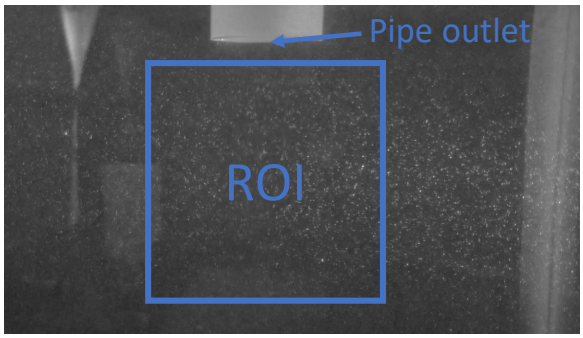

Fig. 2.9: Diagram showing the ROI analyzed by PIVlab on images obtained by the mI-PIV mobile phone and laser, as well as the lab-grade laser, camera, and syncronizer.

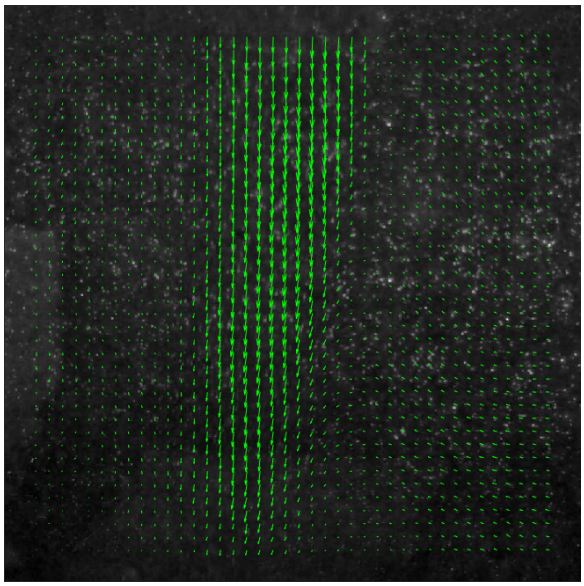

(a)

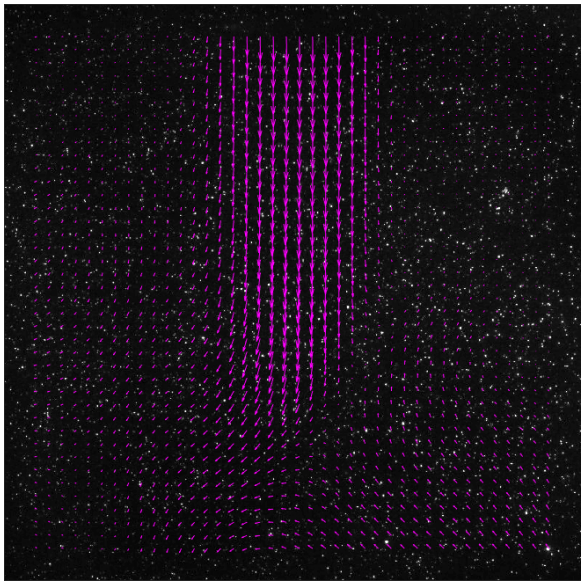

(b)

Fig. 2.10: (a) PIVlab output for downward jet using lab-grade images (b) PIVlab output from images taken with mI-PIV laser and mobile phone camera.

CHAPTER 3

Benchmarking the mI-PIV System

3.1 Benchmarking Approach for the mI-PIV System

The design of the mI-PIV app and system is currently under development through a process known as "design-based research" (DBR) [31]. Design-based research is an iterative process that involves forming a tentative design based on desired outcomes, past research, and known constraints and limitations, then implementing that design in educational settings in order to find potential improvements, then applying those improvements to the next iteration of the design and starting the process over again. As part of this process, several different parameters relating to the mI-PIV system were tested to find their effect on the accuracy of the system. These parameters have effects on safety, cost, and ease of use, so this knowledge, once obtained, would allow for more educated decisions throughout the design-based research process. Table 3.1 outlines the parameters that were tested, the different values of those parameters that were tested, and the ground truth that the system was tested against for those parameters.

For the physical components, the mI-PIV measurements were benchmarked for accuracy against a lab-grade PIV system, which acted as ground truth, as described in Section 3.3. For benchmarking of PIV algorithms, synthetic images were used and accuracy of the different algorithms was compared, as described in Section 3.9.2.

3.2 Objectives

An outline of the main objectives of this study are as follows:

1. Determine the effect of laser power on accuracy of PIV measurements taken with a mobile phone camera. Use results of testing to optimize the design of the mI-PIV app and system.

Table 3.1: mI-PIV parameters that were tested for their effect on total system error, as well as the equivalent parameters of the system they were benchmarked against. "(Ave. Displacement at 30 fps)" shown in the second line of the second row is the average displacement of the particles found by the lab-grade system corresponding to the flow velocities in the first line in second row.

Parameter	**mI-PIV Value**	**Benchmark Value**	**Benchmark**
Laser setting	1, 2, 3, 4, 5, 6, 7, 8, 9, 10, 15, 20, 25, 30, 35, 40, 45, 50 [mW]	36 [mJ/pulse] at 120 [Hz]	Lab-Grade System
Flow velocity (Ave. Displacement at 30 fps)	0.76, 1.16, 1.65, 2.07, 2.45, [cm/s] (4.8, 7.0, 10.2, 12.3, 15.0 [pix])		
Number of lasers	1, 2	1	
Optic lens type	Glass stir stick, Thorlabs optic lens	LaVision Optic Lens	
Type of illumination	CW laser, LED	Pulsed laser	
PIV programs	JPIV, OpenPIV, PIVlab, DaVis	True displacement data	Synthetic Images

2. Determine the effect of flow velocity on accuracy of the system. Use the results to optimize the design of the mI-PIV app and system.

3. Determine the viability of a double-laser (2x5 mW) design intended to increase particle illumination while keeping the mI-PIV system within the IIIa laser classification in order to eliminate the need for protective eyewear. This was done by comparing the double-laser design with a single laser pointer set at 10 mW.

4. Determine the viability of particle illumination using an LED pointer for planar PIV, when compared with a CW laser sheet.

5. Determine the performance of a glass stir stick as a sheet optic for producing a laser sheet for particle illumination, compared to the performance of a Thorlabs optic lens.

6. Compare performance of open-source PIV programs PIVlab, OpenPIV, and JPIV with DaVis (proprietary) using synthetic images.

3.3 Benchmarking Setup for Physical mI-PIV Components

A simple steady-state square duct flow was measured with the mI-PIV system and a lab-grade (LG) system on the same region of interest (ROI), as illustrated in fig. 3.1. This was achieved by aligning the LG and mI-PIV laser sheets to illuminate the same section of the flow and aiming both the LG and the mI-PIV camera at the same ROI. The LG system is shown in the top row of fig. 3.1 and the mI-PIV system is shown in the bottom row. The left column shows a front view of the setups and the right column shows a side view, which is a cross-section of the front view. A photograph of the setup is shown in fig. 3.2.

Mean bias error of the mI-PIV system was found in terms of the x-direction using eqs. (3.1) to (3.3), as defined by [40], where $(\Delta x)_{mI,i}$ is a single displacement measured by the mI-PIV system, $d_{m,x}$ is mean mI-PIV displacement, $(\Delta x)_{LG,i}$ is a single displacement measured by the lab-grade system, $d_{a,x}$ is mean LG displacement (considered the true displacement), and d_b is error. Root-mean-square (RMS) error σ_x [40] was found at each location in the ROI by eq. (3.4), using the $d_{m,x}$ and $(\Delta x)_{mI,i}$ that have already been defined. Since RMS error σ_x only serves to quantify the variation of the measurements around the mean, $d_{a,x}$ is not needed for its calculation. These equations can be used in terms of the y-direction as well.

$$d_{m,x} = \frac{1}{N}\sum_{i=1}^{N}(\Delta x)_{mI,i} \tag{3.1}$$

$$d_{a,x} = \frac{1}{N}\sum_{i=1}^{N}(\Delta x)_{LG,i} \tag{3.2}$$

$$d_{b,x} = d_{m,x} - d_{a,x} \tag{3.3}$$

$$\sigma_x = \sqrt{\frac{1}{N}\sum_{i=1}^{N}\left((\Delta x)_{mI,i} - d_{m,x}\right)^2} \tag{3.4}$$

The summations in eqs. (3.1), (3.2) and (3.4) are over the measurements given by all evaluated image pairs in the ensemble correlation. The number of image pairs is N. For

example, if 100 LG image pairs are evaluated, the mean LG displacement $d_{a,x}$ at point (1,1) of the output PIV measurement grid is

$$[d(1,1)]_{a,x} = \frac{1}{100} \sum_{i=1}^{100} [\Delta x(1,1)]_{LG,i}$$

where $\Delta x(1,1)$ represents a single measurements at point (1,1) of the output PIV measurement grid.

The average displacements in the x-direction $(d_{a,x})_{ave}$ were found for the entire ROI, as shown in eq. (3.5), where N_{meas} is the number of PIV measurements in the ROI. This is the source of the "Ave. Displacement" values shown in the second line in the second row of Table 3.1.

$$(d_{a,x})_{ave} = \frac{1}{N_{meas}} \sum_{i=1}^{N_{meas}} (d_{a,x})_i \tag{3.5}$$

The flow was produced with a flow visualization water tunnel designed by Engineering Laboratory Design Inc. with inner dimensions of 6x6 inches (15.24x15.24 cm). Its test section has four glass walls, all with a 532 nm wavelength anti-reflective coating.

For the mI-PIV system, a SparkFun Electronics 532 nm CW laser diode was used. The diode was bought on Amazon and had a laser driver already incorporated. It was rated at 5 mW at 5 V. For these tests, it was powered by a power source at 5 V and its output power was adjusted by input current. Output power of the laser was measured immediately before each test with a Thorlabs S121C photodiode power sensor coupled with a Thorlabs PM100USB Power and Energy Meter Interface, which was connected to a laptop. A 1/4-inch glass stir stick was used as an optic lens to spread the beam into a sheet, and a Google Pixel 3 XL smartphone camera was used for image acquisition. Brightness (aperture) of the Google Pixel 3 XL was set to maximum and shutter speed was not adjusted (left at default value, which is not known from phone metadata). This was due to the fact that these settings are difficult and/or impossible to adjust with the app on the Google Pixel 3 XL and may also be difficult and/or impossible to adjust with the app on different mobile phones that teachers or students may use, and therefore a widely usable system cannot depend on

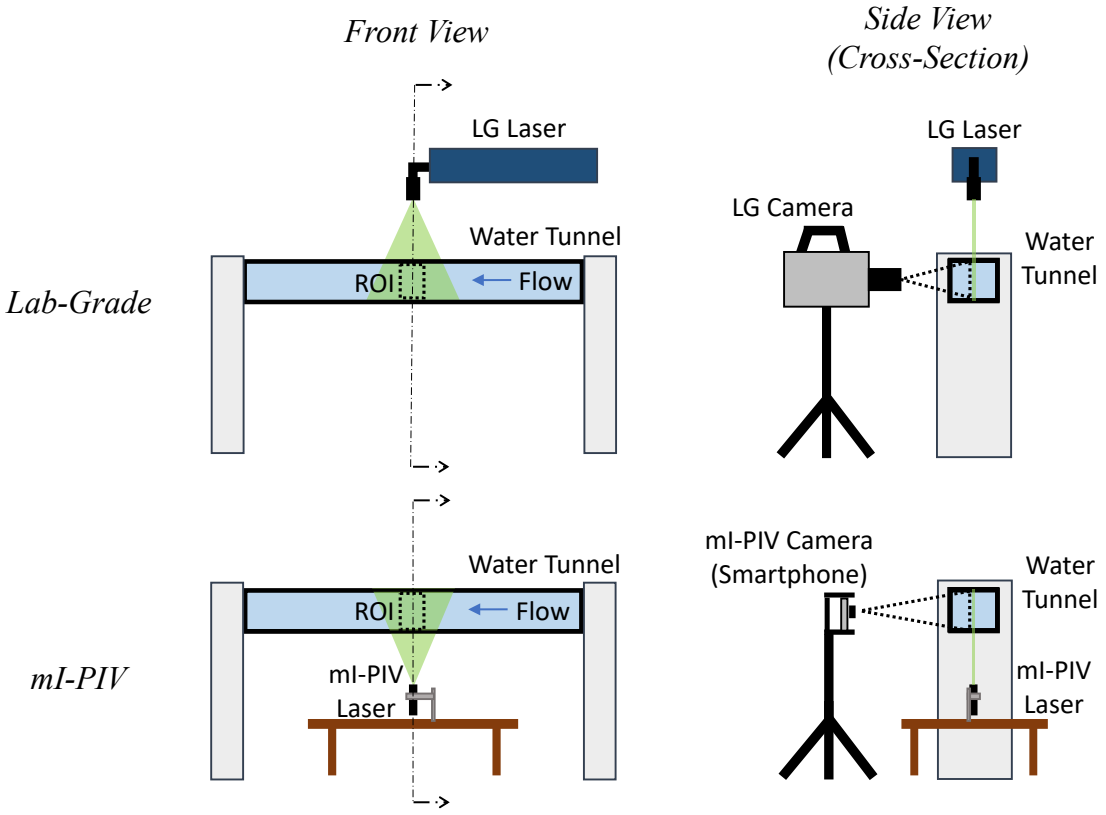

Fig. 3.1: Setup for benchmarking against a lab-grade (LG) system. ROI is measured by the lab-grade PIV system and the mI-PIV system and error is found using eq. (3.3). Note that the two systems measure the same ROI in the same plane, but not simultaneously.

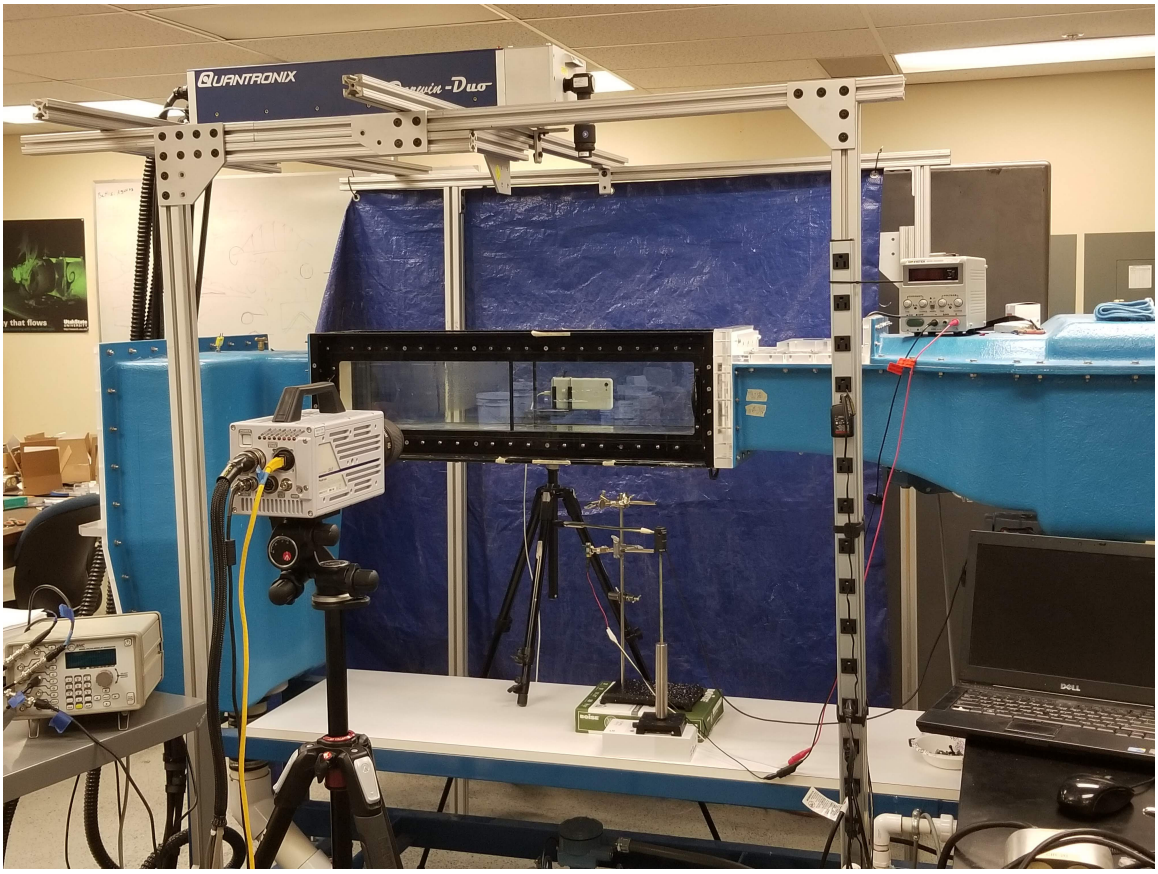

Fig. 3.2: Setup for benchmarking against a lab-grade (LG) system. ROI is measured by the lab-grade PIV system and the mI-PIV system and error is found using eq. (3.3). Note that the two systems measure the same ROI in the same plane, but not simultaneously.

adjustment of such parameters. Also, the frame rate was kept at 30 fps, because this is the standard frame rate of most currently available mobile phones, and because at this stage of the project the mobile application did not have the capability of changing frame rate of the camera. As a note, it still lacks this capability at the time of writing this work. A higher frame rate was not used because of the issue of very low particle illumination. Higher frame rates allow less light into the aperture, which then compounds the problem of particle images that already have very low brightness and low contrast from the background. The importance of proper lighting is discussed in greater detail in Section 3.4.1.

For the lab-grade system, a Quantronix Darwin-Duo diode-pumped solid state Nd:YLF 527 nm laser was set to a current of 18 [A] (36 [mJ/pulse]) and its beam was spread into a sheet by a LaVision sheet optics lens with a focal point of -10 mm. A FASTCAM SA3 camera was synced to the laser with a pulse generator for image acquisition. Since the Darwin-Duo laser does not have the capacity to pulse at rates under 100 Hz, the synced camera and laser were set to a frequency of 120 Hz and 3 frames were skipped to give an image pair with an equivalent frame rate of 30 fps, or $dt = 1/30$ [s]. A diagram illustrating this method of skipping frames is shown in fig. 3.3, where it can be seen that by skipping 1 frame between image pairs, a frame rate of 60 fps can be obtained, and by skipping 3 frames between image pairs, a frame rate of 30 fps can be obtained.

For the purpose of repeatability, further specifications of equipment used for this experiment are given in Appendix B.

PIV was performed using the FFT cross-correlation, sub-pixel accuracy, multipass algorithm contained in the `<piv_FFTmulti()>` function provided by PIVlab [2]. In particular, one pass was made with a 128x128 pixel interrogation area and a second and third pass was made with a 64x64 pixel interrogation area for the multipass scheme. The large size of the first interrogation area was chosen so that there would be more than 5 particles per interrogation area, as suggested in [14]. Since the flow was considered to be steady-state, PIV data was averaged across 150 image pairs for ensemble correlation to decrease the effect of variations in the flow from one time step to the next. Background

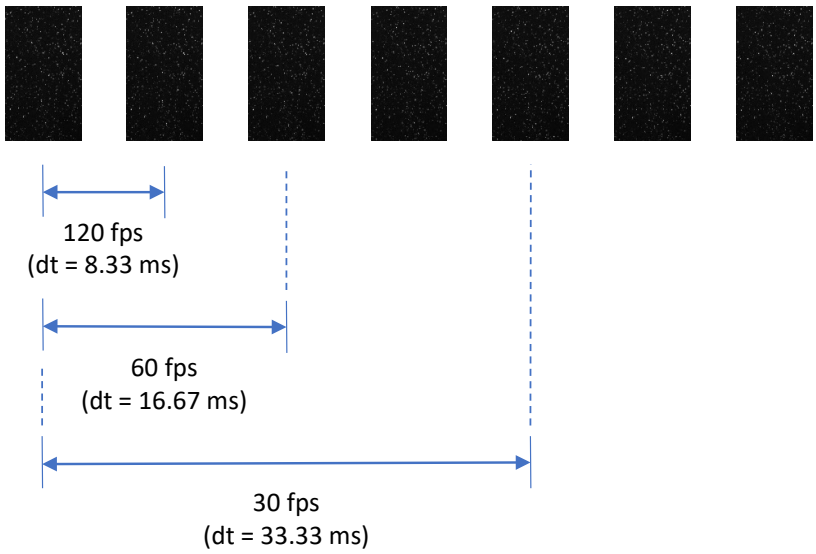

Fig. 3.3: Diagram illustrating the method used for obtaining a frame rate of 30 fps from a synced camera and laser pulsed at 120 Hz. By skipping 1 frame between image pairs, a frame rate of 60 fps can be obtained, and by skipping 3 frames between image pairs, a frame rate of 30 fps can be obtained.

subtraction was done for preprocessing on the lab-grade images, and mI-PIV images were evaluated with and without background subtraction preprocessing in order to determine its effect, as described in Section 3.4.3. For the lab-grade measurements, outliers were detected using a standard deviation filter and a local median filter, turned into NaNs, and then replaced using the spring metaphor interpolation technique included in MATLAB's `<inpaint_nans()>` function. The algorithm for validation and outlier removal/replacement is found in the `<PIVlab_commandline.m>` script provided with PIVlab. Outlier detection was used on the lab-grade measurements because these measurements were meant to represent the flow as closely as possible for a proper benchmarking. It is well-known that spurious vectors can cause unnecessary discrepancies in the true velocities of a flow and "mask data of good quality, possibly even leading to misinterpretation of the data" [10]. However, neither outlier detection nor replacement were applied to the mI-PIV measurements. This was so that only the raw data was analyzed for these measurements and thus the performance of the actual system could be more accurately evaluated.

3.4 Laser Output Power

3.4.1 Motivation

In PIV image acquisition, contrast of particles from the background of the image is absolutely essential, otherwise the correlation peak can be low compared to peaks produced from background noise and stationary objects [10, 15, 41, 42, 43]. From this it can be inferred that since higher laser power leads to greater particle illumination, it will also lead to increased PIV accuracy. In fact, M. Kiss [44] found that laser output power is indeed positively correlated with signal-to-noise ratio (SNR), as well as particles detected in the images, at least for their particular setup: laser powers from 0.3 W (300 mW) to 1.9 W (1900 mW), shutter speed at 1000 ms, and aperture at 2.0. Also of importance is maintaining the same level of brightness of a particular particle as it travels through the light sheet. Any variations in illumination throughout the light sheet can cause loss-of-correlation due to out-of-plane motion [45, 46, 47]. If a laser is weak and/or of low quality, particles may not be sufficiently bright enough to produce a strong correlation peak, or there may be undesired out-of-plane motion. It is therefore concluded that illumination is a critical factor in the design of the mI-PIV system.

There are two very important factors of the mI-PIV system that limit the potential brightness of the laser in the mI-PIV design:

1. *Cost*: – The least expensive laser diodes and laser pointers that can be purchased online today (as far as the present authors have found) tend to range in output power from around 1 mW - 50 mW. Since a minimal-cost PIV system is desired, these low-cost, low-powered lasers are an appealing choice for particle illumination. As a matter of fact, most of the inexpensive PIV solutions mentioned in the introduction in Section 1.4 do use very low laser output powers (1 mW – 100 mW) compared to a lab-grade PIV system [18, 19, 20, 21, 22, 24, 25]. Although many of these papers have accuracy assessments, the assessments are generally only taken using one laser output power. Therefore, at these low laser powers, the effect of varying illumination

on PIV accuracy remains mostly unstudied. In effect, it is unknown whether it is better to use a 50 mW laser or a 5 mW laser for PIV with a low-cost, non- lab grade system. We seek to answer such a question. This knowledge can then serve to assist other researchers as they consider the effects of laser output power in a low-power PIV measurement.

2. *Safety*: – For a PIV system that can be used in high schools or other youth settings, safety takes paramount importance. It follows that laser output power should be as low as possible in such a system. One of the major objectives of the mI-PIV system is to keep laser output power at or under 5 mW in order to remove the need to provide protective eyewear to mI-PIV users, as stated in Sections 1.3.4 and 2.3. This objective conflicts with the objective of obtaining maximum possible accuracy by increasing illumination.

For a low-power laser PIV system, laser output power and error are hypothesized to have a correlation similar to the plot shown in fig. 3.4. The reasoning behind this hypothetical plot is that at a laser power of zero, error must be at a maximum, since with zero output power there can be no laser sheet to illuminate the particles and thus no correlation. Then error should decrease with increasing illumination until a threshold is hit where the particle images reach a maximum possible brightness. After this point, error is no longer correlated with illumination and is either random or associated with other factors in the PIV system.

3.4.2 Methods

The mI-PIV laser was set to different output powers from 2 mW to 50 mW, with sample images shown in fig. 3.5, and output measurements were benchmarked as described in Section 3.3. As power increases in fig. 3.5, so does the brightness of the particles, as expected, but from about 10 mW and up, background noise also increases. This is especially noticeable at the lines produced from the reflection of the laser on the top and bottom glass sheets of the flow channel.

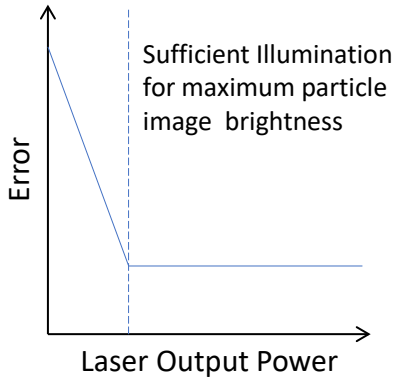

Fig. 3.4: Hypothetical relationship between error and laser output power at very low laser output powers. Error is hypothesized to be maximum at zero laser output power because there would be no illumination, then to decrease with increasing illumination until a threshold is hit where the particle images reach a maximum possible brightness. After this point, error is no longer correlated with illumination and is either random or associated with other factors in the PIV system.

This range of output power was used because it is the range of output power of several different laser pointers that were purchased online and then tested with a photodiode power sensor. Those lasers tested represent a sample of lasers that may be purchased by a teacher and used in conjunction with the mI-PIV system. Also, it was desired to test lasers in both the IIIa and IIIb classification, either of which is potentially applicable to the project. Originally the low end of the range was 1 mW, but that laser output power was not able to illuminate any particles sufficiently for the mobile phone camera to detect them and so no correlation could be found for the images. Because of this, the 1 mW images were removed from the dataset.

3.4.3 Results

In order to quantitatively determine the accuracy of the mI-PIV system throughout the ROI, colormaps were made for mI-PIV and LG mean displacements in the x-direction d_x, as given by eq. (3.6) and are shown in fig. 3.6. Equation (3.6) is similar to eqs. (3.1) and (3.2), but generalized to encompass measurements from either system. These displacements are given for output powers from 2-50 mW and are from a 2.45 cm/s flow, which corresponds to

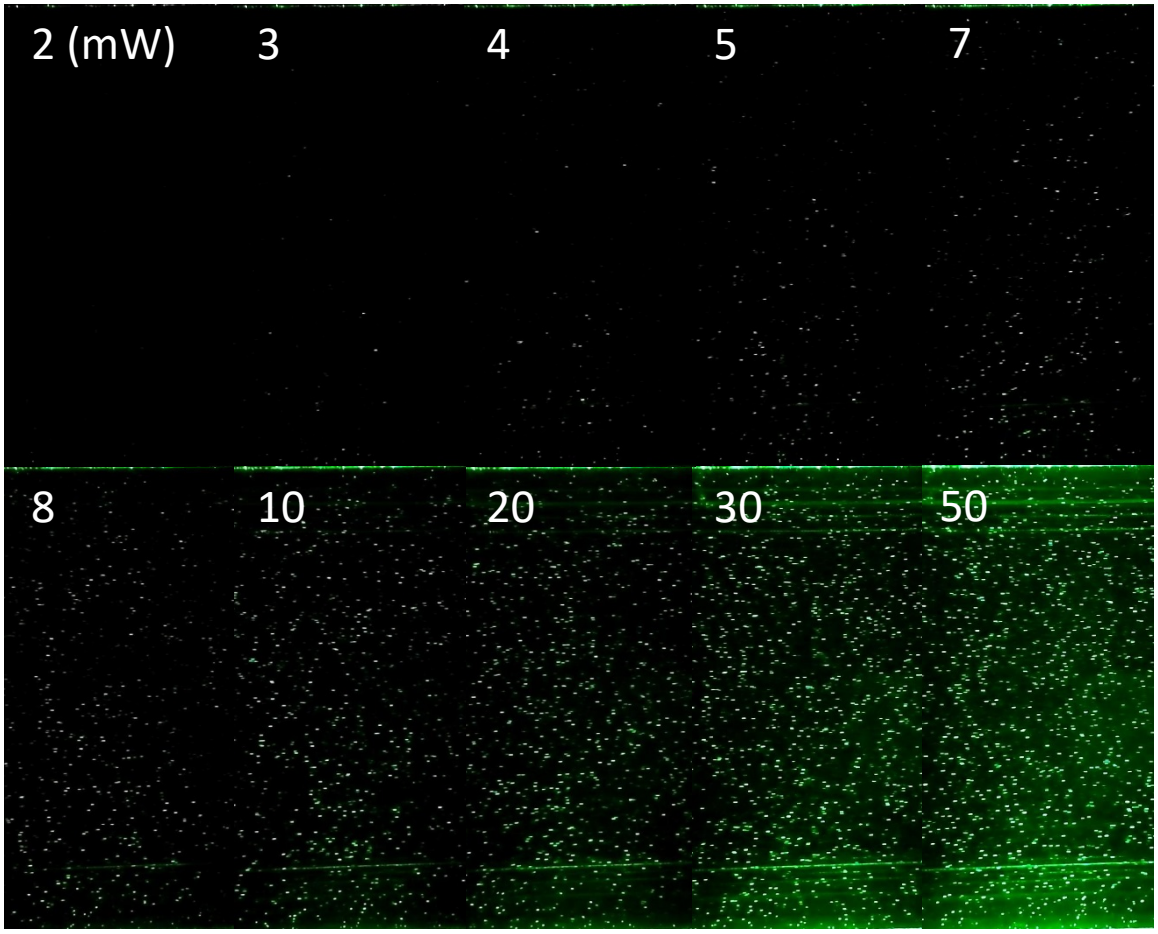

Fig. 3.5: mI-PIV crops with varying mI-PIV laser output powers. No background subtraction was applied to these images, in contrast to the images in fig. 3.12, where background subtraction has been applied.

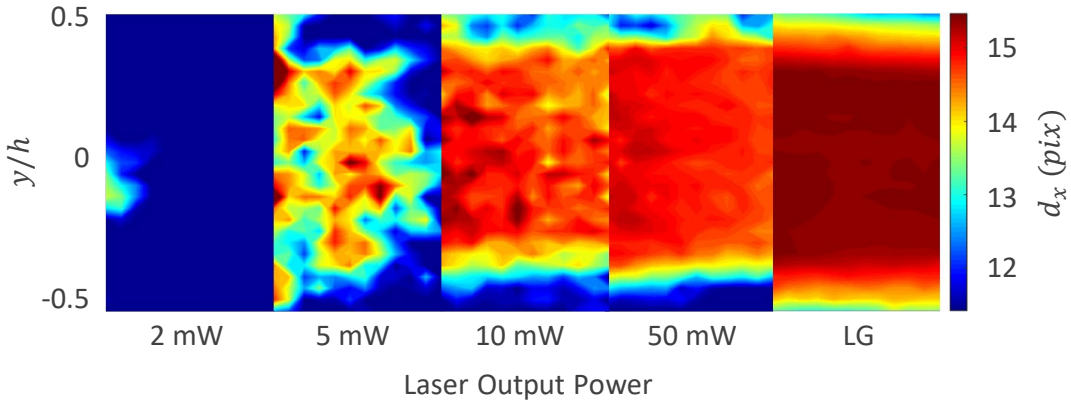

Fig. 3.6: Colormaps showing mean pixel displacement in the x-direction d_x for measurements with mI-PIV system set at laser powers from 2 mW to 50 mW, as well as for lab-grade (LG) system and the double-laser (2x5) tests. This case shows measurements for $(d_{a,x})_{ave} = 15.0$ [pix]

$(d_{a,x})_{ave} = 15.0$ [pix] (as given by eq. (3.5) and specified in table 3.1). Figure 3.6 shows that the higher the laser power for the mI-PIV system, the more similar the flow measurement looks to the lab-grade measurement of the flow.

$$d_x = \frac{1}{N}\sum_{i=1}^{N}(\Delta x)_i \tag{3.6}$$

The flow in this setup is was assumed to be unidirectional in the x-direction. Therefore the analysis is primarily concerned with displacement, bias error, and RMS error in the x-direction. However, for the sake of thoroughness, a y-direction analysis is given in Section 3.4.3.1. Also, plots that illustrate total magnitude of bias and RMS errors, which are calculated from the displacement vectors that include both the x- and y-directions, are given in Appendix C.

The values d_x, $d_{b,x}$ and σ_x were found with eqs. (3.3), (3.4) and (3.6) for the entire ROI and then each value was averaged across the x-axis (column-wise) to obtain column-wise-averaged displacement in the x-direction d_x^*, column-wise-averaged mean bias error in the x-direction, and $d_{b,x}^*$ and column-wise-averaged RMS error in the x-direction σ_x^*, as given in eqs. (3.7) to (3.9).

$$d_x^* = \frac{1}{N_{col}} \sum_{i=1}^{N_{col}} (d_x)_i \tag{3.7}$$

$$d_{b,x}^* = \frac{1}{N_{col}} \sum_{i=1}^{N_{col}} (d_{b,x})_i \tag{3.8}$$

$$\sigma_x^* = \frac{1}{N_{col}} \sum_{i=1}^{N_{col}} (\sigma_x)_i \tag{3.9}$$

Figure 3.7 shows the profile plots created with d_x^* and σ_x^*. There are five subplots for the five different $(d_{a,x})_{ave}$ that were measured. Each color corresponds to a different laser output power of the mI-PIV system and the black lines represent the LG measurements. The solid lines represent d_x^* and the dotted lines represent σ_x^*. For all the subplots, the 2 mW cases (blue solid lines) give displacement measurements near zero, due to the extremely low illumination and weak correlation. At 5 mW (pink solid lines), the measurements are consistently better than at 2 mW, but still largely underestimate the flow compared to the higher-laser-power measurements and the lab-grade measurement. In general, the higher the laser power, the closer the measurements come to the lab-grade measurement throughout the ROI, especially in the main body of the flow. RMS error σ_x^* for the 2 mW and 5 mW cases (blue and pink dotted lines) are very high, generally over 8 [pix]. However, 10 mW and 50 mW (green and red dotted lines) generally give RMS error that is substantially lower than in the lower-power cases, and is especially low at lower $(d_{a,x})_{ave}$. LG (black) RMS error is consistently low for all cases. Decreasing RMS with increasing laser output power is thought to be due to increasing correlation signals with increasing laser output power.

Column-wise-averaged mean bias error $d_{b,x}^*$ is shown in the profile plots in fig. 3.8. Again, each subplot corresponds to a different $(d_{a,x})_{ave}$ and color represents laser output power of the mI-PIV system. There is no lab-grade $d_{b,x}$, since $d_{b,x}$ is defined from the lab-grade measurements (see eq. (3.3)). Positive bias error for mI-PIV measurements means that displacement is overestimated and negative bias error means that displacement is underestimated. It is readily seen that the mI-PIV measurements almost always underestimate

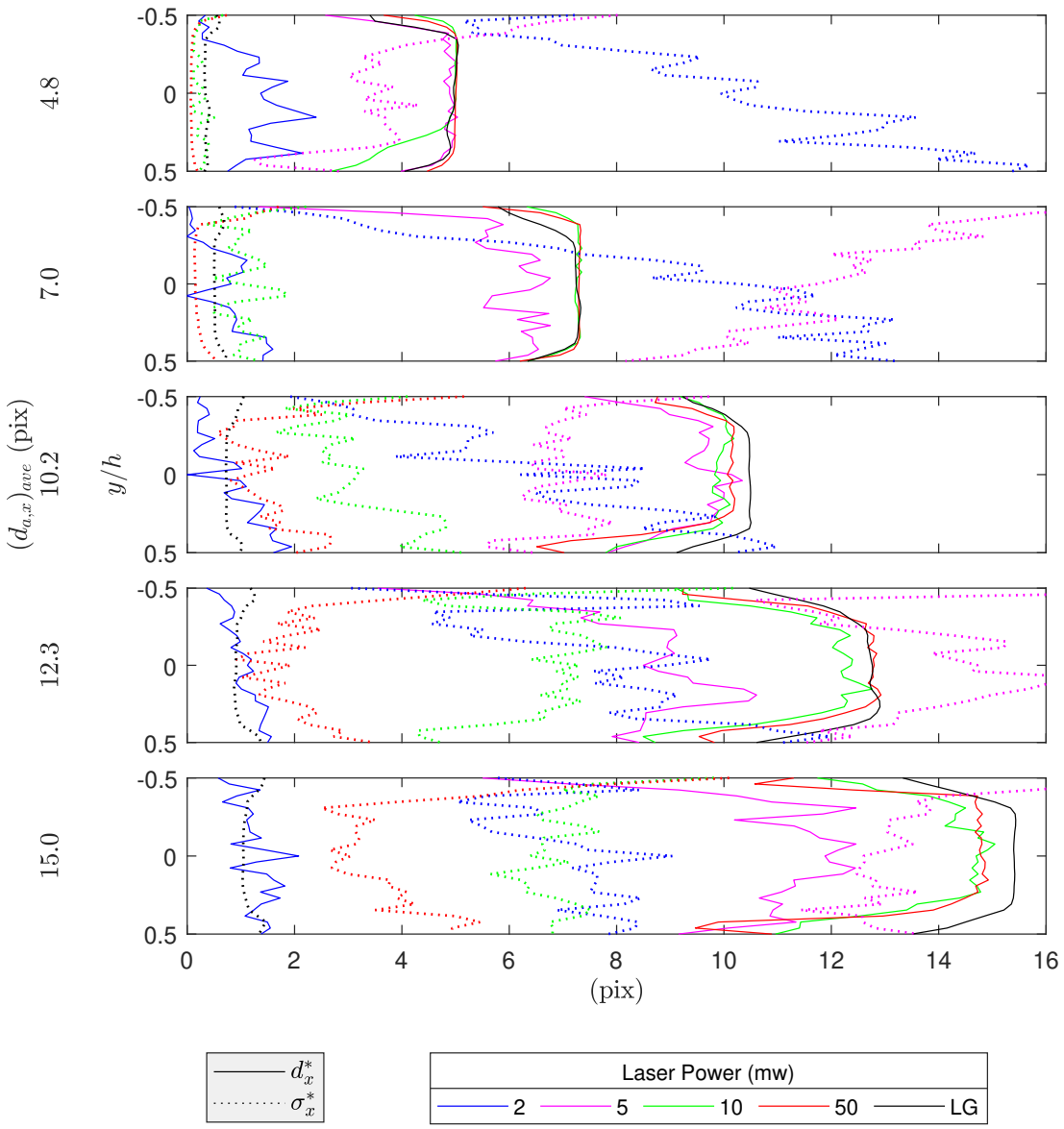

Fig. 3.7: Profile plots showing d_x^* and σ_x^* for different mI-PIV laser output powers (colors) and the LG measurement (black) at different $(d_{a,x})_{ave}$ (subplots). The left-most legend shows that d_x^* is represented by solid lines and σ_x^* is represented by dotted lines.

the flow, since most $d^*_{b,x}$ in the plots in fig. 3.8 are negative. This underestimation is likely caused mostly by the lower contrast of the particles in the mI-PIV images than in the LG images. Lower contrast weakens the correlation signal and thus gives a smaller displacement estimation. Such a supposition is supported by the fact that as output laser power decreases, $d_{b,x}$ becomes more negative, showing more underestimation with lower levels of illumination. Absolute bias error in the x-direction $|d^*_{b,x}|$ (distance of $d^*_{b,x}$ from zero) can be useful to analyze the magnitude of the bias error. The main trend in fig. 3.8 is that with increasing laser power, there is decreasing $|d^*_{b,x}|$. Laser output power of 2 mW gives very high $|d^*_{b,x}|$ throughout most of the ROI for all $(d_{a,x})_{ave}$, since it was already shown that d^*_x is close to zero in all cases. At 5 mW, $|d^*_{b,x}|$ is lower than at 2 mW but is still not very good, except where $(d_{a,x})_{ave} = 4.8$ [pix], in which case it is near zero. At output laser powers of 10 mW and 50 mW, bias error is mostly fairly small in the middle of the flow but higher at the edges of the flow. This is likely due to error in PIV measurements,as well as the random fluctuations of the actual flow, since even the LG flows are seen to have slightly different shapes at the edges of the ROI from one flow velocity to the next (see fig. 3.7 for displacement profiles). Likely, $|d^*_{b,x}|$ is lower in the main body of the flow than at the edges because this is the part of the flow with the least velocity gradients and because it is the most steady part of the flow and allows for more precise measurements.

In order to better visualize the *overall* effect of laser power on accuracy, the magnitudes of the mean bias errors in the x-direction $|d_{b,x}|$ were averaged across the entire ROI for all experiments, giving an overall average magnitude of the bias error $|d_{b,x}|_{ave}$ for the ROI, as shown in eq. (3.10), where N_{meas} represents the total number of measurements in the ROI. Overall average RMS error in the x-direction $(\sigma_x)_{ave}$ was also found using eq. (3.11), where again, N_{meas} is the number of measurements in the ROI. It was not necessary to calculate absolute values of RMS errors, because RMS error is never negative (due to the square in eq. (3.4)).

$$|d_{b,x}|_{ave} = \frac{1}{N_{meas}} \sum_{i=1}^{N_{meas}} |d_{b,x}|_i \tag{3.10}$$

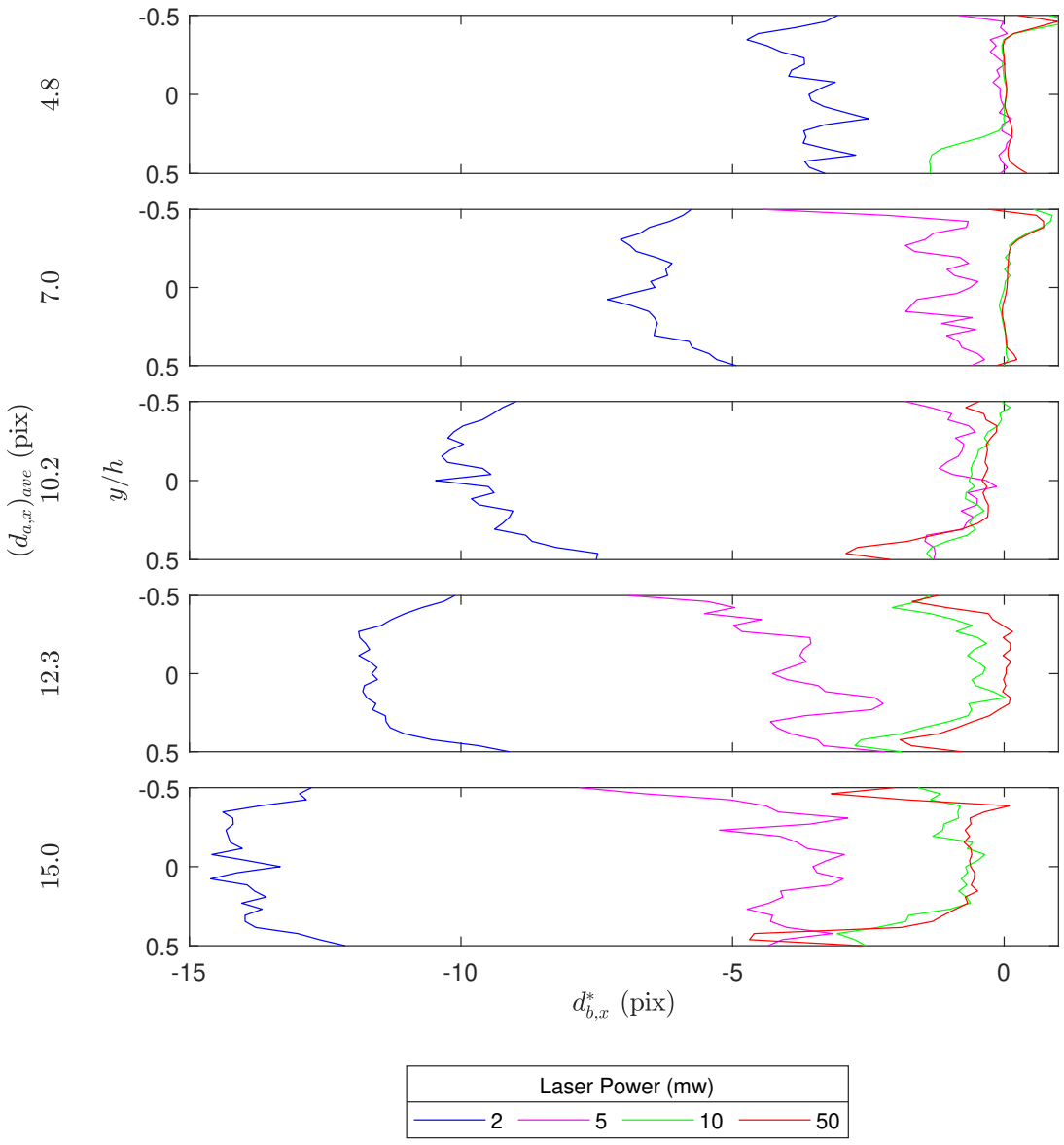

Fig. 3.8: Profile plots showing $d^*_{b,x}$ for different mI-PIV laser output powers (colors) at different $(d_{a,x})_{ave}$ (subplots). There is no lab-grade $d_{b,x}$, since $d_{b,x}$ is defined from the lab-grade measurements (see eq. (3.3)).

$$(\sigma_x)_{ave} = \frac{1}{N_{meas}} \sum_{i=1}^{N_{meas}} (\sigma_x)_i \tag{3.11}$$

For each case of different laser output powers and $(d_{a,x})_{ave}$ that was tested, $|d_{b,x}|_{ave}$ was found and is represented by a point in fig. 3.9, and $(\sigma_x)_{ave}$ was found and for each test, represented by a point in fig. 3.10. In both plots, the x-axis represents laser output power, $|d_{b,x}|_{ave}$ is shown on the y-axis and different $(d_{a,x})_{ave}$ are given as colors in the rightmost legend, while the symbols in the middle legend represent the type of test performed. Tests with a single stir stick and single laser pointer *without* background subtraction applied to the mI-PIV images ("Single Stir Stick, No Background Sub" in the legend) are shown as dots. Tests with a single stir stick and single laser pointer *with* background subtraction on the mI-PIV images ("Single Stir Stick, Background Sub" in the legend) are shown as circles. Tests with the double-laser system ("Double Laser" in the legend), discussed further in Section 3.6, are shown as the crosses at the 10 mW tick mark. Tests with a Thorlabs optics lens ("Thorlabs Optic Lens" in the legend), discussed further in Section 3.7, are shown as stars at the 5 and 10 mW tick marks. The solid trend lines were calculated from the "Single Stir Stick, No Background Sub" tests (dots), using MATLAB's two-term exponential fit, and the dashed trend lines were calculated from the "Single Stir Stick, Background Sub" test (circles), also using a two-term exponential fit. These fits are chosen by observation of the data and the goodness of fit (as evaluated by R^2 values), not by a known mathematically proven theoretical trend.

The plot in fig. 3.9 shows a trend that is very similar to the hypothesized trend shown in fig. 3.4, except that the sharp corner in fig. 3.4 is rounded in fig. 3.9. Like expected in the hypothetical plot, there is indeed a strong decrease in bias error for increasing laser power at low laser powers, and then error flattens out for higher laser powers. This shows a kind of minimum error achievable by the system in terms of laser power, which will be defined here as "Laser output power cutoff for approximate minimum bias error" Φ^*_{bias}. These Φ^*_{bias} values are from visual estimation of where the trend line begins to flatten out. For example, it is obvious that the $(d_{a,x})_{ave} = 7.0$ [pix] trend (black line) in fig. 3.9 has

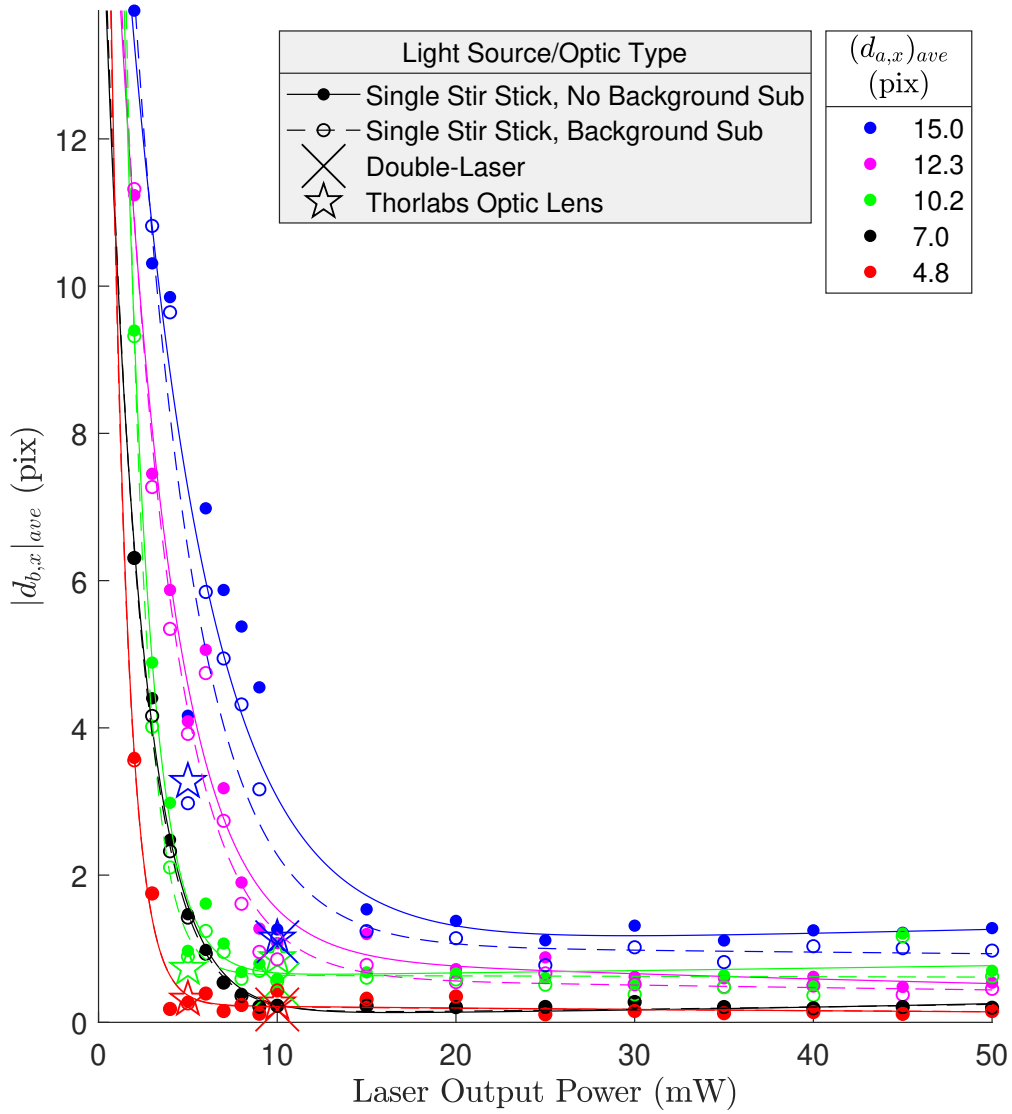

Fig. 3.9: Overall average magnitude of mean bias error in the x-direction $|d_{b,x}|_{ave}$ as a function of laser output power for the mI-PIV system. Colors represent overall average displacement $(d_{a,x})_{ave}$ in [pix]. Dots represent single stir stick analysis with no background subtraction applied to the mI-PIV images, and solid lines are two-term exponential fits of those data (for $(d_{a,x})_{ave}$ from top to bottom of legend, $R^2 = 0.92,\ 0.97,\ 0.99,\ 0.99,\ 0.96$). Circles represent single stir stick analysis with background subtraction applied to the mI-PIV images, and dashed lines are two-term exponential fits of those data (for $(d_{a,x})_{ave}$ from top to bottom of legend, $R^2 = 0.93,\ 0.97,\ 0.99,\ 0.99,\ 0.96$). Crosses at 10 mW represent error from the double-laser tests (no background subtraction for the mI-PIV images), and stars at 5 and 10 mW represent PIV error from the Thorlabs optic lens tests (no background subtraction for the mI-PIV images).

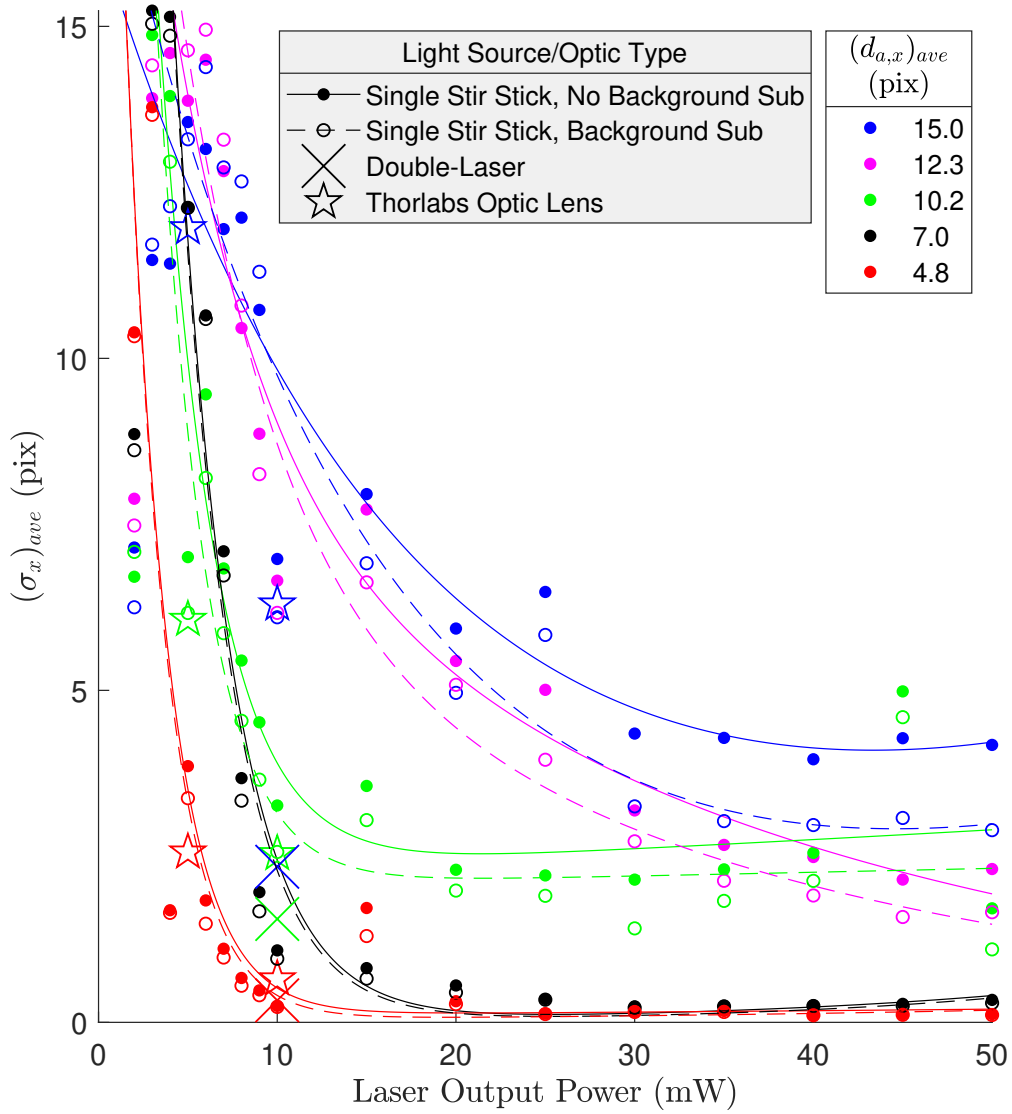

Fig. 3.10: Overall average RMS error in the x-direction $(\sigma_x)_{ave}$ as a function of laser output power for the mI-PIV system. Colors represent overall average displacement $(d_{a,x})_{ave}$ in [pix]. Dots represent single stir stick analysis with no background subtraction applied to the mI-PIV images, and solid lines are two-term exponential fits of those data (for $(d_{a,x})_{ave}$ from top to bottom of legend, $R^2 = 0.91,\ 0.95,\ 0.87,\ 0.97,\ 0.78$). Circles represent single stir stick analysis with background subtraction applied to the mI-PIV images, and dashed lines are two-term exponential fits of those data (for $(d_{a,x})_{ave}$ from top to bottom of legend, $R^2 = 0.90,\ 0.96,\ 0.86,\ 0.96,\ 0.79$). Crosses at 10 mW represent error from the double-laser tests (no background subtraction for the mI-PIV images), and stars at 5 and 10 mW represent PIV error from the Thorlabs optic lens tests (no background subtraction for the mI-PIV images).

almost entirely flattened out around 8 mW, so $\Phi^*_{bias} = 8$ [mW] is chosen for $(d_{a,x})_{ave} = 7.0$ [pix]. The fits in fig. 3.9 follow the data closely, as shown by the R^2 values given in the caption, so these trend lines, and thus Φ^*_{bias}, are thought to be reasonably representative of the data. However, these estimations, like the data fits, are not based on a known proven mathematical model but can nevertheless serve as useful interpretations of the data. The point where error begins to flatten is different for each LG average x-displacement $(d_{a,x})_{ave}$ (colors), and for these data Φ^*_{bias} ranges from 4 mW for $(d_{a,x})_{ave} = 4.8$ [pix] (red line in fig. 3.9) to 15 mW for $(d_{a,x})_{ave} = 15.0$ [pix] (blue line in fig. 3.9).

The plot in fig. 3.10 shows a similar relationship between laser output power and RMS error to that of mean bias error in fig. 3.9, except that RMS error is much slower to drop with increasing laser power. RMS error is especially sensitive to the negative effect of low laser output power, showing RMS error values of up to 15 pixels for laser output powers below 7 mW.

"Laser output power cutoff for approximate minimum RMS error" Φ^*_{RMS} is estimated for the trends in fig. 3.10, in similar fashion to how Φ^*_{bias} was estimated for bias error. Both Φ^*_{bias} and Φ^*_{RMS} are estimated for all $(d_{a,x})_{ave}$ that were tested and shown in fig. 3.11. The Φ^*_{bias} are taken from the plots in fig. 3.9 and the Φ^*_{RMS} are taken from the plots in fig. 3.10. The trend lines In fig. 3.11 are linear fits evaluated with the `<fit()>` function in MATLAB.

Figure 3.11 demonstrates that as $(d_{a,x})_{ave}$ increases, so do both Φ^*_{bias} and Φ^*_{RMS}. In other words, as flow velocity increases (which means an increase in $(d_{a,x})_{ave}$ for a camera at a fixed frame rate), a higher laser output power is required to reach a minimum possible bias error Φ^*_{bias}, and a higher laser output power is required to reach a minimum possible RMS error Φ^*_{RMS} as well. As has been stated already, RMS is more sensitive to laser output power, at least in these data, which is the reason for the larger slope in Φ^*_{RMS} (red trend line). It is thought that this trend can be forecasted to higher $(d_{a,x})_{ave}$ due to the clarity of the relationship shown.

Due to the especially large bias and RMS errors below 7 mW, shown in figs. 3.9 and 3.10,

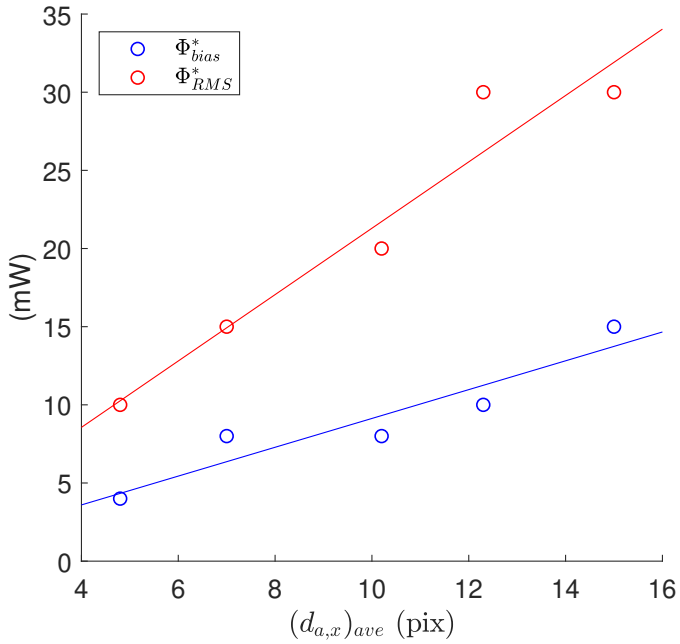

Fig. 3.11: Laser output powers at which an approximate minimum possible error for the system is reached, at least in terms of laser output power, for given $(d_{a,x})_{ave}$. "Laser output power cutoffs for approximate minimum bias error" Φ^*_{bias} are the points at which the different lines in fig. 3.9 begin to flatten out, while "Laser output power cutoffs for approximate minimum RMS error" Φ^*_{RMS} are the points at which the different lines in fig. 3.10 begin to flatten out. Blue points and fits are for Φ^*_{bias} and red points and fits are for Φ^*_{RMS}. The fit for Φ^*_{bias} gives $R^2 = 0.88$ and the fit for Φ^*_{RMS} gives $R^2 = 0.93$.

this range of output power is considered to be unacceptable for the mI-PIV system. For laser output powers above 10 mW, most mean bias errors fall under 2 pixel for the flow rates that were measured. This is quite good for such a low-grade system and is considered acceptable for the mI-PIV system design. Such a pattern suggests the use of the double-laser system introduced in Section 2.3, which is meant to increase power of the laser sheet to 10 mW using two 5 mW lasers, and who's performance is analyzed in Section 3.6.3. The fact that RMS error is higher than mean bias error suggests that ensemble correlation is a useful tool for mI-PIV that should be explored, since this technique serves to reduce the effects of random error on the final output measurement [10].

It was initially thought that the flattening out of bias and RMS errors previously discussed could possibly be due in part to the increase in noise at higher laser output powers, seen in the images in fig. 3.5. As was stated in Section 3.4.2, the particles in the images from 2 mW to 10 mW get brighter with increasing power but the background stays basically black. In the images from 10 mW to 50 mW, the particles still seem to get slightly brighter with increasing laser power, but the background also get brighter, until at 50 mW there is a very pronounced green tint throughout the entire image, as well as bright lines where the laser sheet crosses the glass sheets of the flow channel. Such an increase in background noise and stationary objects (the green lines) of course decreases the contrast of the image, in turn lowering the correct correlation signal and increasing surrounding correlation signals. This is a well-known occurrence [10, 15, 41, 42, 43] that has been discussed in Section 3.4.1. Could it be that this decrease of correlation signal due to noise at laser powers form 10-50 mW is cancelling the increase of correlation signal due to particle brightness to contribute to the flattening of error at higher laser output powers?

The PIV analysis was run on all images again, but background subtraction was applied to the mI-PIV images by averaging 30 images (out of 300) for each analysis that were temporally distant from each other and subtracting that "average image" from all images in the ensemble. The background-subtracted images are shown in fig. 3.12, and it is readily apparent that most background noise has been removed when compared with fig. 3.5. Bias

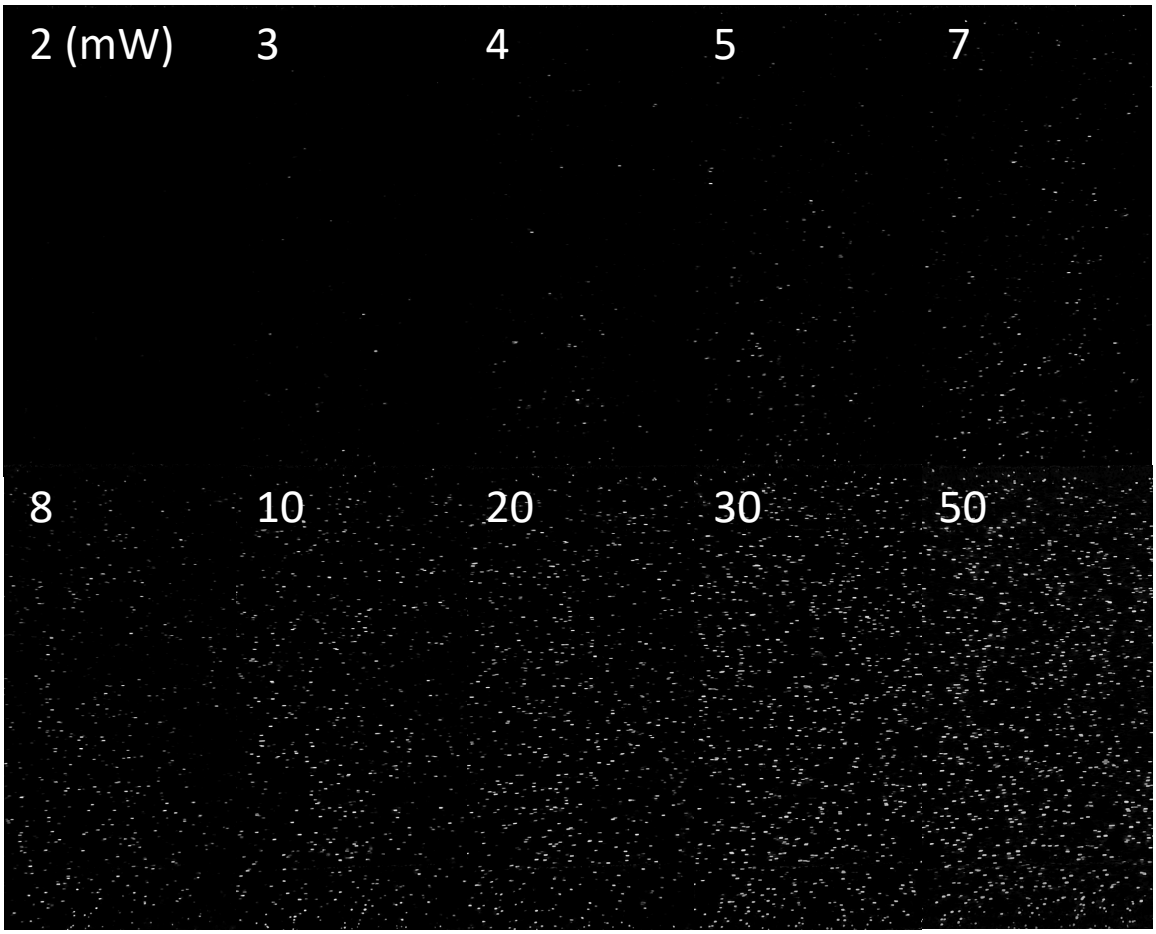

Fig. 3.12: mI-PIV crops with background subtraction applied at varying mI-PIV laser output powers. These are the same images as in fig. 3.5 but with background subtraction applied.

error and RMS error calculated from these results, shown as the circles with the dashed trend lines in figs. 3.9 and 3.10, suggests that background noise is not a large factor in the overall average error obtained, because these data are almost identical to the data made from the non-background subtraction PIV analyses. It seems that there is hardly any real improvement in accuracy from background subtraction in this case. This lack of substantial improvement from background subtraction is probably due to the fact that other factors, such as saturation of particle brightness and low correlation signal due to the low illumination, play more heavily into the bias and RMS errors of the mI-PIV system than the background noise and effect of stationary objects.

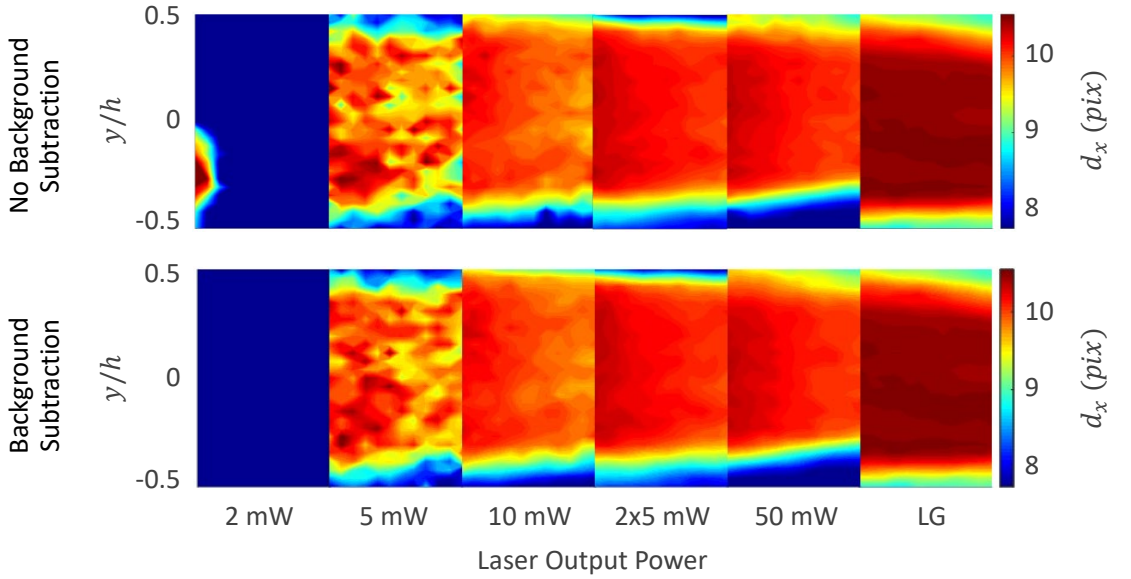

Fig. 3.13: Comparison of colormaps from PIV with no background subtraction (*top*) to colormaps of PIV with background subtraction (*bottom*) applied. Only very subtle differences are present, except in the 2 mW colormaps, in which velocity in the far left of the ROI is lower for the background subtraction case than for the non-background subtracted case. This may be because the few particles that were in the 2 mW images (see the 2 mW image in fig. 3.5) were basically completely erased from the background subtraction (see the 2 mW image in fig. 3.12). The LG colormaps are identical because background subtraction was applied to the LG images in all cases. The $(d_{a,x})_{ave} = 10.2$ [pix] for both cases.

The colormaps that result from the images with background subtraction are also extremely similar to the colormaps resulting from no background subtraction, as shown in fig. 3.13, where the top row is evaluated from images with no background subtraction and the bottom row is evaluated with images with background subtraction applied. Since all other background subtraction colormaps were nearly identical to their no-background-subtraction counterparts, only this sample is shown here to demonstrate the similarity. Note that the LG colormaps are identical because background subtraction was applied to the lab-grade images in all cases.

3.4.3.1 Y-Direction Analysis

Although the flow was considered to be unidirectional in the x-direction, the average displacement in the y-direction d_y, bias error in the y-direction $d_{b,y}$, and RMS error in

the y-direction σ_y were evaluated in case additional information could be obtained for the present analysis. From these values, d_y^*, $d_{b,y}^*$ and σ_y^* were obtained by replacing x with y in eqs. (3.7) to (3.9), and are shown in figs. 3.14 and 3.15. It can be seen by comparing the displacements in fig. 3.14 to the bias errors in fig. 3.15 that $d_{b,y}^*$ is generally of the same magnitude as d_y^* and both are very much smaller than $d_{b,x}^*$ and d_x^* (shown in figs. 3.7 and 3.8. This suggests that bias error in the y-direction $d_{b,y}^*$ is almost entirely random. The flow is much more steady in the x-direction, which validates the assumption of a unidirectional flow for this study. RMS error in the y-direction σ_y^*, shown in fig. 3.14 is seen to be very similar to σ_x, shown in fig. 3.7. This further suggests that the error in the y-direction is dominated by random error.

The overall average mean bias error in the y-direction $(d_{b,y})_{ave}$ was plotted in fig. 3.16, and the overall average RMS error $(\sigma_y)_{ave}$ was plotted in fig. 3.17. It can be seen from fig. 3.16 that $(d_{b,y})_{ave}$ is almost completely independent of laser output power, except that at very low laser powers it fluctuates at greater magnitudes. This confirms that error in the y-direction is mostly completely random experimental error. The $(\sigma_y)_{ave}$ shown in fig. 3.17 is nearly identical to the $(\sigma_y)_{ave}$ shown in fig. 3.10. This again confirms that y-displacement is mostly random.

3.5 Flow Velocity

3.5.1 Motivation

The flow field can affect PIV accuracy in a variety of ways. In-plane velocity gradients can increase random error at the location of the gradients [10, 16], and if there is much of an out-of-plane velocity gradient it will cause out-of-plane motion and thus increase error [42]. Also, particle streaking can affect accuracy. Particle streaking is caused by movement of particles that is either significantly faster than the laser pulse in pulsed-laser PIV or significantly faster than the shutter speed in CW laser PIV [10, 48].

Velocity of the flow is hypothesized to have a significant effect on PIV accuracy for the mI-PIV system, since a CW laser is used, and also because frame rate and shutter speed

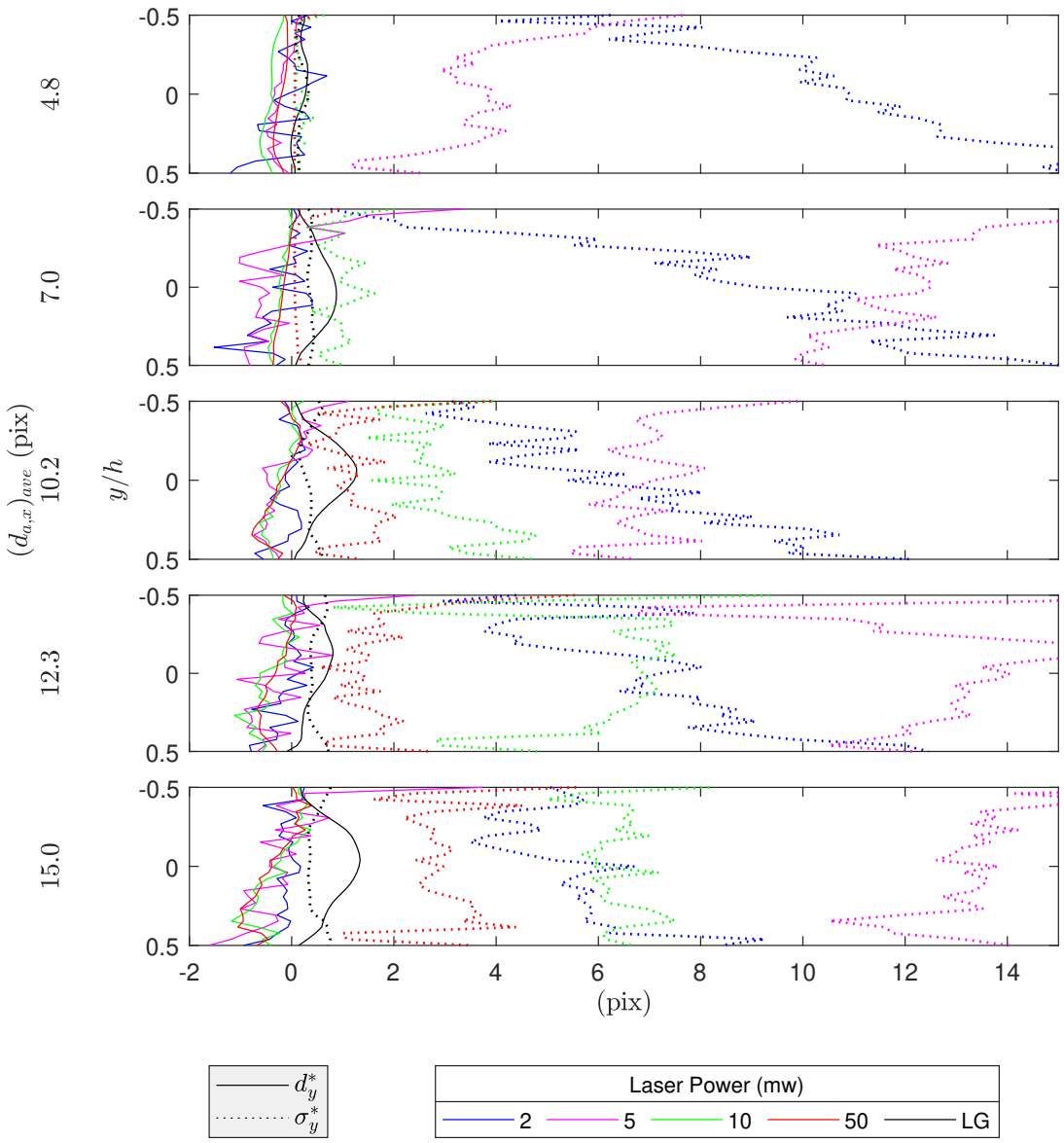

Fig. 3.14: Profile plots showing d_y^* and σ_y^* for different mI-PIV laser output powers (colors) and the LG measurement (black) at different $(d_{a,x})_{ave}$ (subplots). The left-most legend shows that d_y^* is represented by solid lines and σ_y^* is represented by dotted lines.

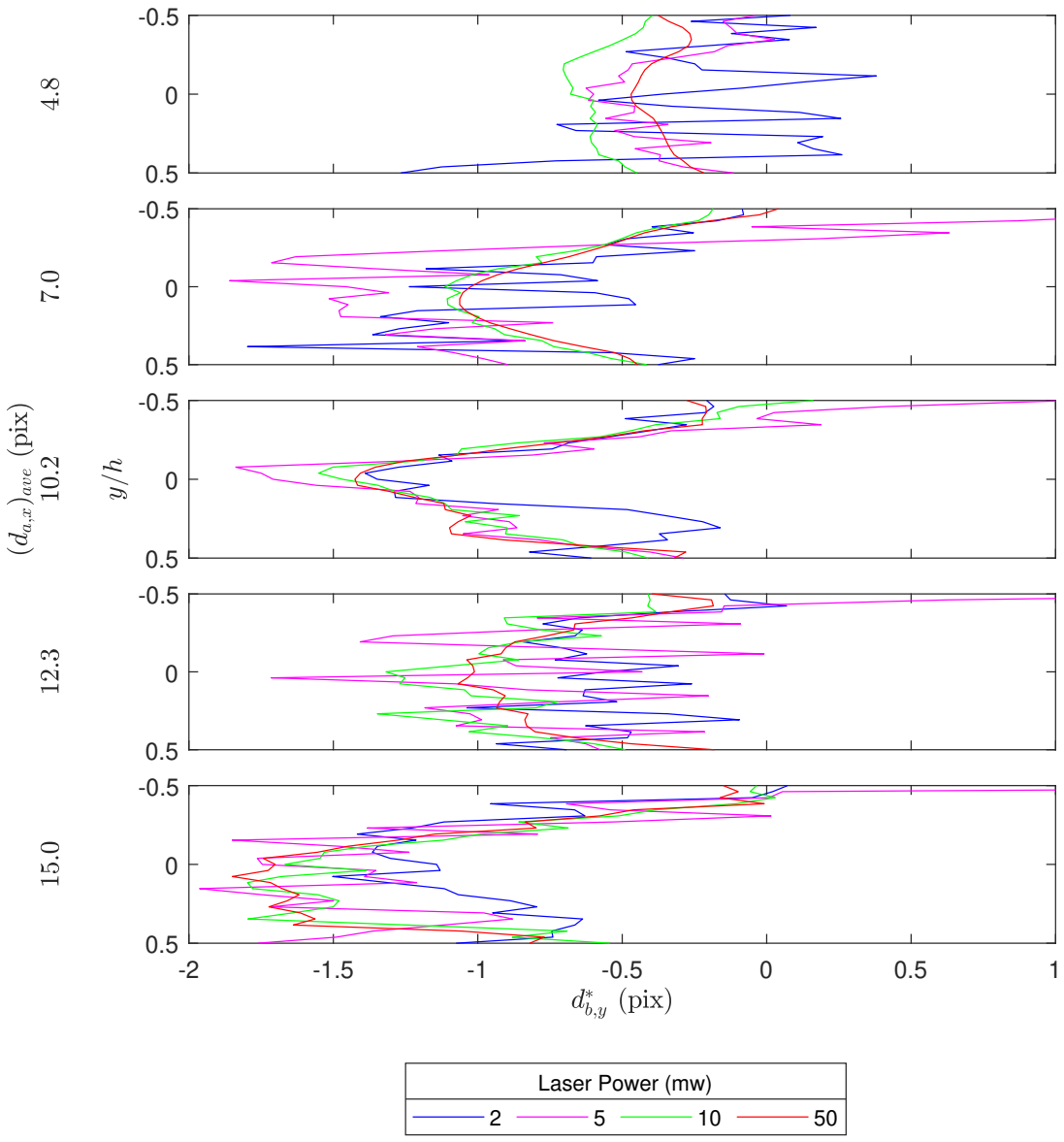

Fig. 3.15: Profile plots showing $d^*_{b,y}$ for different mI-PIV laser output powers (colors) at different $(d_{a,x})_{ave}$ (subplots). There is no lab-grade $d_{b,y}$, since $d_{b,y}$ is defined from the lab-grade measurements (see eq. (3.3)).

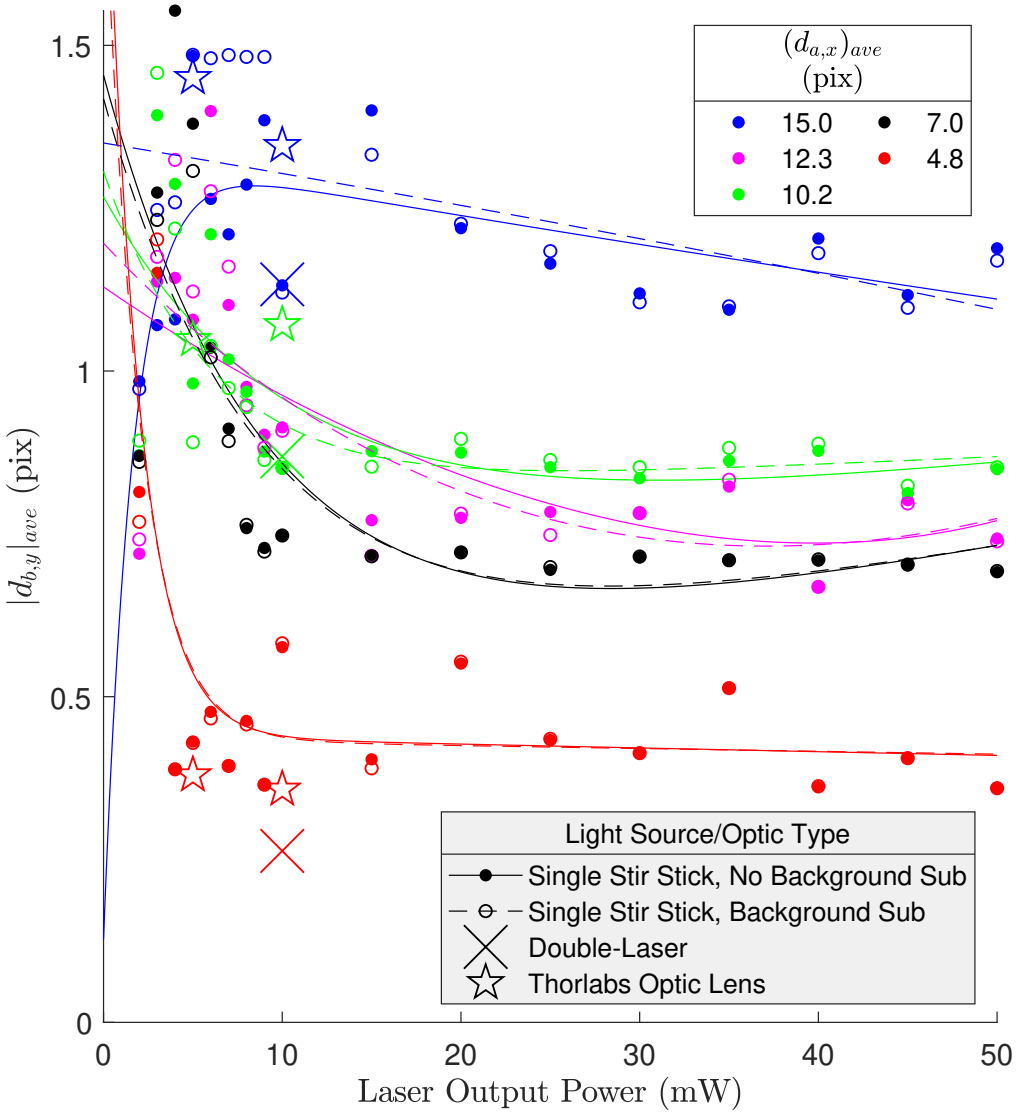

Fig. 3.16: Overall average of the magnitude of mean bias error in the y-direction $|d_{b,y}|_{ave}$ as a function of laser output power for the mI-PIV system. Colors represent overall average displacement $(d_{a,x})_{ave}$ in [pix]. Dots represent single stir stick analysis with no background subtraction applied to the mI-PIV images, and solid lines are two-term exponential fits of those data (for $(d_{a,x})_{ave}$ from top to bottom of legend, $R^2 = 0.44,\ 0.45,\ 0.47,\ 0.56,\ 0.52$). Circles represent single stir stick analysis with background subtraction applied to the mI-PIV images, and dashed lines are two-term exponential fits of those data (for $(d_{a,x})_{ave}$ from top to bottom of legend, $R^2 = 0.23,\ 0.50,\ 0.41,\ 0.55,\ 0.46$). Crosses at 10 mW represent error from the double-laser tests (no background subtraction for the mI-PIV images), and stars at 5 and 10 mW represent PIV error from the Thorlabs optic lens tests (no background subtraction for the mI-PIV images).

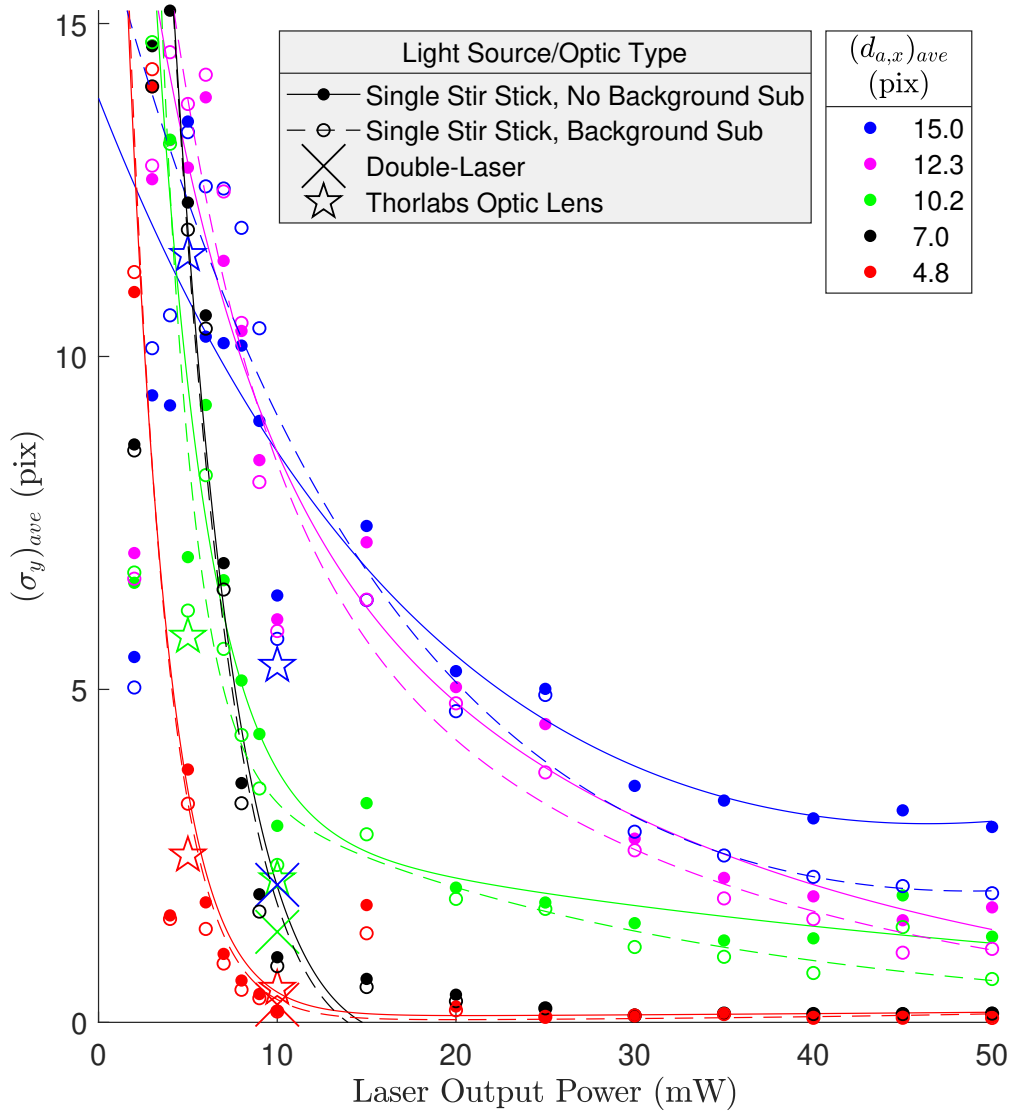

Fig. 3.17: Overall average of RMS error in the y-direction $(\sigma_y)_{ave}$ as a function of laser output power for the mI-PIV system. Colors represent overall average displacement $(d_{a,x})_{ave}$ in [pix]. Dots represent single stir stick analysis with no background subtraction applied to the mI-PIV images, and solid lines are two-term exponential fits of those data (for $(d_{a,x})_{ave}$ from top to bottom of legend, $R^2 = 0.90,\ 0.95,\ 0.93,\ 0.97,\ 0.79$). Circles represent single stir stick analysis with background subtraction applied to the mI-PIV images, and dashed lines are two-term exponential fits of those data (for $(d_{a,x})_{ave}$ from top to bottom of legend, $R^2 = 0.90,\ 0.96,\ 0.93,\ 0.98,\ 0.80$). Crosses at 10 mW represent error from the double-laser tests (no background subtraction for the mI-PIV images), and stars at 5 and 10 mW represent PIV error from the Thorlabs optic lens tests (no background subtraction for the mI-PIV images).

are held constant. A lab-grade PIV system is much less sensitive to high flow velocity, since pulsed lasers can allow for almost instantaneous capture of the moving particles and frame rate can be adjusted according to flow velocity. Again, frame rate and shutter speed are held constant at this stage of the project because the mobile application does not currently have the capability of changing those parameters on the mobile phone's built-in camera. For the above reasons, flow velocity's affect on accuracy is important for knowing what kinds of experiments mI-PIV is capable of analyzing effectively, and for designing experiments that are compatible with mI-PIV.

It is hypothesized that flow velocity and error have a positive correlation, as shown in the plot in fig. 3.18. This relationship is hypothesized because at higher flow velocities, there will be more particle-streaking, since shutter speed cannot be adjusted, and there will be greater in-plane loss of pairs from particles moving out of the interrogation window. Also, if the flow is not perfectly straight, there will be greater out-of-plane loss-of-pairs at higher velocities due to greater overall particle motion. All of these factors would cause an increase in error, as shown *before the dashed line* in fig. 3.18. At a certain velocity threshold, particle displacement will reach 1/2 of the width of the interrogation window, which will cause a complete loss of correlation and very high error, as shown *after the dashed line*. At this point, the PIV correlation basically gives random outputs, so error is at a maximum value and is no longer affected by velocity.

3.5.2 Methods

Flow velocity was varied in the channel by adjusting the motor speed of the pump. Flow velocity was adjusted from approximately 0.76 [cm/s] to 2.45 [cm/s] by (approximately) 0.4 [cm/s] intervals. Neither the flow velocities nor the intervals are exact due to the somewhat coarse adjustment capabilities of the flow channel. However, the exact flow rate is not extremely important, since only knowledge of a trend is desired. The flow velocities were calculated from the flow rate reading given by the channel and the known cross-sectional area of the channel. Again, these flow velocities each gave an average displacement $(d_{a,x})_{ave}$ as defined in eq. (3.5). The images in fig. 3.19 show some measurements at a laser power

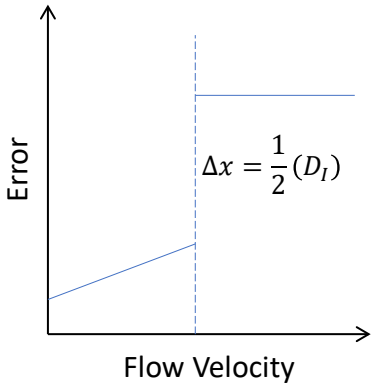

Fig. 3.18: Hypothetical relationship between error and flow velocity with fixed aperture, shutter speed, and frame rate due to use of mobile phone for image acquisition. Higher velocities are expected to cause increase in error, and once a particle displacement Δx of $1/2$ the width D_I of the interrogation window is reached, the error will have a large jump in magnitude, since there will then be a complete loss of correlation, at least when using an FFT correlation method.

of 50 mW for the range of velocities studied. The particles at higher velocities are very streaked compared to those at lower velocities. In fact, most of the particles at the higher velocities appear to be substantially longer in the direction of the flow than they are wide.

3.5.3 Results

It is seen in fig. 3.7 that as flow velocity, or $(d_{a,x})_{ave}$, increases, the correlation breaks down at 2 mW and 5 mW, resulting in a representation of the flow that is clearly incorrect. For example, in the 5 mW, $(d_{a,x})_{ave} = 15.0$ [pix] case, the flow is shown to be very weak and not smooth. At the same laser power, the $(d_{a,x})_{ave} = 4.8$ [pix] case gives a much better and smoother representation of the true flow as given by the LG measurement. Also, although the 10 mW readings give a good estimate of the flow at all flow velocities, there is much less smoothness in the $(d_{a,x})_{ave} = 15.0$ [pix] case than at $(d_{a,x})_{ave} = 4.8$ [pix] and $(d_{a,x})_{ave} = 7.0$ [pix]. This pattern is reiterated by the RMS error profile plots, shown as the dotted lines in fig. 3.7, where it can be seen that for any given laser power, σ_x increases rapidly with increasing $(d_{a,x})_{ave}$. Another notable pattern is that in the 50 mW cases, the edges of the flow seem to give greater RMS error than the middle of the flow does, which is likely caused

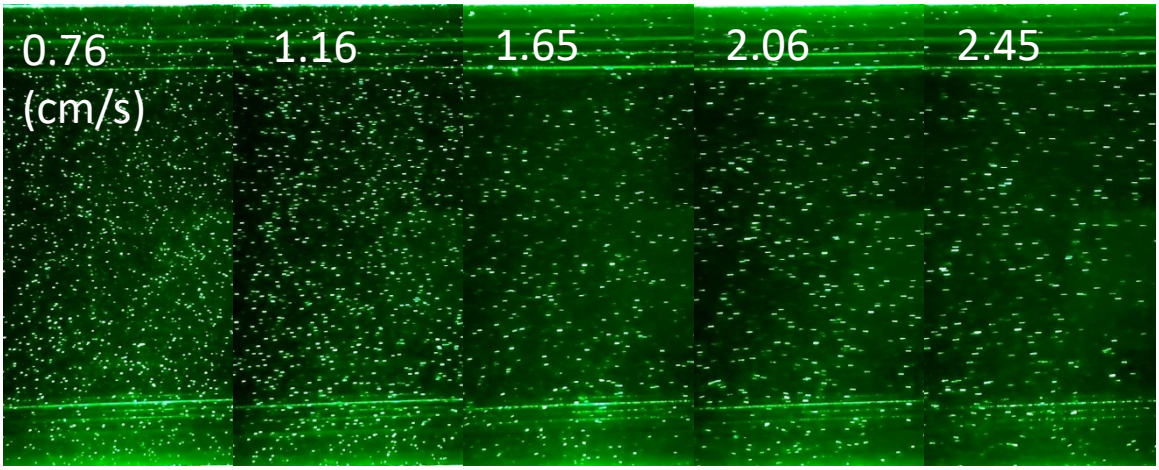

Fig. 3.19: Demonstration of amount of streaking of particles in mI-PIV crops at different velocities (all at 50 mW output power). As velocity increases (going left to right in the figure), particle image streaking is also shown to increase.

by the in-plane gradients present there [10, 16].

Mean bias error increases with flow velocity, as shown in fig. 3.14, although this trend is more pronounced at lower laser powers (see the 5 mW case at different cases of $(d_{a,x})_{ave}$) when compared to higher laser output powers (see the 50 mW case at different cases of $(d_{a,x})_{ave}$). Thus, high flow velocities and low laser output powers seem to compound each others' negative effects on PIV accuracy.

Upon viewing $|d_{b,x}|_{ave}$ and $(\sigma_x)_{ave}$ shown in figs. 3.9 and 3.10, it is clear that increasing flow velocity (and thus increasing $(d_{a,x})_{ave}$) consistently causes increasing bias error and RMS error, no matter the laser output power. This is the same pattern predicted in the hypothetical relationship in fig. 3.18 before the dashed line. It can also be seen that the effect of $(d_{a,x})_{ave}$ on bias error and RMS error is minimized at higher laser powers, whereas at lower laser powers, $(d_{a,x})_{ave}$ has a greater effect. For example, the trend lines in fig. 3.9 have a greater vertical spread from 5 to 15 mW than they do at ranges above 15 mW. Also, the lines in fig. 3.10 have a greater vertical spread from 5 to 30 mW than above 30 mW. Therefore, to a large extent, higher laser power mitigates the negative effect of flow velocity on accuracy.

It is thought that increases in mean bias and RMS errors with higher $(d_{a,x})_{ave}$ (seen

in figs. 3.9 and 3.10) are mostly due to the streaking of the particles. This is due to the fact that even the highest $(d_{a,x})_{ave}$ (15 pixels) is less than 1/4 of the interrogation window size D_I of the interrogation area in the first pass (128 pixels). Therefore, displacement itself does not have a strong effect on error at these low velocity flows. The flow is also slow enough that out-of-plane motion is not an issue, especially since it is a unidirectional flow. Therefore, most error at these low displacements are most likely caused by particle streaking.

What is not shown in these results is the effect of having displacements over 1/2 the size of the first interrogation window, since the maximum displacements of these tests ranged from about 5 pixels to 16 pixels. With an initial interrogation window size of 128 pixels, half of which is 64 pixels, this limit was never reached in these tests. However, it is well-known that once displacements reach 1/2 the size of the interrogation window, the FFT correlation method fails and results in completely inaccurate PIV measurements, so proving that assumption was never the goal of these tests.

3.6 Double Laser System

3.6.1 Motivation

In [23], the use of multiple lasers to increase overall illumination was shown to be effective. The "double-laser" system, shown in fig. 3.20, is an idea for the mI-PIV system that uses two 5 mW lasers — which are class IIIa and eliminate the need for safety eyewear — to output a 10 mW laser sheet, as described in Section 2.3. This idea is especially relevant to the mI-PIV system since it was seen in Section 3.4.3 that 10-15 mW gives minimum bias error for the system. It was hypothesized that if two 5 mW lasers are combined to form a single light sheet, that the resulting light sheet should be equivalent to a 10 mW sheet. If this proves to be true, then this double-laser (2x5 mW) combination should give PIV accuracy close to that given by a single 10 mW laser.

3.6.2 Methods

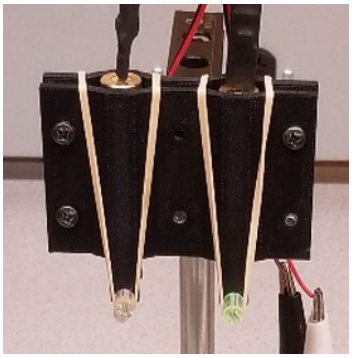

Fig. 3.20: Photo of the double-laser system, as described in Section 2.3. The rubber bands hold the glass stir sticks onto the frame.

In order to validate the hypothesis stated above, the double-laser system was used to perform PIV using the benchmarking setup, and the overall average magnitude of the bias error in the x-direction $|d_{b,x}|_{ave}$ was compared to that obtained when using a single 10 mW laser. Overall average RMS error in the x-direction $(\sigma_x)_{ave}$ was also compared for the two systems. This test determined whether the double-laser system could be considered a viable option to replace a single 10 mW laser system.

3.6.3 Results

The double-laser $|d_{b,x}|_{ave}$ for the $(d_{a,x})_{ave} = 15.0$, 10.2, and 4.8 [pix] flows are shown by the blue, green, and red crosses, respectively, all located above the 10 mW mark in fig. 3.9. The $|d_{b,x}|_{ave}$ for these double-laser tests are shown to be very close to the $|d_{b,x}|_{ave}$ for the single 10 mW laser tests and significantly lower than for the single 5 mW tests, represented by the blue, green, and red dots at 10 mW and 5 mW. Also, the $(\sigma_x)_{ave}$ given by the double-laser is consistently at or near the $(\sigma_x)_{ave}$ given by the single 10 mW laser, and significantly lower than the $(\sigma_x)_{ave}$ given by the single 5 mW laser, as shown in fig. 3.10. Thus it is verified that the double-laser system effectively combines the laser sheets of two 5 mW lasers — which are considered class IIIa and are safe enough to not require protective eyewear — to produce a laser sheet similar to one produced by a single 10 mW laser, which gives about 1/2 the error of a 5 mW laser sheet and close to the minimum error that can be achieved with the mI-PIV physical components.

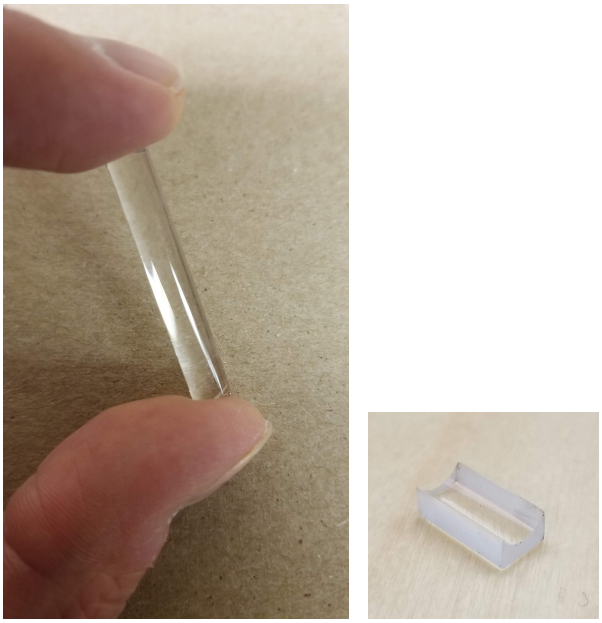

(a) (b)

Fig. 3.21: (a) Stir stick (b) Thorlabs optic lens

3.7 Laser Sheet Optic Lens Type

3.7.1 Motivation

It was found that a stir stick can be used to spread a laser beam into a sheet, with the round curvature of the stir stick bending the laser light in similar fashion to a traditional optic lens. Since a glass stir stick (fig. 3.21(a)) is much less expensive (on the order of $1.00) than an optic lens (fig. 3.21(b), on the order of $100.00), it is desired to know whether the stir stick optic solution is comparable to a traditional optic lens from an accuracy standpoint.

3.7.2 Methods

Testing was done using both a stir stick and a Thorlabs optic lens and $|d_{b,x}|_{ave}$ and $(\sigma_x)_{ave}$ were found for both types, similarly to the double-laser tests in Section 3.6. The same laser was used for both the stir stick optic lens tests and the Thorlabs optics lens tests. The stir stick had a radius of 1/8 inch, so the plano-concave (a common lens type for PIV sheet optics) Thorlabs optic lens that was purchased had a radius of curvature of 1/8

inch. On visual inspection, the spread of the laser sheets that the two lenses produced was very similar.

3.7.3 Results

From the plots in figs. 3.9 and 3.10, it can be seen that the measurements taken with the Thorlabs optic lens, shown by blue, green and red stars, and with the stir stick, shown by the blue, green and red dots, gave very similar $|d_{b,x}|_{ave}$ and $(\sigma_x)_{ave}$ at their respective $(d_{a,x})_{ave}$, at laser output powers of both 5 mW and 10 mW. This suggests that the stir stick introduces no appreciable error to the measurements vs. the Thorlabs optics lens. Since the two lenses performed so similarly, a stir stick is recommended for use with the mI-PIV system, as well as any other low-laser-power PIV system.

3.8 LED Pointer vs. Laser Pointer

3.8.1 Motivation

LEDs are commonly used for PIV, but mainly for volume illumination [49, 50, 51, 52, 53] due to their poor ability to be collimated [10]. However, LED sheet illumination was thought to have the potential to benefit the design of mI-PIV by providing an alternate, perhaps safer, light source to lasers. Whereas there are many rules and guidelines for lasers and their use, as was discussed in Section 1.3, there is a sparsity of restrictions on LEDs. This is, perhaps, because an LED does not emit collimated light as does a laser and is therefore not considered as severe a safety hazard. This makes LED light an interesting consideration for particle illumination in a high-risk environment, such as a high school, where safety hazards should be kept to an absolute minimum. Therefore, due to the possibility of safer PIV, LED illumination was of interest to this study, and was attempted for planar PIV.

3.8.2 Methods

A 532 nm LED pointer purchased from U.S. LED Solutions was used for PIV to compare to the laser sheet produced with the SparkFun Electronics laser pointer. This LED

Fig. 3.22: Sample image taken with the smartphone camera demonstrating that the LED pointer does not illuminate the particles.

pointer was comprised of a bright green LED that was focused with an aspherical lens and emitted out of a slit or point diaphragm to produce a dot or line beam, depending on which diaphragm was used. Since the beam obtained with the dot diaphragm was so dim, the line beam was used for the test. The line was about 1 mm wide at the waist and so was thought to be similar enough to the laser sheet that it would illuminate the particles in a similar fashion. The LED pointer was placed above the flow field to illuminate its midsection. Its accuracy was to be found by comparison to lab-grade measurements, as with the other parameters tested. Upon visual inspection, the beam was very dim.

3.8.3 Results

Upon acquiring images with the LED pointer, it was seen that the particles were not illuminated enough to be detected by the mobile phone camera — the images were almost completely black, as shown in fig. 3.22. The LED pointer was therefore deemed unsuitable for mI-PIV. This outcome is probably due to the very small diaphragm used by the pointer, which lets out only a very small fraction of the total light produced by the LED. This diaphragm is necessary to produce a thin sheet, even though the aspherical lens included with the pointer helps to focus the light, because LED light is not collimated. If the dot diaphragm were to be used to produce a beam of light and that beam were spread into a sheet using an optic lens in the same way that the laser sheet is formed, there would be much less light emitted, and the resulting sheet would be even more dim.

Possible further exploration into LED illumination may reveal that with a better lens configuration and/or a combination of many LEDs, such as in the work of Chetelat *et al.* [53], better results may be achieved. However, Chetelat *et al.*'s work in 2002 [53] dealt with volumetric PIV, and in their work in LED illumination in 2001 [20], they stated that LEDs are better used for volumetric PIV measurements because they cannot be formed into a focused sheet like a laser can. This is supported by other literature as well [10], and was reiterated with our experiment.

3.9 Open-Source PIV Algorithms

3.9.1 Motivation

Open-source PIV algorithms have been widely used in recent years due to their increasingly sophisticated algorithms and, of course, their free access. Although advanced proprietary algorithms seem to outperform these open-source algorithms [30], many open-source packages presently available are equipped with advanced features such as multi-pass, multigrid, and window deformation and have been shown to give satisfactory results. PIVlab and OpenPIV are equipped with preprocessing, multi-pass, multigrid, and window deformation, along with other advanced features. They have been benchmarked for accuracy against synthetic images and shown relatively high accuracies [2, 45, 54], and have been used in various experiments [18, 22, 23, 24, 25, 45]. JPIV is equipped with a multi-pass, multigrid algorithm and has also been used for a number of fluid velocity measurement applications [55, 56]. As far as the authors are aware, the accuracy of PIVlab, OpenPIV, and JPIV, have not been compared with the accuracy of advanced proprietary software such as DaVis using synthetic images. It has been stated in Section 2.2 that the current prototype of mI-PIV uses OpenPIV's multipass algorithm for PIV measurements. Also, the source code of PIVlab and JPIV may be used to aid in the design of a JAVA-based, handwritten PIV algorithm to be used in the future for a PIV algorithm that operates completely on the mobile device. Therefore, the performance of OpenPIV, JPIV, and PIVlab are of special interest in the design process of the mI-PIV algorithm.

3.9.2 Methods

The open source PIV packages JPIV, OpenPIV, PIVlab, and DaVis were tested and compared using synthetic images created in MATLAB. The synthetic images were generated using modified code from an image generation program included in the PIVlab download, and the particle displacement data of those synthetic images was saved. The creation of these synthetic images is described in Appendix D. One image pair used for analysis was a plane Poiseuille flow and the other image pair was a clockwise pure rotational flow. PIV was run on the images using the four software packages and the bias error was found using eq. (3.12), where d_b is bias error, PIV measurements are represented by $(\Delta x)_{PIV}$ and the true displacement data is represented as $(\Delta x)_{true}$. Equation (3.12) is modified from eq. (3.3) to eliminate the need to average over image pairs, since only one image pair was used for this analysis. For all PIV programs, a multipass algorithm was used with a 64x64 pixel interrogation window for the first pass and a 32x32 pixel interrogation window for the second pass. No preprocessing or postprocessing was done for any of the programs, so that the analysis could focus on the basic algorithms, and because the synthetic images were not noisy and were idealized for PIV.

$$d_b = (\Delta x)_{PIV} - (\Delta x)_{true} \tag{3.12}$$

3.9.3 Results

3.9.3.1 Poiseuille Flow

In fig. 3.23, color maps are shown for the absolute displacement $|\Delta\vec{x}|$ (left column) and absolute bias error $|\vec{d_b}|$ (right column) of each program (rows) throughout the ROI. $|\Delta\vec{x}|$ is found by combining Δx and Δy as given in eq. (3.13), and $|\vec{d_b}|$ is found by substituting $|\Delta\vec{x}|$ for Δx in eq. (3.12).

$$|\Delta\vec{x}| = \sqrt{(\Delta x)^2 + (\Delta y)^2} \tag{3.13}$$

A correlation can be seen between the smoothness of the $|\Delta\vec{x}|$ color maps and the magnitude of the $|\vec{d_b}|$. That is, the true displacement color map is completely smooth, and the less smooth the displacement color maps for the different programs, the more bias error was introduced. Generally, bias error occurs at somewhat random concentrated points throughout the ROI. Therefore, it is thought to be random bias error in the PIV measurement given by the different programs. For JPIV, PIVlab, and DaVis, the middle of the flow generally had little or none of these random points of bias error. This may be caused by the lower gradient in the middle of the flow compared to at the outer edges. Perhaps the reason this is not the case for the OpenPIV bias error is that random errors caused by the algorithm were larger than the errors caused by the gradients, and so dominated the overall bias error. In the case of the DaVis analysis, the error caused by the gradients seems to dominate over random algorithmic errors, showing a much smoother transition from low to high error in the ROI without so many error hot spots.

Since the OpenPIV multipass algorithms performed so poorly, as shown in the top row ("OpenPIVmulti") of fig. 3.23, the image was analyzed again using OpenPIV's single pass algorithm. This gave much better results, as shown in the second to the top row of fig. 3.23 (OpenPIVsingle). This points to the actual multi-pass scheme, not the PIV algorithm, as the cause of the large errors throughout the ROI in the OpenPIVmulti case. Perhaps the window shifting algorithm implemented in the WiDIM function has an error that causes the location of the displacement measurements to be slightly skewed.

3.9.3.2 Pure Rotational Flow

The colormaps in fig. 3.24 have the same layout as those in fig. 3.23. Also, similar patterns can be noticed in these color maps to the Poiseuille color maps in fig. 3.23, such as increasing roughness in $|\Delta\vec{x}|$ resulting in increasing $|\vec{d_b}|$. Although the performance of each algorithm relative to the others is similar to in the Poiseuille flow analysis, more overall bias error is present for the pure rotational flow. This may be because the negative effect of curvature of streamlines in the pure rotational flow is stronger than the effect of the in-plane gradients in the Poiseuille flow. In the PIVlab and DaVis analyses, the bias error seems to

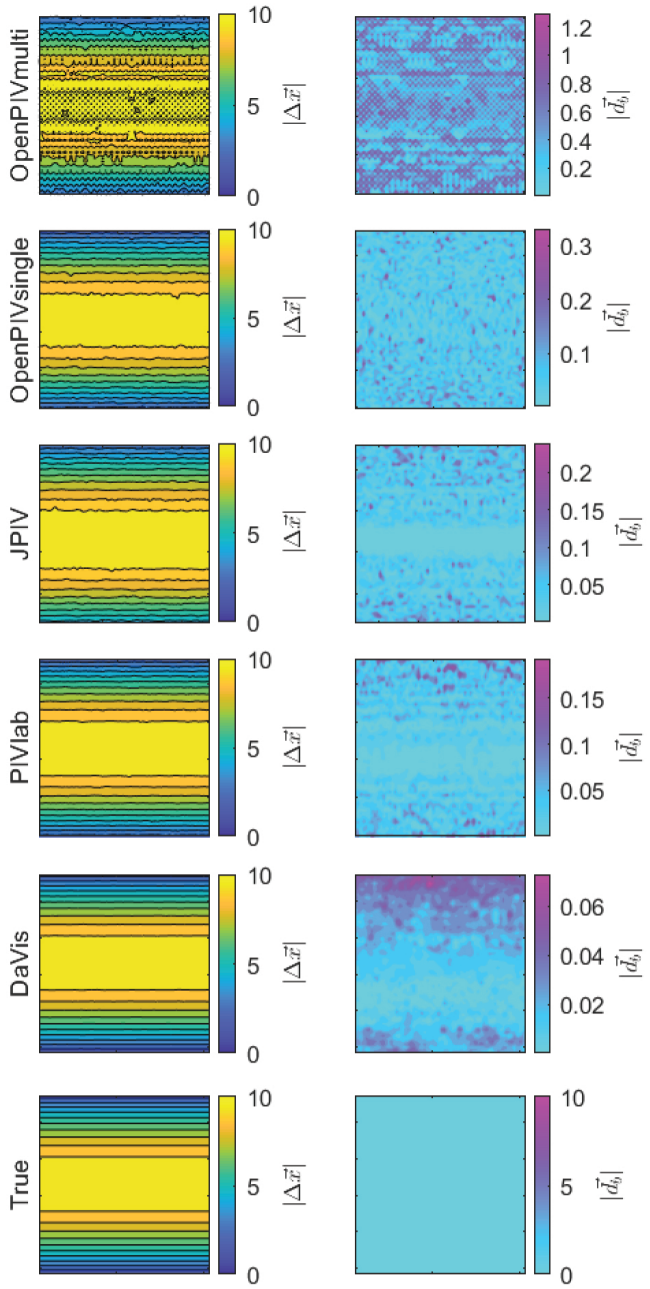

Fig. 3.23: OpenPIV, JPIV, PIVlab, and DaVis analyses of a synthetic Poiseuille flow. True displacement data is shown in the bottom left figure. Absolute displacement for each analysis is shown in the left column and magnitude of the bias error $|\vec{d_b}|$, as given in eq. (3.12), is shown in the right column for each analysis.

be strongly related to radial distance from the center. There is also a small area near the center of the OpenPIV single pass analysis where bias error hot spots are mostly absent. This suggests that the negative effect of streamline curvature on accuracy is compounded by higher particle displacements. It is unclear why the low-error (light blue) regions present in the PIVlab and DaVis analyses are somewhat off-center, but it could be due to a bias in the ability of the PIVlab and DaVis algorithms to detect certain directions of displacement better than others. For example, the low-error region for the DaVis analysis extends into the bottom left quadrant of the ROI. Since it is a clockwise flow, the direction of displacement is up and to the left in this quadrant. Perhaps the DaVis algorthm performs slightly better for upwards and to-the-left displacements. Likewise for the PIVlab algorithm, but for downwards and to-the-right displacements. A rigorous investigation into this matter to find the true cause of this peculiarity would necessitate a deep-dive into the code of PIVlab and DaVis and is out of the scope of the mI-PIV project.

3.9.3.3 Overall Comparison

Overall average magnitude of the bias error $|\vec{d_b}|_{ave}$ was found by finding the average of all $|\vec{d_b}|$ in the ROI as given in eq. (3.14), where N_{meas} is the number of displacement measurements in the ROI.

$$|\vec{d_b}|_{ave} = \frac{1}{N_{meas}} \sum_{i=1}^{N_{meas}} |\vec{d_b}|_i \tag{3.14}$$

These $|\vec{d_b}|_{ave}$ are shown for the Poiseuille flow for all programs in fig. 3.23 and for the pure rotation flow in fig. 3.24. Error bars represent one standard deviation from the mean. DaVis gives appreciably lower $|\vec{d_b}|_{ave}$ than any other program, which was expected given its advanced, professionally maintained algorithms. OpenPIV multipass gave much higher $|\vec{d_b}|_{ave}$ than any other, which again is thought to be caused by some unexpected error in the actual window shifting or some other anomalous error in the multipass validation scheme, since the single pass algorithm gave comparable results to the other programs. PIVlab outperformed the other two open-source programs for the Poiseuille flow but did worse

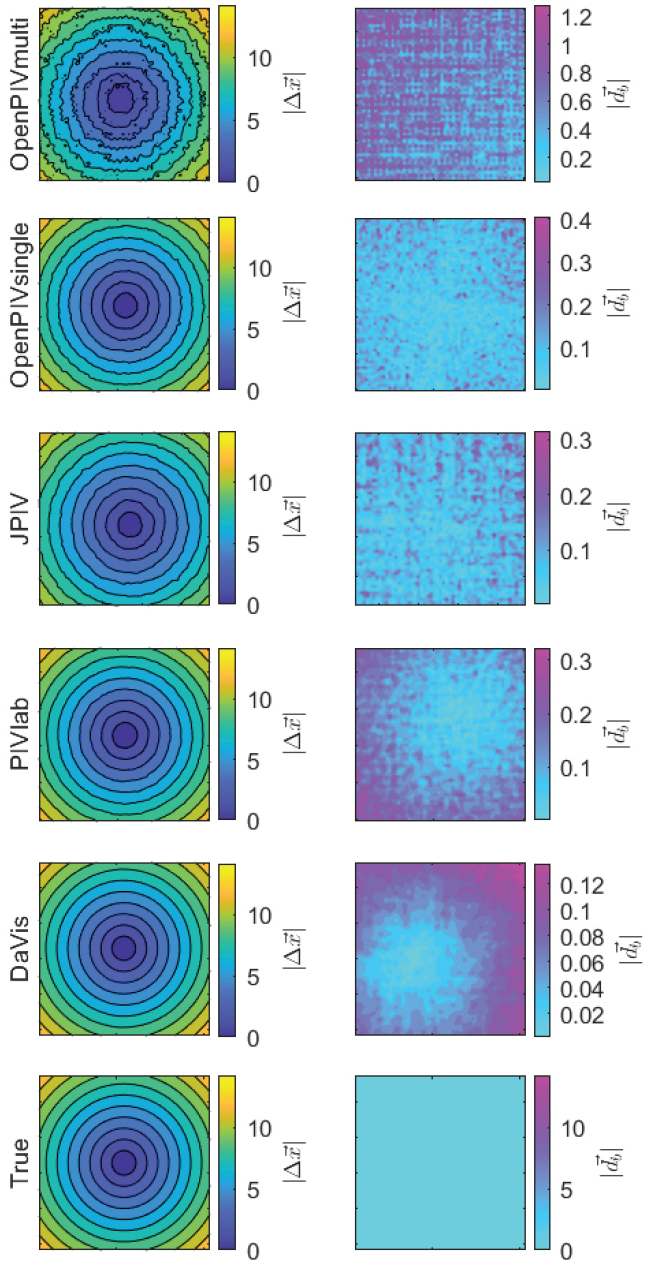

Fig. 3.24: OpenPIV, JPIV, PIVlab, and DaVis analyses of a synthetic pure rotational flow. True displacement data is shown in the bottom left figure. Absolute displacement for each analysis is shown in the left column and magnitude of the bias error $|\vec{d_b}|$, as given in eq. (3.12), is shown in the right column for each analysis.

than both for the pure rotation. JPIV had surprisingly good results, being only slightly worse than PIVlab for the Poiseuille flow but outperforming both OpenPIV and PIVlab for the pure rotational flow. However, despite these differences in performance, the open-source algorithms are very comparable in all practicality, especially in terms of the mI-PIV system. Since even best-case, the mI-PIV physical components themselves give bias errors on the order of 1 pixel (see fig. 3.9), the fraction-of-a-pixel differences in $|\vec{d_b}|_{ave}$ given by different algorithms will not have a considerable impact on the overall performance of the mI-PIV system.

A caveat for these synthetic image tests is that it is well-known that synthetic images generally do not accurately represent real PIV images. However, testing with synthetic images is a common method for obtaining baseline estimates for the capability of a given algorithm, and therefore it is considered an appropriate method here for approximate performance comparisons between different algorithms.

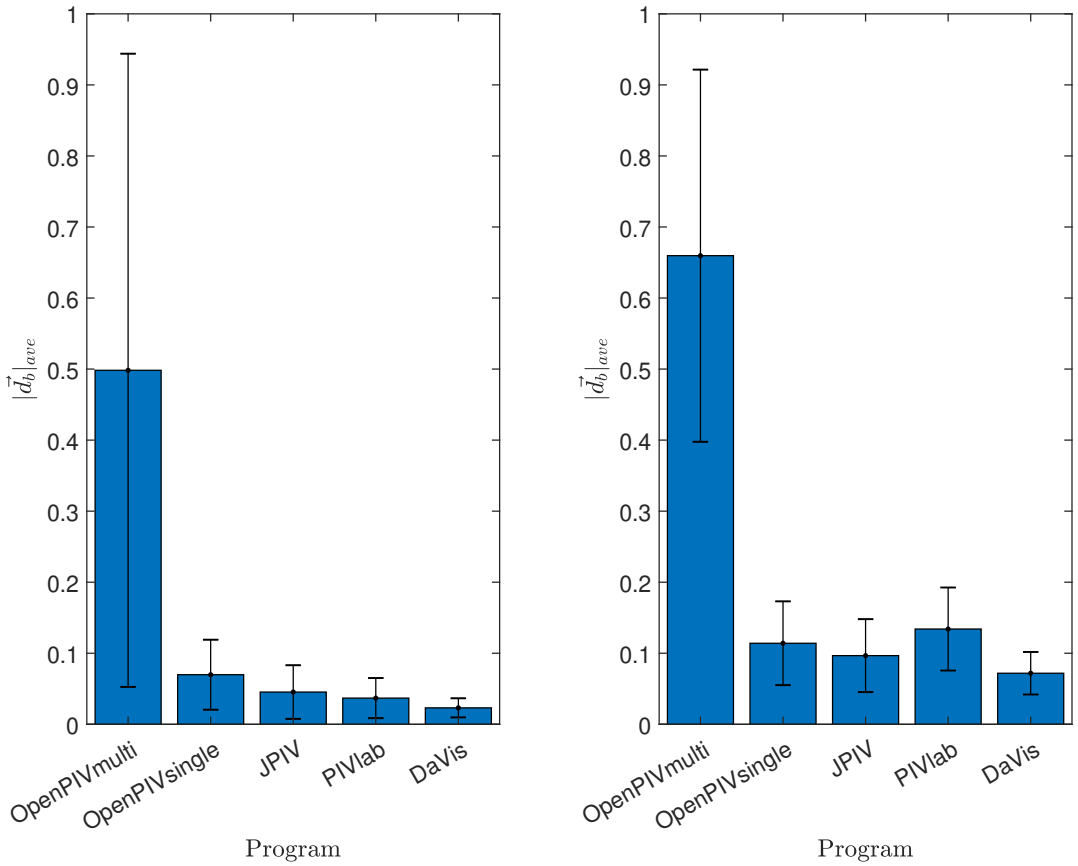

Fig. 3.25: $|\vec{d}_b|_{ave}$ of OpenPIV multipass, OpenPIV single pass, JPIV, PIVlab, and DaVis analyses on synthetic images of (a) a Poiseuille flow and (b) a pure rotational flow. Error bars are one standard deviation from the mean.

CHAPTER 4

Conclusion

The mI-PIV system, which relies on a mobile phone application for both image acquisition and PIV analysis, is a unique solution to expand the availability of PIV. It's design is described in Chapter 2. As part of the design-based research process, various PIV parameters relating to the mI-PIV system were benchmarked for accuracy and this benchmarking is described in Chapter 3. These parameters were: laser output power, average velocity of the flow, number of lasers used to produce the laser sheet, type of sheet optic lens, use of an LED pointer as the light source, and different open-source PIV algorithms – as shown in Table 3.1.

4.1 Benchmarking Conclusions

Laser output power was seen to have a relationship with overall average mean bias error resembling an exponential decay, and to have a similar but more pronounced relationship with overall average RMS error. Laser output powers of 5 mW and lower were seen to give unacceptable bias and RMS error for the mI-PIV system. For the mI-PIV system, bias error was seen to approach a minimum at laser output powers of about 10 mW, and RMS error was seen to approach a minimum at laser output powers of about 40 mW. The above findings may discourage other researchers from using laser powers under 5 mW in their PIV system designs, even if low laser output power is desired for their particular application. It may also serve as a guideline for other researchers in deciding what exact laser they prefer to use for their PIV system and were interested in lowering system cost, since higher-powered lasers tend to cost more. For example, a decision between lasers with output powers of 10 mW, 50 mW, or 100 mW may be made easier with the information contained in Section 3.4.3, since the trends are clear and could potentially even be forecasted to higher laser powers than those that were tested in this work. Of course, these findings are mainly

for PIV with use of a smartphone camera, and it is unknown how closely another image acquisition method would follow the trends found in this work.

Average flow velocity was shown to be positively correlated with error. This was expected due to higher in-plane gradients, particle streaking, greater in-plane motion of particles, and potentially greater out-of-plane motion of particles associated with higher flow velocities. It was found that the increase in error caused by higher flow velocities compounds with high error due to low laser powers to give especially high, unacceptable error for the mI-PIV system. These findings, described in detail in Section 3.5.3, may help guide the use of mobile phone cameras for other PIV setups, especially at low frame rates as were used in these experiments.

The use of the **double-laser device** is encouraged by the apparent threshold for minimum bias error at around 10 mW. The double-laser system is a design that combines two 5 mW (IIIa) lasers — which are considered safe enough to eliminate a need for safety eyewear [8, 11] — to produce a 10 mW laser sheet. This design was shown to effectively create a 10 mW laser sheet, giving bias and RMS errors similar to a single 10 mW laser. In principle, this multiple-laser system is not a new idea [23], but this work establishes the effectiveness of a double-laser setup for a low-power system to enhance accuracy considerably. The stir stick sheet **optic lens** was shown to perform equally to the Thorlabs optic lens, and this encourages the use of the very inexpensive stir stick as the mI-PIV optic lens and could serve to decrease cost for any low-laser-power, simplified PIV system. The **LED pointer** that was tested was not able to illuminate the particles in the flow sufficiently for detection by the mobile phone camera, and thus is not a suitable option for mI-PIV.

Although the different open-source **PIV programs** gave slightly different overall average bias errors, that difference was not enough to have an appreciable effect on the overall accuracy of the mI-PIV system. Also, these findings serve to show the similarity in performance of OpenPIV, JPIV, and PIVlab, at least when tested on synthetic images.

4.2 Future Work

There are many more parameters that can affect quality of PIV than were tested

in this study: Particle size, particle type, seeding density, thickness of the laser sheet, camera aperture, camera ISO, frame rate, interrogation area size, and different preprocessing techniques, to name a few. While it would be beneficial to study all these parameters, it is thought that the most important factors to study further are:

- The affect of the size of the ROI on mI-PIV accuracy. This study was only done on a 6-inch ROI. With increasing distance from the lens, a laser sheet weakens and thus particle illumination decreases. Thus, as ROI increases, the illumination from the laser sheet will not be able to illuminate the particles as well as with smaller ROIs. This affect may be an important factor to study in case it is desired to experiment using very large ROIs. Note: when adjusting the size of the ROI, it is imperative to ensure that particle size is large enough to appear larger than 2 pixels in diameter in the images. This is to avoid peak-locking and other ill effects caused by particles being too small [9, 10]. Of course, adjustments of ROI size also require adjustments in calibration.

- The affect of higher flow velocities (and thus $(d_{a,x})_{ave}$ for a fixed frame rate) on mI-PIV accuracy.

- The affect of adjusting frame rate on mI-PIV accuracy. Since the current mI-PIV application uses a mobile phone camera's automatic setting of 30 fps, these tests were run at 30 fps. Higher frame rates could potentially give better results for higher flow velocities by decreasing particle image displacement (when needed). However, as frame rate is adjusted on a mobile phone camera, less light is allowed into the sensor in each frame, resulting in particles that are less bright. This will likely cause PIV to give worse results than with lower frame rates, at least when illumination is kept very low, as is required for the mI-PIV system.

REFERENCES

[1] Z. J. Taylor, R. Gurka, G. A. Kopp, and A. Liberzon, "Long-duration time-resolved piv to study unsteady aerodynamics," *IEEE Transactions on Instrumentation and Measurement*, vol. 59, no. 12, pp. 3262–3269, Dec. 2010.

[2] W. Thielicke and E. J. Stamhuis, "PIVlab – towards user-friendly, affordable and accurate digital particle image velocimetry in MATLAB," *Journal of Open Research Software*, 2014.

[3] W. Thielicke, "The flapping flight of birds: Analysis and application," Ph.D. dissertation, University of Groningen, 2014.

[4] W. Thielicke and E. J. Stamhuis, "PIVlab - Time-Resolved Digital Particle Image Velocimetry Tool for MATLAB," Sep. 2019.

[5] P. Vennemann, "JPIV," 2020.

[6] C. Cierpka, R. Hain, and N. Buchmann, "Flow visualization by mobile phone cameras," *Experiments in Fluids*, vol. 57, no. 6, 2016.

[7] A. A. Aguirre-Pablo, M. K. Alarfaj, E. Q. Li, J. F. Hernández-Sánchez, and S. T. Thoroddsen, "Tomographic particle image velocimetry using smartphones and colored shadows," *Scientific Reports*, vol. 7, no. 1, p. 3714, Jun. 2017.

[8] *Electronic Code of Federeal Regulations*, Food and Drug Administration, Mar. 2020.

[9] R. Johnson, *Handbook of Fluid Dynamics*. CRC Press, 2016.

[10] M. Raffel, C. Willert, F. Scarano, C. Kähler, S. Wereley, and J. Kompenhans, *Particle Image Velocimetry: A Practical Guide*, ser. Experimental Fluid Mechanics. Springer International Publishing, 2018.

[11] *OSHA Technical Manual*, Occupational Safety and Health Administration, Jan. 1999.

[12] F. M. White, *Viscous fluid flow*, 3rd ed. McGraw Hill Higher Education, 2006.

[13] C. Kähler, T. Astarita, P. Vlachos, J. Sakakibara, R. Hain, S. Discetti, R. La Foy, and C. Cierpka, "Main results of the 4th international PIV challenge," *Experiments in Fluids*, vol. 57, no. 6, 2016.

[14] R. Adrian, "Twenty years of particle image velocimetry," *Experiments in Fluids*, vol. 39, no. 2, pp. 159–169, 2005.

[15] L. Adrian, R. Adrian, and J. Westerweel, *Particle Image Velocimetry*, ser. Cambridge Aerospace Series. Cambridge University Press, 2011.

[16] J. Westerweel, "Fundamentals of digital particle image velocimetry," *Measurement Science and Technology*, vol. 8, no. 12, pp. 1379–1392, 1997.

[17] D. Dabiri, "Cross-correlation digital particle image velocimetry – a review," 2007.

[18] A. Budd and J. Howison, "A low-cost PIV system for undergraduate fluids laboratories," vol. 2018-June, 2018.

[19] W.-Y. Chang, F. Lin, W.-F. Tsai, J.-S. Lai, C.-H. Loh, and S.-C. Kang, "Development of portable PIV devices," Jan. 2015, pp. 70–73.

[20] O. Chetelat, S. Y. Yoon, and K. C. Kim, "Design and construction of a miniature PIV (MPIV) system," *KSME International Journal*, vol. 15, no. 12, pp. 1775–1783, 2001.

[21] A. Goharzadeh, A. Molki, and M. Ohadi, "A proposed particle image velocimetry (PIV) system for instructional purposes in a modern mechanical engineering undergraduate laboratory program," *ASEE Annual Conference and Exposition, Conference Proceedings*, Jan. 2006.

[22] N. Jankovic, M. Barjaktarovic, M. Jankovic, and D. Cantrak, "First steps in new affordable PIV measurements," 2017.

[23] K. Knight and T. Uyeno, "A kinematic and kinetic analysis of a frog launching from water using digital particle image velocimetry," Ph.D. dissertation, Dec. 2014.

[24] B. Ring and E. Lemley, "Design and implementation of a low cost particle image velocimetry system for undergraduate research and education," 2014.

[25] W. G. Ryerson and K. Schwenk, "A simple, inexpensive system for digital particle image velocimetry (DPIV) in biomechanics," *Journal of Experimental Zoology Part A: Ecological Genetics and Physiology*, vol. 317 A, no. 2, pp. 127–140, 2012.

[26] S. Tingir, B. Cavlazoglu, O. Caliskan, O. Koklu, and S. Intepe-Tingir, "Effects of mobile devices on k–12 students' achievement: a meta-analysis," *Journal of Computer Assisted Learning*, vol. 33, no. 4, pp. 355–369, 2017.

[27] Interactive Flow Studies Corporation, "epiv^{TM} for interactive flow visualization & analysis in classroom or laboratory," Online, 2019, accessed March 17, 2020.

[28] M. Stanislas, K. Okamoto, and C. K. hler, "Main results of the First international PIV challenge," *Measurement Science and Technology*, vol. 14, no. 10, pp. R63–R89, Sep. 2003.

[29] M. Stanislas, K. Okamoto, C. J. Kähler, and J. Westerweel, "Main results of the second international PIV challenge," *Experiments in Fluids*, vol. 39, no. 2, pp. 170–191, Aug. 2005.

[30] M. Stanislas, K. Okamoto, C. J. Kähler, J. Westerweel, and F. Scarano, "Main results of the third international PIV challenge," *Experiments in Fluids*, vol. 45, no. 1, pp. 27–71, Jul. 2008.

[31] A. Minichiello, D. Armijo, S. A. Mukerjee, L. Caldwell, T. Truscott, V. Kulyukin, A. Bhouraskar, and J. Elliot, "Developing a mobile application-based particle image

velocimetry tool for enhanced teaching and learning in fluid mechanics: A design-based research approach," *Computer Applications in Engineering Education, Special Issue on Mobile Device Use and Social Media Role in Engineering Education*, 2020, under review.

[32] A. Minichiello, T. Truscott, and V. Kulyukin, "Mobile instructional particle image velocimetry (mi-PIV): Hands-onflow visualization and experimentation for improved student interest and technical capacity in navy-relevant engineering careers," 2018, volume I: Technical Proposal.

[33] F. Scarano and M. L. Riethmuller, "Iterative multigrid approach in PIV image processing with discrete window offset," *Experiments in Fluids*, vol. 26, no. 6, pp. 513–523, May 1999.

[34] J. Westerweel, D. Dabiri, and M. Gharib, "The effect of a discrete window offset on the accuracy of cross-correlation analysis of digital PIV recordings," *Experiments in Fluids*, vol. 23, no. 1, pp. 20–28, May 1997.

[35] F. Scarano, "Iterative image deformation methods in PIV," *Measurement Science and Technology*, vol. 13, no. 1, pp. R1–R19, Nov. 2001.

[36] S. Scharnowski, A. Sciacchitano, and C. Kähler, "A new look on the "valid detection probability" of PIV vectors," Jul. 2018.

[37] R. D. Keane and R. J. Adrian, "Optimization of particle image velocimeters: II. multiple pulsed systems," *Measurement Science and Technology*, vol. 2, no. 10, pp. 963–974, Oct. 1991.

[38] E. Rieschel and L. Brandt, "A study on the flow of viscous fluids in a square duct," 2016.

[39] B. R. Munson, D. F. Young, T. H. Okiishi, and W. W. Huebsch, *Fundamentals of Fluid Mechanics*. John Wiley and Sons, Inc., 2009.

[40] H. Huang, D. Dabiri, and M. Gharib, "On errors of digital particle image velocimetry," *Measurement Science and Technology*, vol. 8, no. 12, pp. 1427–1440, Dec. 1997.

[41] B. Wieneke, "PIV uncertainty quantification and beyond," Ph.D. dissertation, Delft University of Technology, 2017.

[42] A. Sciacchitano, "Uncertainty quantification in particle image velocimetry," *Measurement Science and Technology*, vol. 30, no. 092001, 2019.

[43] S. Scharnowski and C. J. Kähler, "On the loss-of-correlation due to PIV image noise," *Experiments in Fluids*, vol. 57, no. 7, p. 119, Jun. 2016.

[44] M. Kiss, "Factors defining the brightness of particle images in PIV-applications," Master's thesis, Czech Technical University in Prague, Faculty of Transportation Sciences, 2016.

[45] D. Sivas, A. Olcay, and H. Ahn, "Investigation of a corrugated channel flow with an open source PIV software," vol. 114, 2016.

[46] H. Nobach and E. Bodenschatz, "Limitations of accuracy in PIV due to individual variations of particle image intensities," *Experiments in Fluids*, vol. 47, no. 1, pp. 27–38, Jul. 2009.

[47] H. Nobach, "Influence of individual variations of particle image intensities on high-resolution PIV," *Experiments in Fluids*, vol. 50, no. 4, pp. 919–927, Apr. 2011.

[48] B. Ganapathisubramani and N. Clemens, "Effect of laser pulse duration on particle image velocimetry," *AIAA Journal*, vol. 44, no. 6, pp. 1368–1371, 2006.

[49] D. Bröder and M. Sommerfeld, "Planar shadow image velocimetry for the analysis of the hydrodynamics in bubbly flows," *Measurement Science and Technology*, vol. 18, no. 8, pp. 2513–2528, 2007.

[50] J. Estevadeordal and L. Goss, "An investigation of particle-shadow velocimetry (PSV) for transonic-flow applications," 2005.

[51] S. M. Hagsäter, C. H. Westergaard, H. Bruus, and J. P. Kutter, "Investigations on LED illumination for micro-piv including a novel front-lit configuration," *Experiments in Fluids*, vol. 44, no. 2, pp. 211–219, Feb. 2008.

[52] S. Nogueira, R. G. Sousa, A. M. F. R. Pinto, M. L. Riethmuller, and J. B. L. M. Campos, "Simultaneous PIV and pulsed shadow technique in slug flow: a solution ror optical problems," *Experiments in Fluids*, vol. 35, no. 6, pp. 598–609, Dec. 2003.

[53] O. Chételat and K. C. Kim, "Miniature particle image velocimetry system with LED in-line illumination," *Measurement Science and Technology*, vol. 13, no. 7, pp. 1006–1013, Jun. 2002.

[54] C. Dallas, M. Wu, V. Chou, A. Liberzon, and P. Sullivan, "Graphical processing unit-accelerated open-source particle image velocimetry software for high performance computing systems," *Journal of Fluids Engineering, Transactions of the ASME*, vol. 141, no. 11, 2019.

[55] J. M. Sherwood, J. Dusting, E. Kaliviotis, and S. Balabani, "The effect of red blood cell aggregation on velocity and cell-depleted layer characteristics of blood in a bifurcating microchannel," *Biomicrofluidics*, vol. 6, no. 2, p. 024119, 2012.

[56] W.-J. Kuo, Y.-S. Sie, and H.-S. Chuang, "Characterizations of kinetic power and propulsion of the nematode caenorhabditis elegans based on a micro-particle image velocimetry system," *Biomicrofluidics*, vol. 8, no. 2, p. 024116, 2014.

[57] P. K. Kundu and I. M. Cohen, "Chapter 9 - laminar flow," in *Fluid Mechanics (Second Edition)*, second edition ed., P. K. Kundu and I. M. Cohen, Eds. Boston: Academic Press, 2002, pp. 271 – 311.

APPENDICES

APPENDIX A

Flow Rate Limit Estimation for mI-PIV Experiments

Due to the slow frame rate of the mI-PIV camera (30 fps), the flow velocity of mI-PIV experiments is quite limited. Here, calculations are made that allow for simple estimation the highest possible flow velocity for mI-PIV to analyze based on the fixed frame rate of 30 fps, the size of the interrogation area used for PIV, the size of the desired ROI in real space, and the size of the desired ROI in pixels.

The maximum particle displacement (in pixels) that can be measured by an FFT correlation scheme is determined by the window size, or the interrogation region (IA) size (D_I) and the calibration C. Since an FFT correlation cannot measure displacements of more than 1/2 the window size, the maximum measurable pixel displacement is given by eq. (A.1). $D_{I,1}$ is the size of the first interrogation window, which, for multipass algorithms, is the only D_I that limits the pixel displacement [9].

$$(\Delta x)_{max} = \frac{D_{I,1}}{2} \tag{A.1}$$

From this displacement limit, an approximate velocity limit can be obtained if the real size of the ROI h_{real} [m] is known, as well as the image size H [pix] and the approximate fraction of the pixel size of the ROI h_{pix} divided by the size of the image H, which will be defined here as $\eta = \frac{h_{pix}}{H}$. An approximate calibration C_{approx} [m/s] can be obtained by eq. (A.2), and h_{pix} can be calculated by eq. (A.3).

$$C_{approx} = \frac{h_{real}}{h_{pix}} \tag{A.2}$$

$$h_{pix} = \eta H \tag{A.3}$$

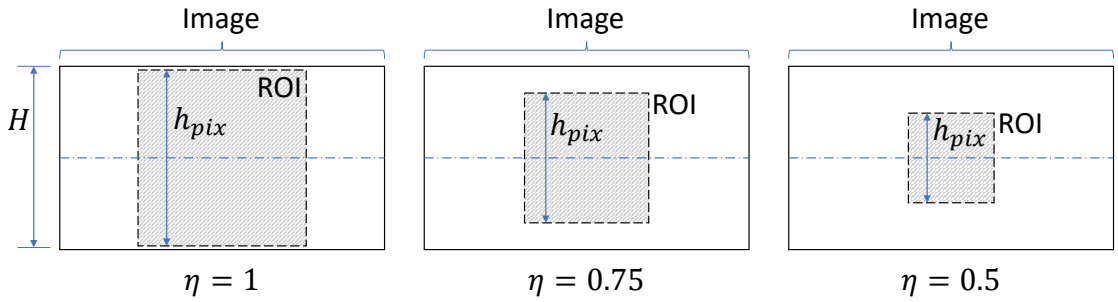

Fig. A.1: Diagram demonstrating an approximation of η by estimating the fraction of the pixel size h_{pix} of ROI divided by the size H of the image. The approximation of *eta* can then be used to find C_{approx}.

Note that the pixel size h_{pix} of the ROI does not have to be known to find C_{approx} if eq. (A.3) is used. This is useful, because while pixel size of the ROI may be difficult to obtain, image size h_{im} is always known for the camera and η can usually be estimated easily from visual inspection of an image of the ROI in question, as in fig. A.1. Also note that this C_{approx} is only for approximating maximum measurable flow velocity and should not be used as a final calibration for finding actual velocity data from PIV pixel displacement measurements.

Once C_{approx} has been calculated, it can be used to find maximum measurable velocity v_{max} using eq. (A.4)

$$v_{max} = (\Delta x)_{max} \times C_{approx} \times f \tag{A.4}$$

where f is frequency or frame rate [Hz]. Using these equations, the max velocities were plotted as a function of FOV size h_{real} for different IA sizes $D_{I,1}$ (given by the line colors and legend) and at different ROI pixel size to image size ratios, η, given by the different y-axes, in fig. A.2. The real ROI size h_{real} ranges from 0 to 0.5 [m], since this is the approximate range for most normal-sized PIV experiments that might be done in an undergraduate or high school setting. However, it may be noticed that all these relationships are linear and can be easily calculated for different values than have been plotted if need be.

A caveat of these maximum velocities v_{max} is that as FOV size in pixels h_{pix} decreases,

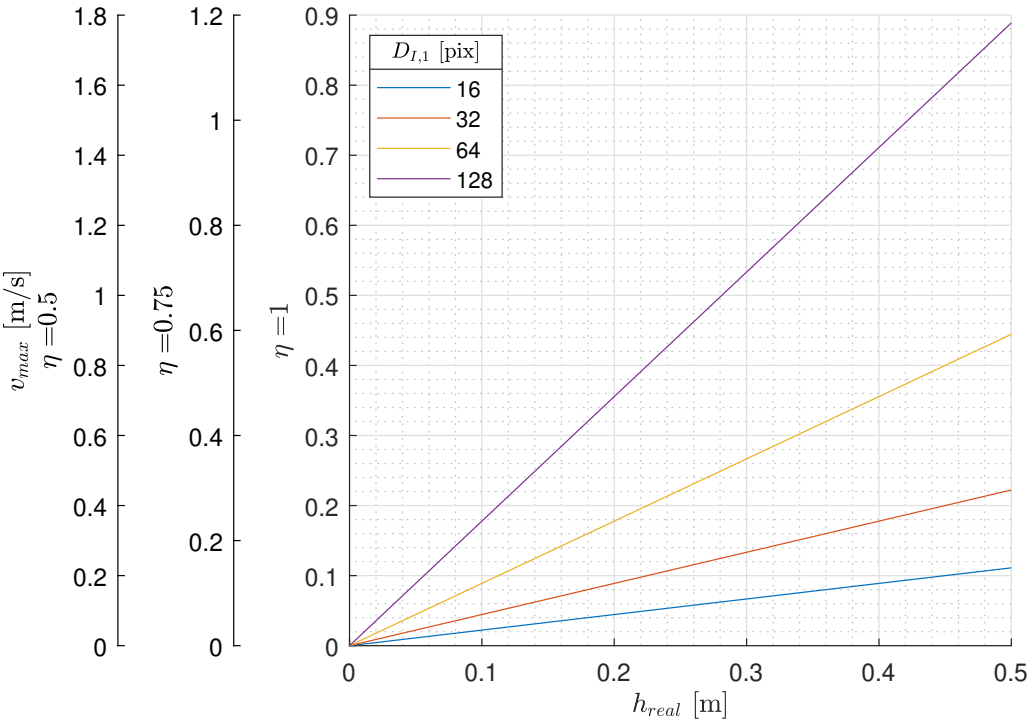

Fig. A.2: Plot for v_{max} as a function of real FOV size h_{real} (x-axis), IA_1 size $D_{I,1}$ (see legend), and η (different y-axes). This is based on a frame rate $f = 30$ [fps] and a camera with image size $H = 1080$ [pix].

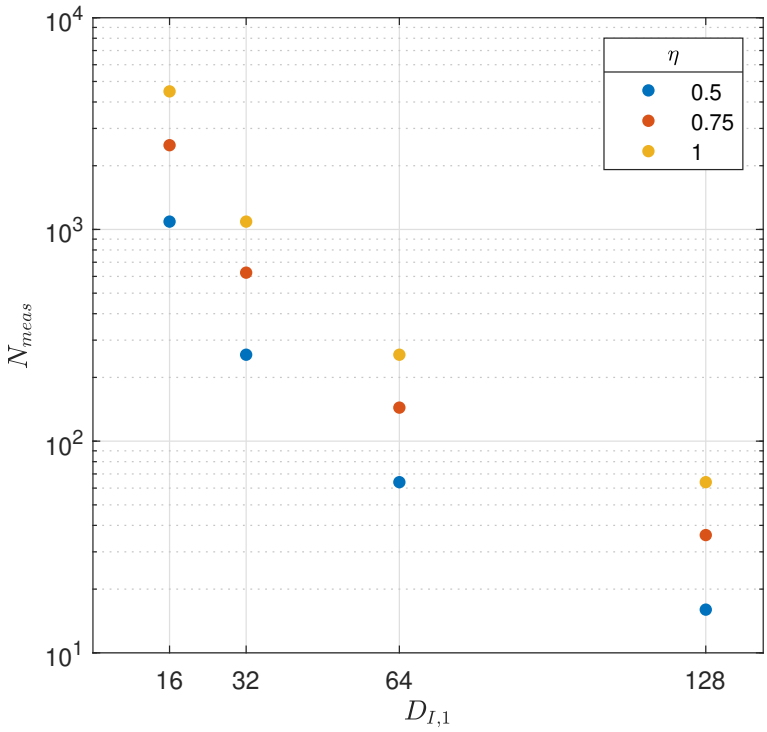

Fig. A.3: Plot for N_{meas} as a function of $D_{I,1}$ for different η. As $D_{I,1}$ increases, N_{meas} decreases rapidly, and as η decreases, N_{meas} also decreases rapidly. This is for an image size H of 1080 pixels.

the spatial resolution – or the amount of PIV measurements N_{meas}, equivalent to the amount of IA in the ROI – decreases rapidly. Also, as the window size $D_{I,1}$ increases, N_{meas} decreases. The number of PIV measurements in an ROI is easily calculated by eq. (A.5), where h_{pix} has already been calculated in eq. (A.3). N_{meas} was plotted as a function of $D_{I,1}$ for different η in fig. A.3.

$$N_{meas} = \left(\frac{h_{pix}}{D_{I,1}}\right)^2 \tag{A.5}$$

These maximum velocities are much higher than the velocities tested in Section 3.5.3. However, the first half of the trend in fig. 3.18, namely, the positive correlation of error and flow velocity, was indeed shown to be correct by experimentation by this work. Also, it is already a known fact that once the displacement Δx reaches 1/2 the size of the interrogation

window $D_I, 1$ of the first pass, there is a complete loss of correlation [9], so this does not need to be proven further.

APPENDIX B

Specifications of Equipment Used

The specifications for the equipment used in the "Laminar Entrance Length in a Square Pipe," "Downward Jet," and "Benchmarking" experiments described in Sections 2.4.1, 2.4.2 and 3.3 are given in Tables B.1 to B.3.

Table B.1: Equipment specifications for "Laminar Entrance Length in a Square Pipe" experiment (Section 2.4.1.)

Item	**Distributor**	**I.D. Type**	**I.D.**	**Description**
PIV Particles	Dantec Dynamics	S/N	9080A5011	"PSP, Polyamid Seeding Particles," 50 μm diameter
Square Pipe	ePlastics	Item	44229	"2-1/4-inch OD x 2-inch ID Clear Extruded Square Acrylic Tubing"
Pump	Superior Pump	Model	90040	"115 Volt [AC] portable transfer pump," 60 Hz, 2.3 Amps
Low-Q Flow Meter	King Instrument Company	P/N S/N	7510216A02 49690219008	Min. measurable flow rate: 0.2 GPM, Max. measurable flow rate: 2 GPM
High-Q Flow Meter	King Instrument Company	P/N S/N	7511212B04 83510119016	Min. measurable flow rate: 1 GPM, Max. measurable flow rate: 10 GPM
Laser Diode	NYBG	EAN UNSPSC Code	9366995768-044 39120000	532 nm, 1 mW (Note: measured at up to 60 mW output power), 5 VDC
Stir Stick	USU Chemistry Stores	Item	23499	Used for mI-PIV optic lens, diameter = 6 mm (1/4 inch). Must be solid, clear glass.
Mobile Phone	Google	Model	G013C	"Pixel 3 XL"

Table B.2: Equipment specifications for "Downward Jet" experiment (Section 2.4.2).

Item	**Distributor**	**I.D. Type**	**I.D.**	**Description**
PIV Particles	Dantec Dynamics	S/N	9080A5011	"PSP, Polyamid Seeding Particles," 50 μm ave. diameter
Pump	Top Fin	Model S/N	SP-1300 321809032-145	"Power Head SM 30," 120 VAC, 60 Hz, 7 W, Qmax: 119 GPH, Hmax: 2.43 ft
Laser Diode (mI-PIV)	NYBG	EAN UNSPSC Code	9366995768-044 39120000	532 nm, 1 mW (Note: measured at up to 60 mW output power), 5 VDC
Stir Stick (mI-PIV)	USU Chemistry Stores	Item	23499	Used for mI-PIV optic lens, diameter = 6 mm (1/4 inch). Must be solid, clear glass.
Mobile Phone (mI-PIV)	Google	Model	G013C	"Pixel 3 XL"
Camera (LG)	Photron	Model S/N	358527273 60K M1	"FASTCAM SA3"
Camera Lens (LG)	EX Sigma	# (Japanese)	11701278	"105 mm 1:2.8 DG Macro," aperture set to 2.8
PIV Laser (LG)	Amplitude	Model	100-M	Nd:YLF, 0.1-10 kHz, 527 nm. Distributor known in past as "Quantronix" and "Photonic Solutions"
Sheet Optic (LG)	LaVision	Article	1108405	"VZ-Beam steering, Sheet, divergent, 532r," f=-10

Table B.3: Equipment specifications for "Benchmarking" experiment (Section 3.3).

Item	**Distributor**	**I.D. Type**	**I.D.**	**Description**
PIV Particles	Dantec Dynamics	S/N	9080A5011	"PSP, Polyamid Seeding Particles," 50 μm ave. diameter
Water Tunnel	Engineering Laboratory Design Inc.	S/N	84515	"6" Flow Visualization Water Tunnel," 6-inch test section
Power Sensor	Thorlabs	Model S/N	S121C 12101913	"Photodiode Power Sensor," Si, 400-1100 nm, 500 mW
Power Meter	Thorlabs	Model	PM100USB	"Power and Energy Meter Interface," connects power sensor to laptop
Laser Diode (mI-PIV)	NYBG	EAN UNSPSC Code	9366995768-044 39120000	532 nm, 1 mW (Note: measured at up to 60 mW output power), 5 VDC
Stir Stick (mI-PIV)	USU Chemistry Stores	Item	23499	Used for mI-PIV optic lens, diameter = 6 mm (1/4 inch). Must be solid, clear glass.
Optic Lens (mI-PIV)	Thorlabs	Item	LK1087L2-A	"H=6.0 L=12.0 f=-6.4 N-BK7 A Coat Plano Concave Cyl Lens"
LED Pointer (mI-PIV)	CCEA Technical Lighting	Config. S/N	87.LN1.L3.V 14554	Green LED pointer with line diaphragm
LED Driver (mI-PIV)	CCEA Technical Lighting	Config. S/N	A11LED3W 13630	Used to power the LED pointer from wall outlet
Mobile Phone (mI-PIV)	Google	Model	G013C	"Pixel 3 XL"
Camera (LG)	Photron	Model S/N	358527273 60K M1	"FASTCAM SA3"
Camera Lens (LG)	EX Sigma	# (Japanese)	11701278	"105 mm 1:2.8 DG Macro," aperture set to 2.8
PIV Laser (LG)	Amplitude	Model	100-M	Nd:YLF, 0.1-10 kHz, 527 nm. Distributor known in past as "Quantronix" and "Photonic Solutions"
Sheet Optic (LG)	LaVision	Article	1108405	"VZ-Beam steering, Sheet, divergent, 532r," f=-10
90° Optic (LG)	LaVision	Article S/N	1108407 VZ10-0620	90°-angle laser mirror optic

APPENDIX C

Plots for Overall Average Total Bias and RMS Errors

Bias error in the x-direction $d_{b,x}$ and RMS error in the x-direction σ_x are more relevant to this study than the magnitude of the total bias error $|\vec{d_b}|$ and magnitude of the total RMS error $|\vec{\sigma}|$. However, for thoroughness, $|\vec{d_b}|$ is found by combining bias error in the x-direction $d_{b,x}$ with the bias error in the y-direction $d_{b,y}$ using eq. (C.1), and $|\vec{\sigma}|$ is found by combining RMS error in the x-direction σ_x^2 with the RMS error in the y-direction σ_y^2 using eq. (C.2)

$$|\vec{d_b}| = \sqrt{d_{b,x}^2 + d_{b,y}^2} \tag{C.1}$$

$$|\vec{\sigma}| = \sqrt{\sigma_x^2 + \sigma_y^2} \tag{C.2}$$

Overall average magnitude of the total mean bias error $|\vec{d_b}|_{ave}$ in the ROI was found using eq. (C.3), and overall average magnitude of the total RMS error $|\vec{\sigma}|_{ave}$ in the ROI was found using eq. (C.4), where N_{meas} is the number of PIV measurements in the ROI. Note that eq. (C.3) is a repeat of eq. (3.14).

$$|\vec{d_b}|_{ave} = \frac{1}{N_{meas}} \sum_{i=1}^{N_{meas}} |\vec{d_b}|_i \tag{C.3}$$

$$|\vec{\sigma}|_{ave} = \frac{1}{N_{meas}} \sum_{i=1}^{N_{meas}} |\vec{\sigma}|_i \tag{C.4}$$

These values were then plotted in fig. C.1(b) and fig. C.2(b). It can be seen in fig. C.1(b) that the bias error in the y-direction $|d_{b,y}|_{ave}$ (shown in fig. 3.16, and which is mostly random experimentation error) is combined with the bias error in the x-direction $|d_{b,x}|_{ave}$ (shown in fig. C.1(a)), which results in an overall upward shift in the bias error from fig. C.1(a) to

fig. C.1(b). Also, $(\sigma_x)_{ave}$ from fig. C.2(a) is combined with $(\sigma_y)_{ave}$ from fig. 3.17 to spread the upper range of the error from 15 to about 20 pixels in fig. C.2(b), compared to the $(\sigma_x)_{ave}$ and $(\sigma_y)_{ave}$ of about 15 pixels.

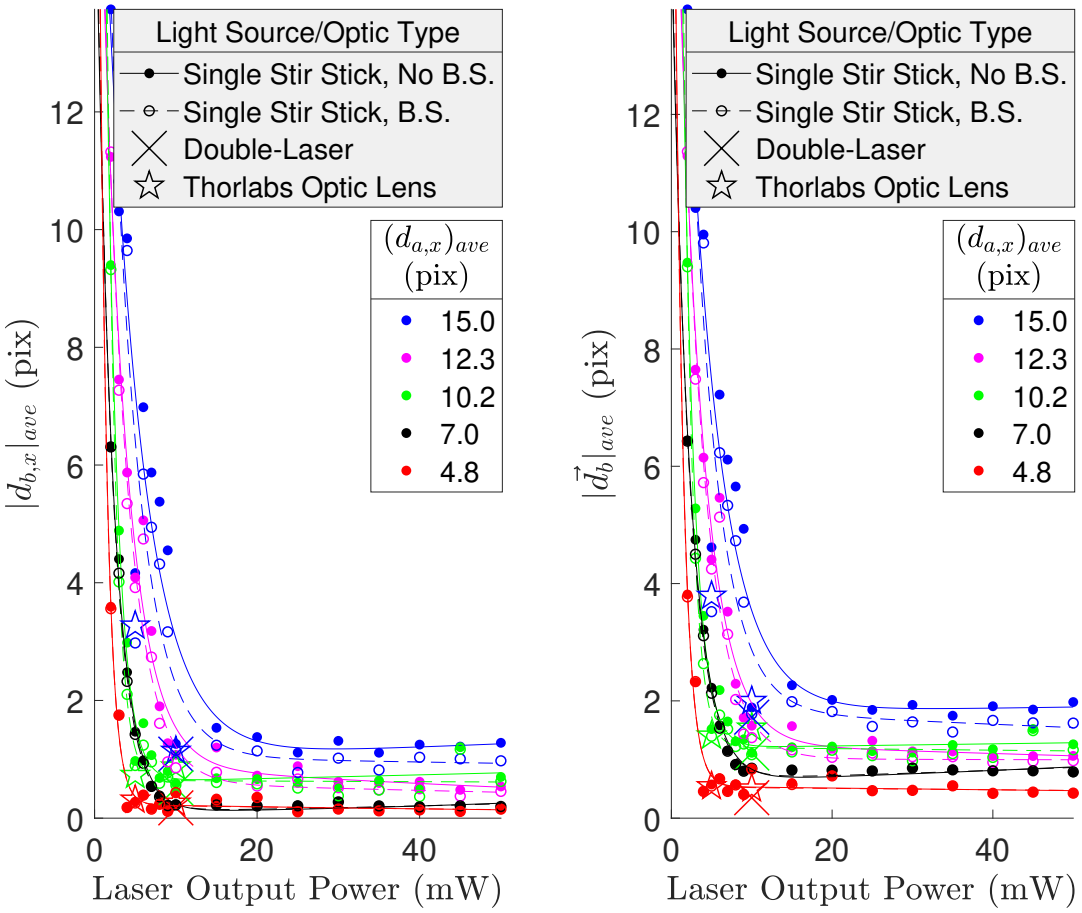

(a) (b)

Fig. C.1: (a) Overall average magnitude of mean bias error in the x-direction $|d_{b,x}|_{ave}$ as a function of laser output power for the mI-PIV system (same plot as in fig. 3.9). (b) Overall average of the magnitude of total mean bias error $|\vec{d}_b|_{ave}$ as a function of laser output power for the mI-PIV system. Colors represent overall average displacement $(d_{a,x})_{ave}$ in [pix]. Dots represent single stir stick analysis with no background subtraction applied to the mI-PIV images, and solid lines are two-term exponential fits of those data (for $(d_{a,x})_{ave}$ from top to bottom of legend, $R^2 = 0.93,\ 0.97,\ 0.99,\ 0.99,\ 0.94$). Circles represent single stir stick analysis with background subtraction applied to the mI-PIV images, and dashed lines are two-term exponential fits of those data (for $(d_{a,x})_{ave}$ from top to bottom of legend, $R^2 = 0.93,\ 0.97,\ 0.99,\ 0.99,\ 0.93$). Crosses at 10 mW represent error from the double-laser tests (no background subtraction for the mI-PIV images), and stars at 5 and 10 mW represent PIV error from the Thorlabs optic lens tests (no background subtraction for the mI-PIV images).

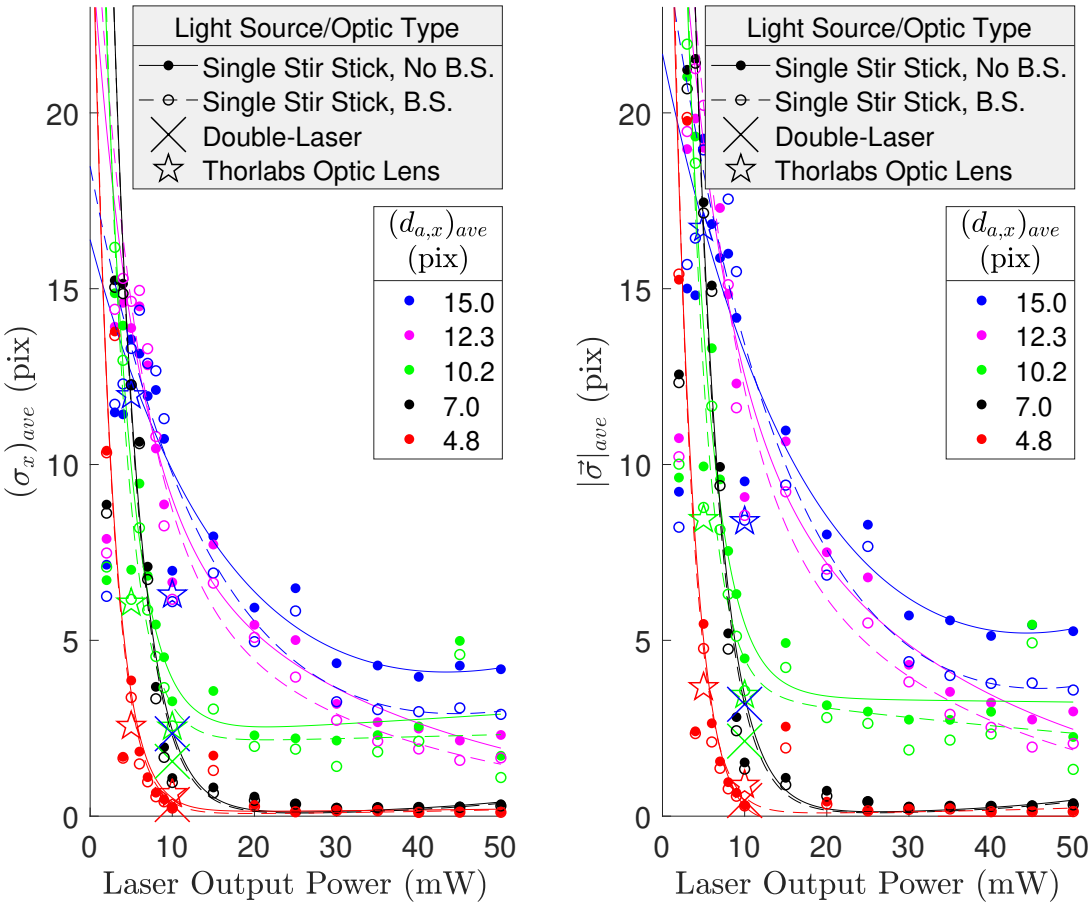

(a) (b)

Fig. C.2: (a) Overall average RMS error in the x-direction $(\sigma_x)_{ave}$ as a function of laser output power for the mI-PIV system (same as in fig. 3.10 but scaled to match scaling of fig. C.2(b)). (b) Overall average of the magnitude of total RMS error $|\vec{\sigma}|_{ave}$ as a function of laser output power for the mI-PIV system. Colors represent overall average displacement $(d_{a,x})_{ave}$ in [pix]. Dots represent single stir stick analysis with no background subtraction applied to the mI-PIV images, and solid lines are two-term exponential fits of those data (for $(d_{a,x})_{ave}$ from top to bottom of legend, $R^2 = 0.90,\ 0.95,\ 0.90,\ 0.97,\ 0.79$). Circles represent single stir stick analysis with background subtraction applied to the mI-PIV images, and dashed lines are two-term exponential fits of those data (for $(d_{a,x})_{ave}$ from top to bottom of legend, $R^2 = 0.90,\ 0.96,\ 0.89,\ 0.97,\ 0.80$). Crosses at 10 mW represent error from the double-laser tests (no background subtraction for the mI-PIV images), and stars at 5 and 10 mW represent PIV error from the Thorlabs optic lens tests (no background subtraction for the mI-PIV images).

APPENDIX D

Creation of Synthetic Images

D.1 Plane Poiseuille Flow

The images in Section 3.9.3.1 are modeled after a plane Poiseuille flow, which can be calculated from maximum Δx as shown in this section.

The flow profile for plane Poiseuille flow is given as eq. (D.1) in [57], where y is distance from the bottom wall of the channel, μ is dynamic viscosity, $\frac{dp}{dx}$ is the pressure gradient in the x-direction, and h is the height of the channel. This equation can be simplified to eq. (D.2) by defining α as in eq. (D.3).

$$u = -\frac{y}{\mu}\frac{dp}{dx}\left(\frac{h-y}{2}\right) \tag{D.1}$$

$$u = \alpha y\,(h-y) \tag{D.2}$$

$$\alpha = -\frac{dp}{dx}\frac{1}{2\mu} \tag{D.3}$$

Position y^* of maximum velocity u_{max} can then be calculated by setting the derivative of eq. (D.2), shown in eq. (D.4), to zero, as shown in eq. (D.5), then isolating y^*, as in eq. (D.6).

$$\frac{du}{dy} = \alpha\,(h-2y) \tag{D.4}$$

$$0 = \alpha\,(h-2y^*) \tag{D.5}$$

$$y^* = \frac{h}{2} \tag{D.6}$$

u_{max} can then be found by substituting y^* for y in eq. (D.2), resulting in eq. (D.7), and α can be put in terms of u_{max} by isolating α, obtaining eq. (D.8).

$$u_{max} = \frac{\alpha h^2}{4} \tag{D.7}$$

$$\alpha = \frac{4u_{max}}{h^2} \tag{D.8}$$

The flow profile of u can then be defined in terms of u_{max}, as in eq. (D.9). This u can be considered the same as Δx in pixels as long as u_{max} is defined as $(\Delta x)_{max}$ in pixels.

$$u = \frac{4y(u_{max})(h-y)}{h^2} \tag{D.9}$$

The code for generating the Poiseille flow images was based on the `<Accuracy.m>` file included with PIVlab, except that the very beginning of the code snippet titled `%% Generate random artificial particle images` is changed to the following code snippet (Appendix D.1.1):

D.1.1 Poiseuille Flow MATLAB Code Snippet

```
%% Generate random artificial particle images
Size=1080;
% size = 10;
partAm=120000;
Z=.333; %0.25 sheet thickness
dt=3; %particle diameter
ddt=1; %particle diameter variation
```

```
8  %disp(['Generating random artificial PIV images with ' num2str(
       partAm) ' particles...'])
9
10 [x,y]=meshgrid(1:1:Size);
11 v_const = 0;
12 v = ones(Size,Size) * v_const;
13
14 u_max = 10;
15 h = Size;
16 alpha = u_max * 4/h^2;
17 u = -alpha*y.*(y-h);
```

This code snippet was changed to define u according to a Poiseuille flow, using eq. (D.9) to define u. The u in this case is equivalent to Δx.

The images were made to distribute particles pseudo-randomly according to the prescribed $\Delta\vec{x}$, have zero out-of-plane motion, and have intensities of 255 at the particle locations, with particle size of about 3 pixels in diameter, with a variation of 1 pixel. Images were made to be 1080x1080 pixels and contained 120,000 particles. These same specifications also apply to the particle images with pure rotational flow.

D.2 Pure Rotational Flow

The equations used to set the rotational flow are eqs. (D.10) and (D.11), where Δx Δy are displacements in the x- and y-direction, $(\Delta x)_a$ and $(\Delta y)_a$ are displacements in the x- and y-direction at the vertical and horizontal edges of the image, x and y are x- and y-position, and a is the distance from the center of the image to the edge of the image, assuming a square image, as illustrated in fig. D.1, where orange arrows represent displacement vectors.

$$\Delta x = \left(\frac{y}{b}\right)(\Delta x)_a \tag{D.10}$$

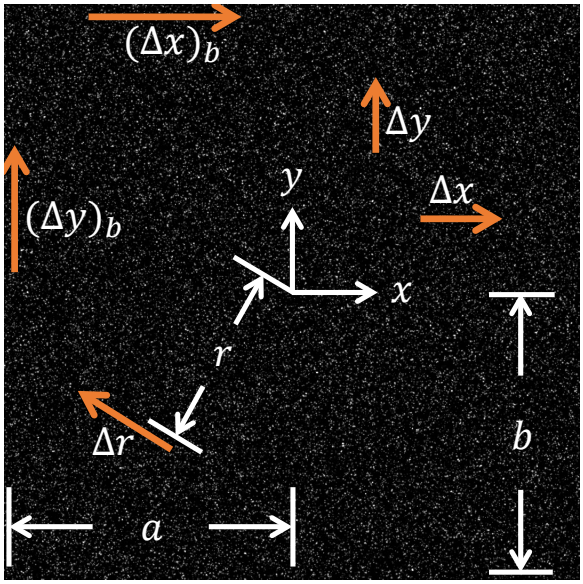

Fig. D.1: Diagram for describing terms of eqs. (D.10) to (D.12) for calculation of displacements for pure rotational flow in a particle image. The background image is one of the actual synthetic images used in this test.

$$\Delta y = -\left(\frac{x}{a}\right)(\Delta y)_b \tag{D.11}$$

If this is a square image, $a = b$. Assuming that $(\Delta x)_b = (\Delta y)_a$, eqs. (D.10) and (D.11) can be equated to eq. (D.12), where $|\Delta\vec{r}|$ is the magnitude of tangential displacement around the center of the image and r is the radial distance from the center of the image, by equating

$$\begin{aligned}
|\Delta\vec{r}| &= \sqrt{(\Delta x)^2 + (\Delta y)^2} \\
&= \sqrt{\left(\left(\tfrac{y}{a}\right)(\Delta x)_b\right)^2 + \left(-\left(\tfrac{x}{b}\right)(\Delta y)_a\right)^2} \\
&= \sqrt{\left(\tfrac{y^2}{a^2}\right)(\Delta x)_b^2 + \left(\tfrac{x^2}{b^2}\right)(\Delta y)_a^2} \\
&= \sqrt{\tfrac{2(x^2+y^2)(\Delta x)_b^2}{2b^2}} \\
&= \tfrac{\sqrt{x^2+y^2}}{b}(\Delta x)_b \\
&= \left(\tfrac{r}{b}\right)(\Delta x)_b
\end{aligned}$$

$$|\Delta\vec{r}| = \left(\frac{r}{b}\right)(\Delta x)_b \tag{D.12}$$

Equation (D.12) is more intuitive when thinking of a rotational flow, since in such a flow the tangential velocity magnitude $|\Delta\vec{r}|$ is a function of radius r. However, as has been shown, eqs. (D.10) and (D.11) is equivalent to eq. (D.12), and therefore they were used to produce the rotational flow for the synthetic images.

The code in `<Accuracy.m>` originally creates a pure rotational flow with $(\Delta x)_a = 5$ [pix]. For the images used in this study, the code was changed slightly so that $(\Delta x)_a = 10$ [pix], as in the following code snippet (Appendix D.2.1):

D.2.1 Pure Rotation Flow MATLAB Code Snippet

```
%% Generate random artificial particle images
Size=1080;
partAm=120000;
Z=.333; %0.25 sheet thickness
dt=3; %particle diameter
ddt=1; %particle diameter variation
%disp(['Generating random artificial PIV images with ' num2str(
    partAm) ' particles...'])
[v,u] = meshgrid(-Size/2:1:Size/2-1,-Size/2:1:Size/2-1);
u=u/max(max(u));
v=-v/max(max(v));
u_max = 10;
v_max = 10;

u=u*u_max;
v=v*v_max;
```

In this code snippet, u is again equivalent to Δx, and also, u_{max} is equivalent to $(\Delta x)_a$.